Ph.D. thesis
Péter FIALA

Development of a numerical model for the prediction of ground-borne noise and vibration in buildings

Ph.D. dissertation

Péter FIALA
M.Sc.E.E

Supervisor:
Dr. János GRANÁT
Department of Telecommunications

2008

Contents

List of Figures

List of Tables

Preface and Declaration

The work described in this dissertation was carried out at the Budapest University of Technology and Economics between September 2002 and September 2007, under the guidance of Dr. János Granát and Dr. Fülöp Augusztinovicz.

I would like to thank Dr. János Granát for his assistance, especially during my last graduate years, when he introduced the field of numerical acoustics to me. I am grateful to Dr. Fülöp Augusztinovicz for proposing the topic of dynamic soil-structure interaction as my PhD research field and for his guidance during my PhD research years. I am grateful to the staff of the Laboratory of Acoustics for their technical expertise and advice. Attila, Krisztián, Tamás, Feri, Csaba és Tibi, you provide a healthy atmosphere for work.

Part of the research was carried out at the Catholic University of Leuven, under the guidance of Prof. Geert Degrande. I would like to express my gratitude to him for teaching me and helping a lot with my publications. Dear BWM guys, I am proud to have been a member of your research group for one year, *Ik ben U eeuwig dankbaar, weet U wat, drink iets voor mij* [vhG01]. My research in Leuven was funded by the Hungarian Scholarship Board and the Flemish Community. Their financial support is gratefully acknowledged.

I declare that this dissertation is the result of my own work, except where specific reference has been made to the work others. The work, or any part of it, has not previously been submitted for any degree, diploma or other qualification.

Chapter 1

Introduction

1.1 Ground-borne noise and vibration in buildings

Significant vibration in buildings near surface or underground railway tracks or roads is attributed to moving vehicles. Traffic induced vibrations in dense urban environments can cause structural damage in buildings and annoyance to the inhabitants of surrounding buildings in the form of vibrations or re-radiated noise.

The vibrations within a building have several effect on the building's structure. The vibrations can vary in a large range from imperceptible to levels causing structural damage. The limit above which the vibrations damage the structure is not clear. Some authors claim that traffic induced ground-borne vibrations can not damage the structures and at worst disturb the occupants. Others [Cro65], however, state that the damaging effect of low frequency vibrations is cumulative and causes the uneven soil settlement under buildings over a long time period.

This thesis does not concern the effect of vibrations on the structural stability of buildings.

The occupants inside the building can percept the vibrations directly in the form of structural motion or indirectly, in the form of noise. Considering the vibration perception limits, the standards divide the frequency range into low and high frequencies. The low frequency range is below 8 Hz. In this frequency range, a vibration acceleration amplitude greater than 5 mm/s^2 is observable. In the higher frequency range, the standards define a velocity amplitude of $1 \cdot 10^{-2}$ mm/s as observable vibration level.

The most important disturbance factor on the inhabitants is the re-radiated noise. This noise is radiated indirectly by the vibrating walls and floors of the structure. The sensitivity of the human ear varies over a large scale with frequency. The smallest observable sound pressure amplitude is about 20 μPa. This is the perception threshold at 1 kHz that is much higher than frequencies caused by traffic induced vibrations. In the low frequency range, below 200 Hz, the human ear can percept the sound pressure amplitudes above 70 μPa, and below 70 Hz, only sound pressure amplitudes above 0.5 mPa are observable. It is important to mention that directly imperceptible vibration levels can radiate perceptible noise inside the building's rooms.

This thesis concerns the effect of low magnitude structural vibration and re-radiated noise on the building's occupants.

Regarding the sources of vibration in building, traffic induced ground vibrations are

tackled in the present thesis. Traffic excitation sources can basically be divided into two groups: road and railway traffic excitations.

For the case of road traffic excitation, the main vibration source mechanisms are the rolling of uneven wheels on an uneven road and the rolling of wheels over road-discontinuities as road joints, smaller grooves or traffic plateaus [Lom01]. For the case of the typical vehicle speed and the typical dimensions of road discontinuities, the road traffic induced vibrations are in the frequency range below 80 Hz.

Considering the surface or underground railway traffic induced vibrations, the main vibration generation mechanisms are the rail and wheel unevenness and the quasi-static excitation [Hun07]. The first excitation is due to the rolling of uneven wheels on rough rails, and is more important for the case of low train speeds below 150 km/h. The latter excitation mechanism is the force applied to the rail as a static force passes over the sleepers of the track. This excitation type is more important in the domain of higher train speeds [MK83]. Train traffic induced vibrations are usually within the frequency range below 200 Hz.

Considering the low-pass filtering effect of the soil on the vibration propagation in the ground, the traffic induced vibrations are dominant in the frequency range below 80 Hz. If the re-radiated noise is also investigated, then the frequency range up to 150-200 Hz is important.

In the present thesis, traffic induced ground-borne vibrations in the frequency range between 0 Hz and 200 Hz are investigated.

Considering the vibration propagation in the soil and in the building, it is important to mention that both media are strongly inhomogeneous, and there is a large variability in their structure. The dynamic properties of the soil vary strongly with depth and along the horizontal coordinates too. The material characteristics of the structural elements are generally also inhomogeneous, and there is always a large uncertainty in the dynamic properties of structural joints. In most of the practical cases it is impossible to have an exact knowledge about all the parameters that affect the vibration propagation in the soil and in the structure. It is common that only parameter ranges are known, and it is assumed that the parameters vary within these ranges with known or unknown distribution. Therefore, from the practical point of view, deterministic methods are not sufficient to describe the vibration propagation, stochastic approaches [Sch07] and uncertainty models [MV05] give a better understanding of ground-borne vibration phenomena. However, as all the stochastic approaches are based on reliable, complex deterministic models where the influence of a wide range of input variables on the response can be investigated, deterministic approaches remain an important issue in the topic of ground-borne noise and vibrations.

In the present thesis, a deterministic model of ground-borne vibrations in buildings will be considered.

1.2 Research background and objectives

In order to be able to handle to problem of traffic induced vibration and noise in dense urban areas, the clear understanding of the vibration generation mechanisms and the phenomena related to vibration propagation in the soil, structures and in the air is essential.

The main objective of the research described in the present thesis is to present a complex numerical model of the whole vibration-chain. The complex model should account for the vibration generation by moving vehicles, vibration propagation in the soil, dynamic soil-

structure interaction, vibration propagation in the building and sound radiation into closed rooms.

A reliable model that can take all these effects into account, can be a valuable tool in the hand of the engineer when the vibration isolation of structures settled near railway lines or roads is planned. The model can be used to predict the in-door noise and vibrations before the construction is started, the model can help to define the required amount of vibration or noise isolation, and the model can be used to predict the effect of different noise and vibration isolation techniques, and to optimize the construction costs.

Significant part of the research has been carried out within the framework of the European project CONVURT between 2003 and 2006. The acronym is for COntrol of Noise and Vibration due to Underground Railway Traffic. The objective of the project was to create validated innovative and quantitative modeling tools to enable prediction of locations where ground-borne vibration transmission and thereby noise will occur in metropolitan railway networks. The project aimed to develop and evaluate innovative and cost effective track and tunnel equipment to reduce ground-borne vibration capable of being retrofitted and exported worldwide, and to prepare Good Practice Guides for underground railway operation in order to maintain minimum vibrations for the lifetime of operation.

The project CONVURT succeeded in the development of separate models for the investigation of subproblems of the total vibration chain. After the project CONVURT finished, the work on the model integration has started. One of the most important results of the present work is that the total coupled numerical model has been integrated and a practical application is also presented.

1.3 Organisation of the text

The structure of the foregoing parts of the thesis is as follows:

Chapter 2 introduces the soil model used in the thesis. This soil model is a linear, isotropic, horizontally layered one-phase half space. The chapter introduces the solution of the Navier-Cauchy equations in the wavenumber-frequency domain and discusses the dynamic stiffness matrix method. Using a simple numerical example, the usage of the method is presented finally.

Chapter 3 deals with the dynamic interaction between the ground vibrations and the vibrations of a structure embedded into the soil. A substructuring-subdomain formalism is introduced, which computes the structural vibrations by means of a coupled finite element-boundary element method.

Chapter 4 considers the boundary element method used in elastodynamics in details. The problem of fictitious eigenfrequencies is discussed which occurs when the impedance of foundations embedded into the soil is computed. The chapter introduces the usage of the CHIEF method and compares this method with the modified Burton and Miller algorithm. The two methods are compared in a numerical example, where the dynamic impedance of cavities embedded in a homogeneous full space is computed.

Chapter 5 deals with the problem of sound radiation into the closed rooms of the building. A spectral finite element formulation is introduced that can be used to compute the re-radiated noise in the rooms in the frequency range between 0 Hz and 200 Hz. A numerical example illustrates the method.

In Chapter 6 a complex numerical example is introduced. The vibration and re-radiated

noise in a three-story portal frame office building due to the passage of a Thalys high speed train is computed. The effect of dynamic soil-structure interaction on the vibration and noise levels in the building is considered. Finally, the effectivity of several noise and vibration reduction techniques (base isolation, floating floors and box-within box arrangements) is demonstrated.

Chapter 7 presents the practical application of the developed numerical model. The practical application consists of the specification of the vibration isolation requirements for the new Budapest underground line m4. The methodology described in section 2 has been used to measure the soil properties along the new underground line, and the total numerical model has been applied for the modeling of vibration propagation from the metro tunnel to nearby buildings.

Chapters 2-3 are based on material available in literature, and these parts do not contain new developments. However, as the methods described here form the basis of the total numerical model, their discussion is necessary in order to present the following parts of the thesis in an easy-to-understand form. The Chapters 4-5 present own research developments. Due to our knowledge, the numerical example presented in Chapter 6 is the first application available in literature, where a coupled numerical model is used to describe the total vibration path starting from vibration generation by a moving vehicle and ending with the re-radiated noise in a building's room. Chapter 7 demonstrates the practical use of the model.

Chapter 2

Vibration propagation in the soil

2.1 Introduction and literature survey

Soil is a complex medium. It is built up of a mixture of solid material, fluid and gas particles, distributed inhomogeneously in space. Due to this structural complexity and inhomogeneity, the soil's behavior under dynamic loads is generally non-linear and anisotropic. Moreover, as the dimension of the ground is practically infinite, the modeling of vibration propagation in the soil has been a challenging issue in computational engineering.

The simplest soil model is the linear isotropic homogeneous half space described as a continuous elastic solid medium. Due to the assumption of linear behavior, this model can only be used with restrictions, where small magnitude of soil displacements and stresses is assumed. In most of the practical cases related to traffic induced ground vibrations, these assumptions are fulfilled. The governing partial differential equations of this ground model has been laid down in the beginning of the 19-th century. Some specific effects of wave propagation in the homogeneous half space has been discovered by Rayleigh [Ray87], Lamb [Lam04] and Love [Lov44].

As computers have been used in scientific and technical computations, the role of numerical techniques has become more important. Since the second half of the 20-th century, approximate solutions of the governing partial differential equations are searched for, basically by means of finite element (FE) or boundary element (BE) methods.

The advantage of the application of the finite element method (FEM) for the analysis of vibration propagation in the soil is that the inhomogeneous material characteristics can be fully taken into account. Lysmer [Lys70] applied the FEM to analyze the behavior of Rayleigh and Love waves in layered one-phase soil models. Here, one-phase means that the presence of the gas and fluid phases is neglected, and only a continuous solid phase is taken into account. Cramer [CW90] developed a finite element method for three-phase soil models and applied it successfully for the computation of impedance stiffness functions. Houdéec [HM90] and Chouw [CLS90] applied a FEM for determining the effectiveness of trenches as a ground vibration countermeasure.

A common drawback of the application of the FEM for the analysis of ground vibrations is that only a finite section of the infinite soil can be discretized. This leads to large FE meshes and undesired reflection of waves from the mesh boundary. The reflection effect can be reduced only by introducing absorption boundary conditions or infinite elements at the mesh boundary, as performed by Lysmer [LW72].

The mentioned drawbacks can be avoided by applying the Boundary element method (BEM) for the computation of vibration propagation in the soil. With the BEM, only the boundary of the investigated domain has to be meshed, so the dimensionality of the problem is reduced by one. On the other hand, the complexity of the soil structure handled with the BEM is limited, as it is is determined by the Green's function used in the BE formalism. Using a BEM with the simplest Green's function of a homogeneous full space, the whole (infinite) soil surface and the interfaces between adjacent soil layers have to be meshed. This restricts the computations practically to simple 2D cases [RFBA04].

The size of the BEM mesh can be reduced significantly if the Green's function matches the problem geometry. Therefore, the Green's functions of the linear elastic half space and the layered half space are of large importance. These Green's functions express the displacements and stresses in a half space consisting of homogeneous horizontal layers due to a unit point load in the soil.

Thomson introduced a matrix formalism [Tho50] to compute the phase velocity of surface waves in multilayered soils. This method has been further developed by Haskell and Kausel [Has53] [KR81] [KP82] to the Dynamic Stiffness Matrix method that computes the Green's functions of the layered half space analytically in the wavenumber-frequency domain. In the Dynamic Stiffness Matrix method the soil is discretized into homogeneous horizontal layers, and the displacements between the layer boundaries are expressed by using the analytical solution of the wave equation in the layers as shape function [Mül90]. The numerical aspects of the integral transforms between the wavenumber and space domains have been considered in details by Apsel and Luco [LA83] [AL83]. The Dynamic Stiffness Matrix method has been further developed by Kausel [Kau86] for anisotropic media, and later by Degrande [DDRVdBS98] [Deg02] for three-phase soil models. The Direct Stiffness Matrix method, combined with the BEM has gained large interest in the recent years. It has been successfully applied to 2D [JP91] [JP92] and 3D problems [WP90] [Aue94] [JP93] [JP97], with standing and moving sources [JLHPP98][LMPLH02] as well.

An alternative method for the computation of the Green's functions of a layered half space is the so called Thin Layer Method [Kau94]. Using this method, the soil's displacements are computed in the frequency-wavenumber domain by discretizing the soil profile to thin soil layers and approximating the displacements between the boundaries by means of polynomial shape functions. This method has been recently further developed by Schevenels [Sch07].

In the scope of this thesis, the Dynamic Stiffness Matrix method combined with a Boundary Element Method is used to compute vibration propagation in the soil. The following parts of this chapter introduce the concepts of the Dynamic Stiffness Matrix method [Wol85]. The governing equations of vibration propagation in linear elastic media are presented, followed by the description of the concept of modeling in the frequency-wavenumber domain. A simple numerical example introduces the usage of the Dynamic Stiffness Matrix method for modeling surface wave propagation.

2.2 The governing equations

The displacement vector in the soil at the coordinate $\mathbf{x}$ and time t is denoted by $\mathbf{u}(\mathbf{x}, t)$, where in a Cartesian coordinate system,

$$\mathbf{u}(\mathbf{x}, t) = \begin{Bmatrix} u_x(x, y, z, t) & u_y(x, y, z, t) & u_z(x, y, z, t) \end{Bmatrix}^{\mathrm{T}} \tag{2.1}$$

The relationship between the strain tensor $\boldsymbol{\epsilon}$ and the displacements is given by

$$\boldsymbol{\epsilon} = \frac{1}{2}\left(\nabla\mathbf{u} + (\nabla\mathbf{u})^{\mathrm{T}}\right) \tag{2.2}$$

where $\nabla\mathbf{u}$ denotes the displacement's derivative tensor.

The equilibrium equations (Newton's second law) can be written in the form:

$$\nabla \cdot \boldsymbol{\sigma} + \rho\mathbf{b} = \rho\ddot{\mathbf{u}} \tag{2.3}$$

where $\boldsymbol{\sigma}$ stands for the stress tensor, ρ denotes the mass density and $\mathbf{b}$ stands for the body forces (gravity or magnetic forces). A dot on a variable denotes derivation with respect to time.

The strain and stress tensors are related to each other by Hooke's law:

$$\boldsymbol{\sigma} = \lambda\bar{\epsilon}\mathbf{I} + 2\mu\boldsymbol{\epsilon} \tag{2.4}$$

where $\bar{\epsilon}$ denotes the trace of the stress tensor (the cubic dilatation) and $\mathbf{I}$ stands for the identity matrix. The material properties λ and μ are the Lamé constants which can be expressed as a function of the Young's modulus E and the Poisson's ratio ν as:

$$\lambda = \frac{\nu E}{(1+\nu)(1-2\nu)} \tag{2.5a}$$

$$\mu = \frac{E}{2(1+\nu)} \tag{2.5b}$$

At a boundary with an external unit normal vector $\mathbf{n}$, the surface traction vector $\mathbf{t}$ is given by:

$$\mathbf{t} = \boldsymbol{\sigma}\mathbf{n} \tag{2.6}$$

Substituting Equations (2.2) and (2.4) into Equation (2.3), the Navier's equations are obtained:

$$(\lambda+\mu)\nabla\nabla\cdot\mathbf{u} + \mu\nabla^2\mathbf{u} + \rho\mathbf{b} = \rho\ddot{\mathbf{u}} \tag{2.7}$$

2.3 P and S waves

In an infinite homogeneous elastic half space with zero body forces ($\boldsymbol{b} = \mathbf{0}$), the Navier's equations have two basic solutions. The first solution corresponds to a non-rotational displacement field, the second corresponds to a non-divergent displacement field.

According to the well-known theorem of vector algebra, every displacement field can be decomposed into the sum of a non-rotational and a non-divergent vector field.

$$\mathbf{u} = \mathbf{u}_{\mathrm{P}} + \mathbf{u}_{\mathrm{S}} \tag{2.8}$$

where $\mathbf{u}_{\mathrm{P}}$ is non-rotational

$$\nabla \times \mathbf{u}_{\mathrm{P}} = \mathbf{0} \tag{2.9}$$

and $\mathbf{u}_{\mathrm{S}}$ is non-divergent

$$\nabla \cdot \mathbf{u}_{\mathrm{S}} = 0 \tag{2.10}$$

writing equation (2.7) on the displacement field $\mathbf{u}_\mathrm{P}$ and making use of the identity

$$\nabla\nabla\cdot\mathbf{u} = \nabla\times(\nabla\times\mathbf{u}) + \nabla^2\mathbf{u} \tag{2.11}$$

we get the following wave equation:

$$\nabla^2\mathbf{u}_\mathrm{P} = \frac{1}{C_\mathrm{P}^2}\ddot{\mathbf{u}}_\mathrm{P} \tag{2.12}$$

where

$$C_\mathrm{P} = \sqrt{\frac{\lambda+2\mu}{\rho}} \tag{2.13}$$

is the velocity of the primary (pressure) P-wave.

Writing equation (2.7) on the displacement field $\mathbf{u}_\mathrm{S}$, the first term of the left hand side cancels ad we obtain

$$\nabla^2\mathbf{u}_\mathrm{S} = \frac{1}{C_\mathrm{S}^2}\ddot{\mathbf{u}}_\mathrm{S} \tag{2.14}$$

where

$$C_\mathrm{S} = \sqrt{\frac{\mu}{\rho}} \tag{2.15}$$

is the velocity of the secondary (shear) S-wave.

2.4 The dynamic stiffness matrix of the layered half-space in two-dimensions

In the following, it will be assumed that all the variables are constant in the y direction, so all the derivatives with respect to the y space coordinate are equal to zero. Further, it will be assumed that no body forces are acting in the soil: $\mathbf{b} = \mathbf{0}$.

Transforming the time t to the frequency ω in Equation (2.12) by means of a Fourier transform (as defined in (A.1)), the following equation is obtained:

$$\nabla^2\hat{\mathbf{u}}_\mathrm{P} = -k_\mathrm{P}^2\hat{\mathbf{u}}_\mathrm{P} \tag{2.16}$$

where $\nabla^2 = \partial^2/\partial x^2 + \partial^2/\partial z^2$ is the two-dimensional Laplace-operator, and $k_\mathrm{P} = \omega/C_\mathrm{P}$ is the compressional wave number. A hat on the variable denotes a variable in the frequency domain. Further transforming the coordinate x to the horizontal wavenumber k_x in Equation (2.16) by means of a second Fourier transform (as defined in appendix (A.3)), the following equation is obtained:

$$\frac{\mathrm{d}^2\tilde{\mathbf{u}}_\mathrm{P}}{\mathrm{d}z^2} = -k_{\mathrm{P}z}^2\tilde{\mathbf{u}}_\mathrm{P} \tag{2.17}$$

where the tilde on the top of a variable denotes a variable in the frequency-wavenumber domain, and

$$k_{\mathrm{P}z}^2 = k_\mathrm{P}^2 - k_x^2 \tag{2.18}$$

is the dispersion relation for the compressional wave. A solution of equation (2.17) can be written in the form

$$\tilde{\mathbf{u}}_\mathrm{P} = \mathbf{A}_\mathrm{P}\mathrm{e}^{-\mathrm{i}k_{\mathrm{P}z}z} \tag{2.19}$$

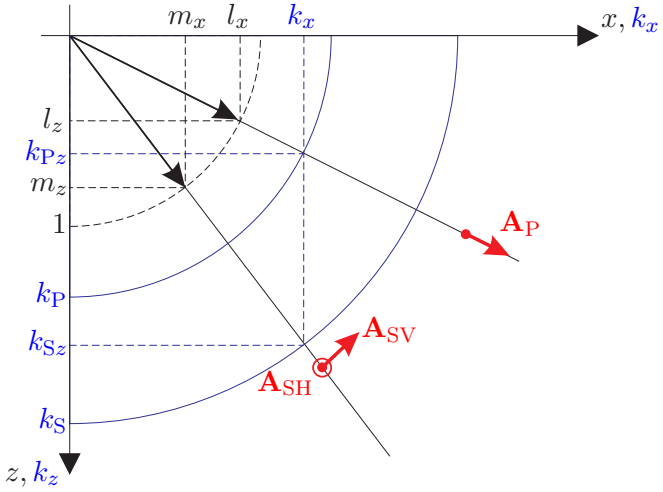

Figure 2.1: Displacements associated with the P and S waves

where the vector $\mathbf{A}_{\mathrm{P}}$ describes the amplitude of a compressional plane wave. According to the dispersion relation (2.18), the vertical wave number $k_{\mathrm{P}z}$ can be defined as

$$k_{\mathrm{P}z} = \sqrt{k_{\mathrm{P}}^2 - k_x^2} \tag{2.20}$$

for the case of $k_{\mathrm{P}}^2 - k_x^2 > 0$. In this case, (2.19) describes a plane wave propagating toward the positive z direction. The direction of propagation of the plane wave is given by the unit vector $\mathbf{l} = \{l_x, 0, l_z\}^{\mathrm{T}}$, the elements of which satisfy the equations:

$$k_x = l_x k_{\mathrm{P}} \tag{2.21a}$$
$$k_{\mathrm{P}z} = l_z k_{\mathrm{P}} \tag{2.21b}$$

Taking into account that the wave is pure compressional, the direction of propagation $\mathbf{l}$ and the direction of the wave amplitude vector are the same:

$$\mathbf{A}_P = \mathbf{l} A_{\mathrm{P}} \tag{2.22}$$

where A_{P} denotes the scalar P-wave amplitude. This is shown in figure 2.1.

For the case of $k_{\mathrm{P}}^2 - k_x^2 < 0$, the dispersion relation can be given as

$$k_{\mathrm{P}z} = -i\sqrt{k_x^2 - k_{\mathrm{P}}^2} \tag{2.23}$$

In this case, (2.19) describes evanescent waves with exponentially decreasing amplitude in the positive z direction.

Analogously, a Fourier transform of equation (2.14) from the time to the frequency domain leads to the equation:

$$\nabla^2 \hat{\mathbf{u}}_{\mathrm{S}} = -k_{\mathrm{S}}^2 \hat{\mathbf{u}}_{\mathrm{S}} \tag{2.24}$$

where $k_{\mathrm{S}} = \omega / C_{\mathrm{S}}$ denotes the shear wave number. A second Fourier transform of equation (2.24) from the space x to the wavenumber k_x domain results in

$$\frac{\mathrm{d}^2 \tilde{\mathbf{u}}_{\mathrm{S}}}{\mathrm{d}z^2} = -k_{\mathrm{S}z}^2 \tilde{\mathbf{u}}_{\mathrm{S}} \tag{2.25}$$

where

$$k_{\mathrm{P}z}^2 = k_{\mathrm{P}}^2 - k_x^2 \tag{2.26}$$

is the dispersion relation for the shear wave. A solution of equation (2.25) can be written in the form

$$\tilde{\mathbf{u}}_{\mathrm{S}} = \mathbf{A}_{\mathrm{S}} \mathrm{e}^{-\mathrm{i}k_{\mathrm{S}z}z} \tag{2.27}$$

where the vector $\mathbf{A}_{\mathrm{S}}$ describes the amplitude of a shear plane wave. According to the dispersion relation (2.26), the vertical shear wave number $k_{\mathrm{S}z}$ can be defined as

$$k_{\mathrm{S}z} = \sqrt{k_{\mathrm{S}}^2 - k_x^2} \tag{2.28}$$

for the case of $k_{\mathrm{S}}^2 - k_x^2 > 0$. In this case, (2.27) describes a plane wave propagating toward the positive z direction. The direction of propagation of the plane wave is given by the unit vector $\mathbf{m} = \{m_x, 0, m_z\}^{\mathrm{T}}$, the elements of which satisfy the equations:

$$k_x = m_x k_{\mathrm{S}} \tag{2.29a}$$

$$k_{\mathrm{S}z} = m_z k_{\mathrm{S}} \tag{2.29b}$$

As the shear wave is non-divergent, the wave amplitude vector $\mathbf{A}_{\mathrm{S}}$ is perpendicular to the direction of propagation $\mathbf{m}$. The shear wave can be further decomposed into a horizontally and a vertically polarized shear wave:

$$\mathbf{A}_{\mathrm{S}} = \mathbf{A}_{\mathrm{SH}} + \mathbf{A}_{\mathrm{SV}} \tag{2.30}$$

where the wave amplitude vector of the SH-wave is perpendicular to the xz plane and the direction of propagation $\mathbf{m}$:

$$\mathbf{A}_{\mathrm{SH}} \times \mathbf{e}_y = \mathbf{0} \tag{2.31a}$$

$$\mathbf{A}_{\mathrm{SH}} \mathbf{m} = 0 \tag{2.31b}$$

Despite its name, the SV wave is not pure vertically polarized. Its wave amplitude is perpendicular to the SH-wave and the direction of propagation $\mathbf{m}$:

$$\mathbf{A}_{\mathrm{SV}} \mathbf{A}_{\mathrm{SH}} = 0 \tag{2.32a}$$

$$\mathbf{A}_{\mathrm{SV}} \mathbf{m} = 0 \tag{2.32b}$$

Using these conditions, it is obtained that:

$$\mathbf{A}_{\mathrm{SH}} = \mathbf{e}_y A_{\mathrm{SH}} \tag{2.33}$$

and

$$\mathbf{A}_{\mathrm{SV}} = \begin{Bmatrix} m_z \\ -m_x \end{Bmatrix} A_{\mathrm{SV}} \tag{2.34}$$

where A_{SH} and A_{SV} denote the scalar amplitude of the SH and SV waves. This is shown in figure 2.1.

For the case of $k_{\mathrm{S}}^2 - k_x^2 < 0$, the dispersion relation is given as

$$k_{\mathrm{S}z} = -i\sqrt{k_x^2 - k_{\mathrm{S}}^2} \tag{2.35}$$

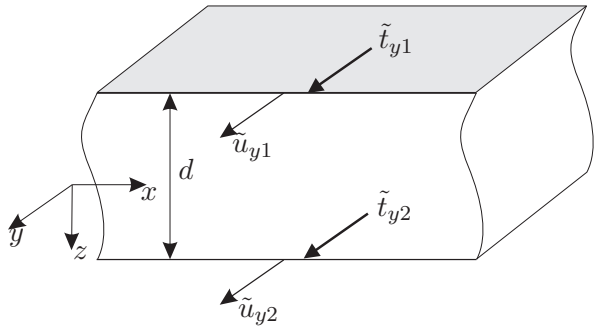

Figure 2.2: Definition of surface tractions and displacements in the layer element for the case of the out-of-plane motion

and (2.27) describes evanescent waves with exponentially decreasing amplitude in the positive z direction.

The total displacement solution $\tilde{\mathbf{u}} = \{\tilde{u}_x, \tilde{u}_y, \tilde{u}_z\}^{\mathrm{T}}$ in the wavenumber domain, for a given horizontal wave number k_x can be written as:

$$\tilde{u}_x = l_x A_{\mathrm{P}} \mathrm{e}^{-\mathrm{i}k_{\mathrm{P}z}z} + m_z A_{\mathrm{SV}} \mathrm{e}^{-\mathrm{i}k_{\mathrm{S}z}z} \tag{2.36a}$$

$$\tilde{u}_y = A_{\mathrm{SH}} \mathrm{e}^{-\mathrm{i}k_{\mathrm{S}z}z} \tag{2.36b}$$

$$\tilde{u}_z = l_z A_{\mathrm{P}} \mathrm{e}^{-\mathrm{i}k_{\mathrm{P}z}z} - m_x A_{\mathrm{SV}} \mathrm{e}^{-\mathrm{i}k_{\mathrm{S}z}z} \tag{2.36c}$$

In the two-dimensional case, the out-of-plane shear traction t_y excites only shear displacements u_y, and the in-plane tractions t_x and t_z give rise only to in-plane displacements u_x and u_z. Therefore, it is useful to handle the out-of-plane and in-plane vibration propagation cases separately.

2.4.1 The dynamic stiffness matrix for the out-of-plane motion

Dynamic stiffness matrix of a layer

The horizontal homogeneous soil layer, shown in figure 2.2, is the basic element of a layered half space model. In the layer, where vibrations can be reflected from the lower boundary, the plane wave solution (2.36b) has to be extended with a second term describing wave propagation toward the negative z direction as:

$$\tilde{u}_y = A_{\mathrm{SH}} \mathrm{e}^{-\mathrm{i}k_{\mathrm{P}z}z} + B_{\mathrm{SH}} \mathrm{e}^{\mathrm{i}k_{\mathrm{P}z}z} \tag{2.37}$$

The vibration state of the layer is determined by two boundary conditions, chosen from the two displacements $\tilde{u}_{y1}$ and $\tilde{u}_{y1}$ or the two tractions $\tilde{t}_{y1}$ and $\tilde{t}_{y1}$ at the two boundaries of the layer. The displacements

$$\tilde{u}_{y1} = \tilde{u}_y|_{z=-\frac{d}{2}} \tag{2.38a}$$

$$\tilde{u}_{y2} = \tilde{u}_y|_{z=+\frac{d}{2}} \tag{2.38b}$$

can be expressed in terms of the wave amplitudes as:

$$\begin{Bmatrix} \tilde{u}_{y1} \\ \tilde{u}_{y2} \end{Bmatrix} = \left[\tilde{\mathbf{U}}^{\mathrm{L}}_{\mathrm{SH}}\right] \begin{Bmatrix} A_{\mathrm{SH}} \\ B_{\mathrm{SH}} \end{Bmatrix} \tag{2.39}$$

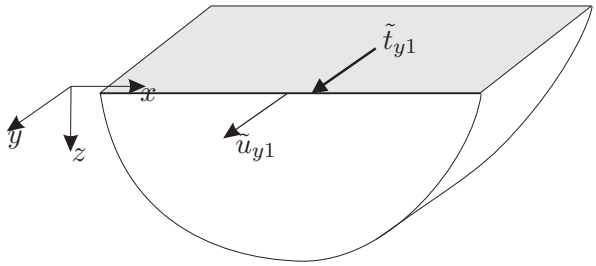

Figure 2.3: Definition of surface tractions and displacements in the half space element for the case of the out-of-plane motion

where

$$\left[\tilde{\mathbf{U}}^{\mathrm{L}}_{\mathrm{SH}}\right] = \begin{bmatrix} \mathrm{e}^{\mathrm{i}k_{\mathrm{P}z}d/2} & \mathrm{e}^{-\mathrm{i}k_{\mathrm{P}z}d/2} \\ \mathrm{e}^{-\mathrm{i}k_{\mathrm{P}z}d/2} & \mathrm{e}^{\mathrm{i}k_{\mathrm{P}z}d/2} \end{bmatrix} \tag{2.40}$$

The out-of-plane traction components at the upper and lower end of the layer can be expressed as:

$$\tilde{t}_{y1} = -\mu \left.\frac{\mathrm{d}\tilde{u}_y}{\mathrm{d}z}\right|_{z=-\frac{d}{2}} \tag{2.41a}$$

$$\tilde{t}_{y2} = \mu \left.\frac{\mathrm{d}\tilde{u}_y}{\mathrm{d}z}\right|_{z=+\frac{d}{2}} \tag{2.41b}$$

Substituting the solution (2.37) into these boundary conditions, the following expression for the tractions is obtained:

$$\begin{Bmatrix} \tilde{t}_{y1} \\ \tilde{t}_{y2} \end{Bmatrix} = \left[\tilde{\mathbf{T}}^{\mathrm{L}}_{\mathrm{SH}}\right] \begin{Bmatrix} A_{\mathrm{SH}} \\ B_{\mathrm{SH}} \end{Bmatrix} \tag{2.42}$$

where

$$\tilde{\mathbf{T}}^{\mathrm{L}}_{\mathrm{SH}} = \mu \mathrm{i}k_{\mathrm{P}z} \begin{bmatrix} \mathrm{e}^{\mathrm{i}k_{\mathrm{P}z}d/2} & -\mathrm{e}^{-\mathrm{i}k_{\mathrm{P}z}d/2} \\ -\mathrm{e}^{-\mathrm{i}k_{\mathrm{P}z}d/2} & \mathrm{e}^{\mathrm{i}k_{\mathrm{P}z}d/2} \end{bmatrix} \tag{2.43}$$

The layer's out-of-plane dynamic stiffness matrix $\tilde{\mathbf{S}}^{\mathrm{L}}_{\mathrm{SH}}$, defined by the equation

$$\begin{Bmatrix} \tilde{t}_{y1} \\ \tilde{t}_{y2} \end{Bmatrix} = \left[\tilde{\mathbf{S}}^{\mathrm{L}}_{\mathrm{SH}}\right] \begin{Bmatrix} \tilde{u}_{y1} \\ \tilde{u}_{y2} \end{Bmatrix} \tag{2.44}$$

can be then computed as

$$\tilde{\mathbf{S}}^{\mathrm{L}}_{\mathrm{SH}} = \tilde{\mathbf{T}}^{\mathrm{L}}_{\mathrm{SH}} \, \tilde{\mathbf{U}}^{\mathrm{L}}_{\mathrm{SH}}{}^{-1} = \frac{\mu k_{\mathrm{P}z}}{\sin k_{\mathrm{P}z}d} \begin{bmatrix} \cos k_{\mathrm{P}z}d & -1 \\ -1 & \cos k_{\mathrm{P}z}d \end{bmatrix} \tag{2.45}$$

Dynamic stiffness matrix of a half-space

The lowest element of a layered half-space model is a half space element, as shown in figure 2.3. In a half space excited on its boundary, only outgoing waves can be generated, so the incoming waves can be excluded from the solution set:

$$B_{\mathrm{SH}} = 0 \tag{2.46}$$

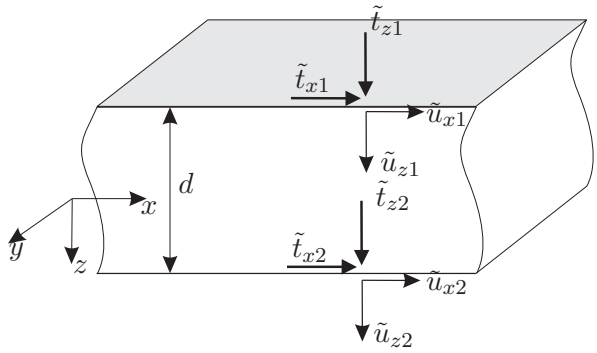

Figure 2.4: Definition of surface tractions and displacements in the layer element for the case of the in-plane motion

The relation of the boundary displacement

$$\tilde{u}_{y1} = \tilde{u}_y|_{z=0} \tag{2.47}$$

and the SH wave amplitude A_{SH} can be expressed as:

$$\tilde{u}_{y1} = A_{\mathrm{SH}} \tag{2.48}$$

while the boundary traction $\tilde{t}_{y1}$ can be expressed as

$$\tilde{t}_{y1} = \mu \frac{\mathrm{d}\tilde{u}_y}{\mathrm{d}z}\bigg|_{z=0} = \mu \mathrm{i} k_{\mathrm{P}z} A_{\mathrm{SH}} \tag{2.49}$$

The half-space element's out-of-plane stiffness $\tilde{S}^{\mathrm{R}}_{\mathrm{SH}}$, defined by

$$\tilde{t}_{y1} = \tilde{S}^{\mathrm{R}}_{\mathrm{SH}} \tilde{u}_{y1} \tag{2.50}$$

can then be expressed as

$$\tilde{S}^{\mathrm{R}}_{\mathrm{SH}} = \mu \mathrm{i} k_{\mathrm{P}z} \tag{2.51}$$

2.4.2 Dynamic stiffness matrix for the in-plane motion

Dynamic stiffness matrix of a layer

For the case of a soil layer undergoing in-plane excitation, the solution given in equations (2.36a,2.36c) has to be extended with plane waves propagating in the negative z direction:

$$\tilde{u}_x = l_x \left(A_{\mathrm{P}} \mathrm{e}^{-\mathrm{i}k_{\mathrm{P}z}z} + B_{\mathrm{P}} \mathrm{e}^{\mathrm{i}k_{\mathrm{P}z}z} \right) + m_z \left(A_{\mathrm{SV}} \mathrm{e}^{-\mathrm{i}k_{\mathrm{S}z}z} + B_{\mathrm{SV}} \mathrm{e}^{\mathrm{i}k_{\mathrm{S}z}z} \right) \tag{2.52a}$$

$$\tilde{u}_z = l_z \left(A_{\mathrm{P}} \mathrm{e}^{-\mathrm{i}k_{\mathrm{P}z}z} + B_{\mathrm{P}} \mathrm{e}^{\mathrm{i}k_{\mathrm{P}z}z} \right) - m_x \left(A_{\mathrm{SV}} \mathrm{e}^{-\mathrm{i}k_{\mathrm{S}z}z} + B_{\mathrm{SV}} \mathrm{e}^{\mathrm{i}k_{\mathrm{S}z}z} \right) \tag{2.52b}$$

The vibrational state of the soil layer is defined by four boundary conditions chosen from four displacements (two components on two sides) or four tractions. The displacement

boundary conditions are expressed as:

$$\tilde{u}_{x1} = \tilde{u}_x|_{z=-\frac{d}{2}} \tag{2.53a}$$

$$\tilde{u}_{z1} = \tilde{u}_z|_{z=-\frac{d}{2}} \tag{2.53b}$$

$$\tilde{u}_{x2} = \tilde{u}_x|_{z=\frac{d}{2}} \tag{2.53c}$$

$$\tilde{u}_{z2} = \tilde{u}_z|_{z=\frac{d}{2}} \tag{2.53d}$$

Substituting the total in-plane displacement expression (2.52b) into the boundary conditions, the following relationship between the displacements and the wave amplitudes can be written:

$$\begin{Bmatrix} \tilde{u}_{x1} \\ \tilde{u}_{z1} \\ \tilde{u}_{x2} \\ \tilde{u}_{z2} \end{Bmatrix} = \left[\tilde{\mathbf{U}}^{\mathrm{L}}_{\mathrm{P-SV}}\right] \begin{Bmatrix} A_{\mathrm{P}} \\ B_{\mathrm{P}} \\ A_{\mathrm{SV}} \\ B_{\mathrm{SV}} \end{Bmatrix} \tag{2.54}$$

For the case of the in-plane motion, the relationship between the in-plane stresses and the displacements are given by:

$$\tilde{\sigma}_{xz} = \mu\left(\frac{\mathrm{d}\tilde{u}_x}{\mathrm{d}z} - ik_x\tilde{u}_z\right) \tag{2.55a}$$

$$\tilde{\sigma}_{zz} = \lambda\left(-ik_x\tilde{u}_x + \frac{\mathrm{d}\tilde{u}_z}{\mathrm{d}z}\right) + 2\mu\frac{\mathrm{d}\tilde{u}_z}{\mathrm{d}z} \tag{2.55b}$$

According to equation (2.6), the traction boundary conditions can be defined as:

$$\tilde{t}_{x1} = -\tilde{\sigma}_{xz}|_{z=-\frac{d}{2}} \tag{2.56a}$$

$$\tilde{t}_{z1} = -\tilde{\sigma}_{zz}|_{z=-\frac{d}{2}} \tag{2.56b}$$

$$\tilde{t}_{x2} = \tilde{\sigma}_{xz}|_{z=\frac{d}{2}} \tag{2.56c}$$

$$\tilde{t}_{z2} = \tilde{\sigma}_{zz}|_{z=\frac{d}{2}} \tag{2.56d}$$

Substituting the displacement expressions into these boundary conditions, the following relationship between the tractions and the wave amplitudes is obtained:

$$\begin{Bmatrix} \tilde{t}_{x1} \\ \tilde{t}_{z1} \\ \tilde{t}_{x2} \\ \tilde{t}_{z2} \end{Bmatrix} = \left[\tilde{\mathbf{T}}^{\mathrm{L}}_{\mathrm{P-SV}}\right] \begin{Bmatrix} A_{\mathrm{P}} \\ B_{\mathrm{P}} \\ A_{\mathrm{SV}} \\ B_{\mathrm{SV}} \end{Bmatrix} \tag{2.57}$$

The layer element's in-plane dynamic stiffness matrix, defined by the equation

$$\begin{Bmatrix} \tilde{t}_{x1} \\ \mathrm{i}\tilde{t}_{z1} \\ \tilde{t}_{x2} \\ \mathrm{i}\tilde{t}_{z2} \end{Bmatrix} = \left[\tilde{\mathbf{S}}^{\mathrm{L}}_{\mathrm{P-SV}}\right] \begin{Bmatrix} \tilde{u}_{x1} \\ \mathrm{i}\tilde{u}_{z1} \\ \tilde{u}_{x2} \\ \mathrm{i}\tilde{u}_{z2} \end{Bmatrix} \tag{2.58}$$

can then be expressed as

$$\tilde{\mathbf{S}}^{\mathrm{L}}_{\mathrm{P-SV}} = \mathbf{D}\tilde{\mathbf{T}}^{\mathrm{L}}_{\mathrm{P-SV}}\ \tilde{\mathbf{U}}^{\mathrm{L}}_{\mathrm{P-SV}}{}^{-1}\ \mathbf{D}^{-1} \tag{2.59}$$

where $\mathbf{D} = \mathrm{diag}\left\{1 \quad \mathrm{i} \quad 1 \quad \mathrm{i}\right\}$. The transformation matrix $\mathbf{D}$ is used to ensure the symmetry of the stiffness matrix. The elements of $\tilde{\mathbf{S}}^{\mathrm{L}}_{\mathrm{P-SV}}$ are given in the appendix B.1.

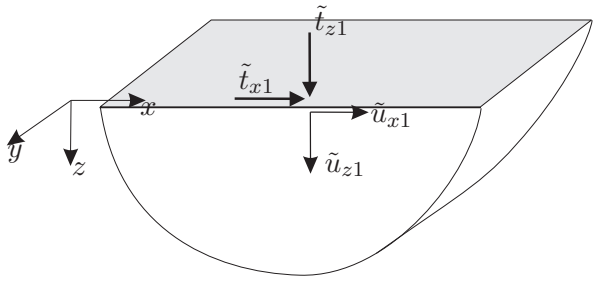

Figure 2.5: Definition of surface tractions and displacements in the layer element for the case of the in-plane motion

Dynamic stiffness matrix of a half-space

The half space element under in-plane excitation on the boundary is displayed in figure 2.5. For the case of this element, the incoming waves are suppressed:

$$B_{\mathrm{P}} = 0 \tag{2.60a}$$
$$B_{\mathrm{SV}} = 0 \tag{2.60b}$$

The boundary conditions are chosen from the two displacement and two traction components on the boundary of the half space:

$$\tilde{u}_{x1} = \tilde{u}_x|_{z=0} \tag{2.61a}$$
$$\tilde{u}_{z1} = \tilde{u}_z|_{z=0} \tag{2.61b}$$
$$\tilde{t}_{x1} = -\tilde{\sigma}_{xz}|_{z=0} \tag{2.61c}$$
$$\tilde{t}_{z1} = -\tilde{\sigma}_{zz}|_{z=0} \tag{2.61d}$$

resulting in the matrix equations:

$$\begin{Bmatrix} \tilde{u}_{x1} \\ \tilde{u}_{z1} \end{Bmatrix} = \left[\tilde{\mathbf{U}}^{\mathrm{R}}_{\mathrm{P-SV}}\right] \begin{Bmatrix} A_{\mathrm{P}} \\ A_{\mathrm{SV}} \end{Bmatrix} \tag{2.62}$$

for the displacements and

$$\begin{Bmatrix} \tilde{t}_{x1} \\ \tilde{t}_{z1} \end{Bmatrix} = \left[\tilde{\mathbf{T}}^{\mathrm{R}}_{\mathrm{P-SV}}\right] \begin{Bmatrix} A_{\mathrm{P}} \\ A_{\mathrm{SV}} \end{Bmatrix} \tag{2.63}$$

for the tractions. The in-plane dynamic stiffness matrix of the half space is defined by

$$\begin{Bmatrix} \tilde{t}_{x1} \\ \mathrm{i}\tilde{t}_{z1} \end{Bmatrix} = \left[\tilde{\mathbf{S}}^{\mathrm{R}}_{\mathrm{P-SV}}\right] \begin{Bmatrix} \tilde{u}_{x1} \\ \mathrm{i}\tilde{u}_{z1} \end{Bmatrix} \tag{2.64}$$

where

$$\tilde{\mathbf{S}}^{\mathrm{R}}_{\mathrm{P-SV}} = \mathbf{D}\tilde{\mathbf{T}}^{\mathrm{R}}_{\mathrm{P-SV}}\ {\tilde{\mathbf{U}}^{\mathrm{R}}_{\mathrm{P-SV}}}^{-1}\ \mathbf{D}^{-1} \tag{2.65}$$

and $\mathbf{D} = \mathrm{diag}\left\{1 \quad \mathrm{i}\right\}$ is used to ensure the symmetry of the stiffness matrix. The matrix elements are given in appendix B.2.

2.4.3 Dynamic stiffness matrix of a layered half-space

A layered half space is built up of a number of N homogeneous soil layers resting on a homogeneous half space. The state of the i-th layer is described by the displacements $\tilde{\mathbf{u}}_1^{(i)}$ and $\tilde{\mathbf{u}}_2^{(i)}$ and the tractions $\tilde{\mathbf{t}}_1^{(i)}$ and $\tilde{\mathbf{t}}_2^{(i)}$, where the indices 1 and 2 correspond to the upper and lower boundary of the layer, respectively:

$$\tilde{\mathbf{u}}_1^{(i)} = \left\{ \tilde{u}_{x1}^{(i)} \quad \tilde{u}_{y1}^{(i)} \quad \mathrm{i}\tilde{u}_{z1}^{(i)} \right\}^{\mathrm{T}} \tag{2.66a}$$

$$\tilde{\mathbf{u}}_2^{(i)} = \left\{ \tilde{u}_{x2}^{(i)} \quad \tilde{u}_{y2}^{(i)} \quad \mathrm{i}\tilde{u}_{z2}^{(i)} \right\}^{\mathrm{T}} \tag{2.66b}$$

$$\tilde{\mathbf{t}}_1^{(i)} = \left\{ \tilde{t}_{x1}^{(i)} \quad \tilde{t}_{y1}^{(i)} \quad \mathrm{i}\tilde{t}_{z1}^{(i)} \right\}^{\mathrm{T}} \tag{2.66c}$$

$$\tilde{\mathbf{t}}_2^{(i)} = \left\{ \tilde{t}_{x2}^{(i)} \quad \tilde{t}_{y2}^{(i)} \quad \mathrm{i}\tilde{t}_{z2}^{(i)} \right\}^{\mathrm{T}} \tag{2.66d}$$

according to these notations, the total 6×6 dynamic stiffness matrix $\tilde{\mathbf{S}}^{\mathrm{L}(i)}$ of the i-th layer, defined by

$$\begin{Bmatrix} \tilde{\mathbf{t}}_1^{(i)} \\ \tilde{\mathbf{t}}_2^{(i)} \end{Bmatrix} = \left[\tilde{\mathbf{S}}^{\mathrm{L}(i)} \right] \begin{Bmatrix} \tilde{\mathbf{u}}_1^{(i)} \\ \tilde{\mathbf{u}}_2^{(i)} \end{Bmatrix} \tag{2.67}$$

can be written as

$$\left[\tilde{\mathbf{S}}^{\mathrm{L}(i)} \right] = \begin{bmatrix} \tilde{\mathbf{S}}_{11}^{\mathrm{L}(i)} & \tilde{\mathbf{S}}_{12}^{\mathrm{L}(i)} \\ \tilde{\mathbf{S}}_{21}^{\mathrm{L}(i)} & \tilde{\mathbf{S}}_{22}^{\mathrm{L}(i)} \end{bmatrix} \tag{2.68}$$

$$= \left[\begin{array}{ccc|ccc} \tilde{S}_{\mathrm{P-SV}_{11}}^{\mathrm{L}(i)} & 0 & \tilde{S}_{\mathrm{P-SV}_{12}}^{\mathrm{L}(i)} & \tilde{S}_{\mathrm{P-SV}_{13}}^{\mathrm{L}(i)} & 0 & \tilde{S}_{\mathrm{P-SV}_{14}}^{\mathrm{L}(i)} \\ 0 & \tilde{S}_{\mathrm{SH}_{11}}^{\mathrm{L}(i)} & 0 & 0 & \tilde{S}_{\mathrm{SH}_{12}}^{\mathrm{L}(i)} & 0 \\ \tilde{S}_{\mathrm{P-SV}_{21}}^{\mathrm{L}(i)} & 0 & \tilde{S}_{\mathrm{P-SV}_{22}}^{\mathrm{L}(i)} & \tilde{S}_{\mathrm{P-SV}_{23}}^{\mathrm{L}(i)} & 0 & \tilde{S}_{\mathrm{P-SV}_{24}}^{\mathrm{L}(i)} \\ \hline \tilde{S}_{\mathrm{P-SV}_{31}}^{\mathrm{L}(i)} & 0 & \tilde{S}_{\mathrm{P-SV}_{32}}^{\mathrm{L}(i)} & \tilde{S}_{\mathrm{P-SV}_{33}}^{\mathrm{L}(i)} & 0 & \tilde{S}_{\mathrm{P-SV}_{34}}^{\mathrm{L}(i)} \\ 0 & \tilde{S}_{\mathrm{SH}_{21}}^{\mathrm{L}(i)} & 0 & 0 & \tilde{S}_{\mathrm{SH}_{22}}^{\mathrm{L}(i)} & 0 \\ \tilde{S}_{\mathrm{P-SV}_{41}}^{\mathrm{L}(i)} & 0 & \tilde{S}_{\mathrm{P-SV}_{42}}^{\mathrm{L}(i)} & \tilde{S}_{\mathrm{P-SV}_{43}}^{\mathrm{L}(i)} & 0 & \tilde{S}_{\mathrm{P-SV}_{44}}^{\mathrm{L}(i)} \end{array}\right] \tag{2.69}$$

The state of the half space is described by the displacement vector $\tilde{\mathbf{u}}_1^{(N+1)}$ and the traction vector $\tilde{\mathbf{t}}_1^{(N+1)}$. The 3×3 stiffness matrix of the half space defined by

$$\left\{ \tilde{\mathbf{t}}_1^{(N+1)} \right\} = \left[\tilde{\mathbf{S}}^{\mathrm{R}} \right] \left\{ \tilde{\mathbf{u}}_1^{(N+1)} \right\} \tag{2.70}$$

can be expressed as

$$\left[\tilde{\mathbf{S}}^{\mathrm{R}} \right] = \begin{bmatrix} \tilde{S}_{\mathrm{P-SV}_{11}}^{\mathrm{R}} & 0 & \tilde{S}_{\mathrm{P-SV}_{12}}^{\mathrm{R}} \\ 0 & \tilde{S}_{\mathrm{SH}}^{\mathrm{R}} & 0 \\ \tilde{S}_{\mathrm{P-SV}_{21}}^{\mathrm{R}} & 0 & \tilde{S}_{\mathrm{P-SV}_{22}}^{\mathrm{R}} \end{bmatrix} \tag{2.71}$$

The displacement continuity between adjacent layers can be expressed as

$$\tilde{\mathbf{u}}_2^{(i-1)} = \tilde{\mathbf{u}}_1^{(i)} = \tilde{\mathbf{u}}^{(i)} \tag{2.72}$$

where $\tilde{\mathbf{u}}^{(i)}$ is the displacement of the i-th boundary. The equilibrium condition between adjacent layers can be written in the form:

$$\tilde{\mathbf{t}}_2^{(i-1)} + \tilde{\mathbf{t}}_1^{(i)} = \tilde{\mathbf{t}}^{(i)} \tag{2.73}$$

where $\tilde{\mathbf{t}}^{(i)}$ denotes the traction at the i-th interface.

Using these conditions, the total dynamic stiffness matrix $\tilde{\mathbf{S}}$ of the layered half space can be assembled, that relates the interface tractions to the interface displacements as

$$\underline{\tilde{\mathbf{t}}} = \tilde{\mathbf{S}}\underline{\tilde{\mathbf{u}}} \tag{2.74}$$

Here, the vector $\underline{\tilde{\mathbf{t}}}$ collects the interface tractions $\tilde{\mathbf{t}}^{(i)}$ and $\underline{\tilde{\mathbf{u}}}$ collects the interface displacements $\tilde{\mathbf{u}}^{(i)}$. The structure of the symmetric and strongly banded stiffness matrix is shown in equation (2.75) (in figure 2.6). The matrix elements corresponding to the same degrees of freedom overlap in a finite element sense.

Using equation (2.74), a general 2D harmonic or transient problem written on a layered half space can be solved as the following: First, the boundary conditions are transformed from the space-time domain to the frequency-wavenumber domain by means of a double Fourier transform. In a second step, equation (2.74) is solved for all frequencies and wavenumbers, and finally, the response is transformed back to the space-time domain by means of a double inverse Fourier transform.

2.5 Numerical example for 2D motion

In the following, a numerical example will be considered in order to demonstrate the use of the described methodology. In the numerical example, a layered half space will be excited by a vertical strip load impulse, and the displacement response will be examined.

Two modeling cases corresponding to two site models are considered. In case 1, the soil is modeled as a homogeneous half space characterized by a shear wave velocity $C_{\mathrm{S}}^{\mathrm{R}} = 250\ \mathrm{m/s}$, compressional wave velocity $C_{\mathrm{P}}^{\mathrm{R}} = 500\ \mathrm{m/s}$, mass density $\rho^{\mathrm{R}} = 2500\ \mathrm{kg/m^3}$ and material damping $\beta^{\mathrm{R}} = 0.025$.

In case 2, the soil is modeled as a $5\ \mathrm{m}$ thick homogeneous layer resting on the same half space. The material of the layer is characterized by a shear wave velocity $C_{\mathrm{S}}^{\mathrm{L}} = 200\ \mathrm{m/s}$, compressional wave velocity $C_{\mathrm{P}}^{\mathrm{L}} = 400\ \mathrm{m/s}$, mass density $\rho^{\mathrm{L}} = 2000\ \mathrm{kg/m^3}$ and a damping coefficient $\beta^{\mathrm{L}} = 0.025$.

The surface traction vector acting on the site is defined as:

$$\mathbf{t}(x, z, t) = t_0 a(x)\delta(z)b(t)\mathbf{e}_z \tag{2.76}$$

where $t_0 = 1\ \mathrm{N/m}$ is the load amplitude. The spatial distribution of the load is given by

$$a(x) = \frac{\epsilon(x + B) - \epsilon(x - B)}{2B} \tag{2.77}$$

where $\varepsilon(x)$ denotes the step function defined as

$$\varepsilon(x) = \begin{cases} 1 & \text{if } x \geq 0 \\ 0 & \text{if } x < 0 \end{cases} \tag{2.78}$$

$$\begin{Bmatrix} \tilde{\mathbf{t}}^{(1)} \\ \tilde{\mathbf{t}}^{(2)} \\ \vdots \\ \tilde{\mathbf{t}}^{(i)} \\ \tilde{\mathbf{t}}^{(i+1)} \\ \vdots \\ \tilde{\mathbf{t}}^{(N+1)} \end{Bmatrix} = \begin{bmatrix} \tilde{\mathbf{S}}_{11}^{\mathrm{L}(1)} & \tilde{\mathbf{S}}_{12}^{\mathrm{L}(1)} & & & & & & \\ \tilde{\mathbf{S}}_{21}^{\mathrm{L}(1)} & \tilde{\mathbf{S}}_{22}^{\mathrm{L}(1)} + \tilde{\mathbf{S}}_{11}^{\mathrm{L}(2)} & \tilde{\mathbf{S}}_{12}^{\mathrm{L}(2)} & & & & & \\ & & \ddots & & & & & \\ & & \tilde{\mathbf{S}}_{21}^{\mathrm{L}(i-1)} & \tilde{\mathbf{S}}_{22}^{\mathrm{L}(i-1)} + \tilde{\mathbf{S}}_{11}^{\mathrm{L}(i)} & \tilde{\mathbf{S}}_{12}^{\mathrm{L}(i)} & & & \\ & & & \tilde{\mathbf{S}}_{21}^{\mathrm{L}(i)} & \tilde{\mathbf{S}}_{22}^{\mathrm{L}(i)} + \tilde{\mathbf{S}}_{11}^{\mathrm{L}(i+1)} & \tilde{\mathbf{S}}_{12}^{\mathrm{L}(i+1)} & & \\ & & & & & \ddots & & \\ & & & & & \tilde{\mathbf{S}}_{21}^{\mathrm{L}(N)} & \tilde{\mathbf{S}}_{22}^{\mathrm{L}(N)} + \tilde{\mathbf{S}}^{\mathrm{R}} \end{bmatrix} \begin{Bmatrix} \tilde{\mathbf{u}}^{(1)} \\ \vdots \\ \tilde{\mathbf{u}}^{(i)} \\ \tilde{\mathbf{u}}^{(i+1)} \\ \vdots \\ \tilde{\mathbf{u}}^{(N+1)} \end{Bmatrix} \tag{2.75}$$

Figure 2.6: The structure of the total dynamic stiffness matrix of a layered half space

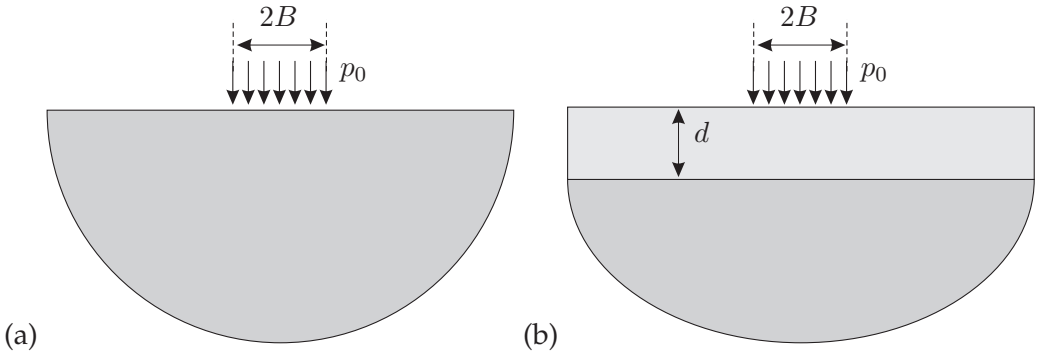

Figure 2.7: Scheme of the numerical example: (a) homogeneous half space, (b) single layer on a half space.

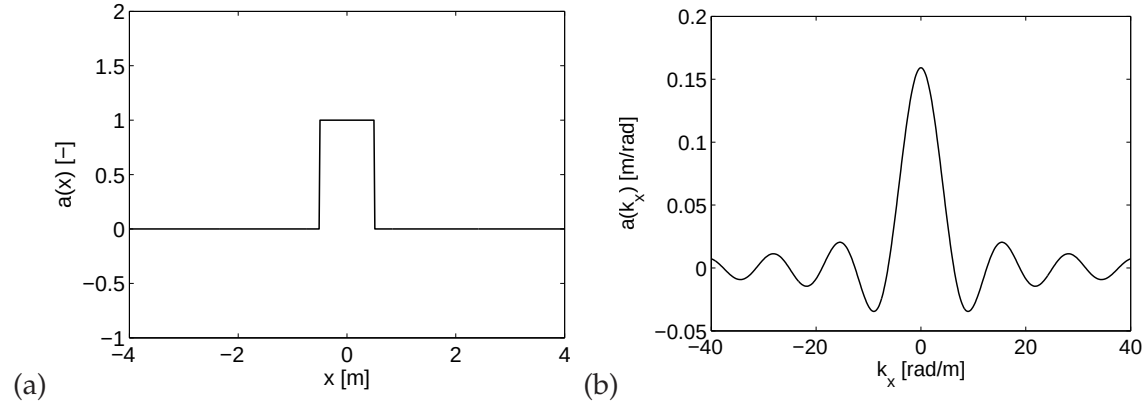

Figure 2.8: The strip load function in the (a) space and in the (b) wavenumber domain.

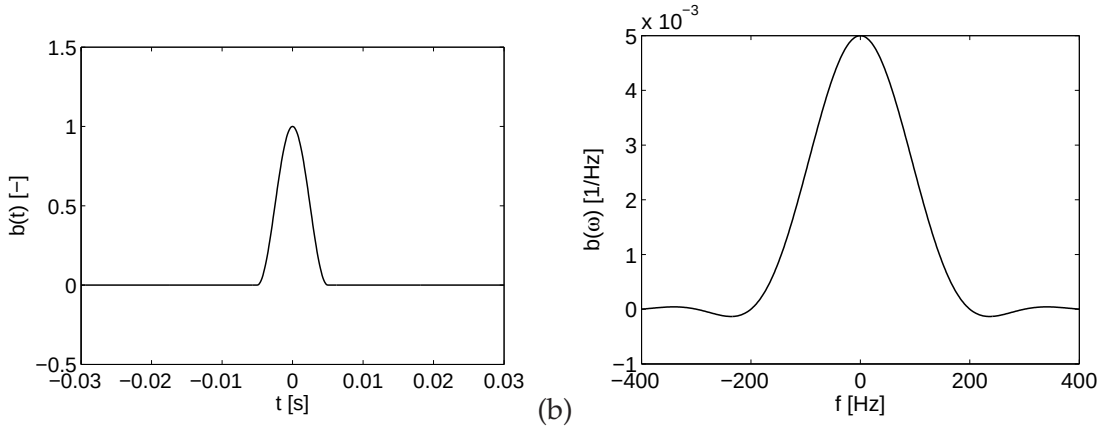

Figure 2.9: The raised cosine function in the (a) time and in the (b) frequency domain.

and $B = 0.5$ m denotes the half strip width. The function $a(x)$ is displayed in figure 2.8(a). The time history of the load $b(t)$ is a raised cosine impulse function of length $2T = 0.01$ s (shown in figure 2.9(a)) defined as:

$$b(t) = \begin{cases} \frac{1+\cos(\pi \frac{t}{T})}{2} & \text{if } |t| \leq T \\ 0 & \text{otherwise} \end{cases} \tag{2.79}$$

A double Fourier transform of the load function results in the wavenumber-frequency domain representation of the load:

$$\tilde{t}(k_x, z, \omega) = t_0 \tilde{a}(k_x) \delta(z) \hat{b}(\omega) \mathbf{e}_z \tag{2.80}$$

where

$$\tilde{a}(k_x) = \frac{\text{sinc}(k_x B)}{2\pi} \tag{2.81}$$

is the wavenumber content of the load, as shown in figure 2.8(b), and

$$\hat{b}(\omega) = T \frac{\text{sinc}(\omega T)}{1 - \left(\frac{\omega T}{\pi}\right)^2} \tag{2.82}$$

is the frequency content of the load, displayed in figure 2.9(b).

According to this loading function, the following boundary conditions can be applied in the dynamic stiffness matrix method. On the upper boundary of the layer, only the vertical traction component $\tilde{t}_z^{(1)}$ is non-zero:

$$\tilde{t}_x^{(1)} = 0 \tag{2.83a}$$
$$\tilde{t}_y^{(1)} = 0 \tag{2.83b}$$
$$\tilde{t}_z^{(1)} = p_0 \tilde{a}(k_x) \hat{b}(\omega) \tag{2.83c}$$

For the case of the layer on a half space, the loads on the interface between the layer and the half space are zero, resulting in the boundary conditions:

$$\tilde{t}_x^{(2)} = \tilde{t}_y^{(2)} = \tilde{t}_z^{(2)} = 0 \tag{2.84}$$

The dynamic stiffness matrix $\tilde{\mathbf{S}}$ of the site (given in equation (2.75)) gives the relation between the tractions and displacement response as $\tilde{\mathbf{t}} = \tilde{\mathbf{S}}\tilde{\mathbf{u}}$. By inverting this equation, the dynamic admittance matrix $\tilde{\mathbf{H}}$ of the site can be defined as $\tilde{\mathbf{u}} = \tilde{\mathbf{H}}\tilde{\mathbf{t}}$. Taking into account that the traction vector is zero except for the $\tilde{t}_z^{(1)}$ element, the vertical surface displacement $\tilde{u}_z^{(1)}$ can be expressed as

$$\tilde{u}_z^{(1)} = \tilde{h}\tilde{t}_z^{(1)} \tag{2.85}$$

where $\tilde{h}$ is one (the first) element of the matrix $\tilde{\mathbf{H}}$. The vertical surface displacement can thus be expressed as

$$\tilde{u}_z(k_x, z = 0, \omega) = \tilde{h}(k_x, \omega) p_0 \tilde{a}(k_x) \hat{b}(\omega) \tag{2.86}$$

and the vertical component of the surface velocity $v_z(k_x, 0, \omega)$ as

$$\tilde{v}_z(k_x, z = 0, \omega) = \mathrm{i}\omega \tilde{h}(k_x, \omega) p_0 \tilde{a}(k_x) \hat{b}(\omega) \tag{2.87}$$

Figure 2.10 displays the modulus of the $\tilde{h}(k_x, \omega)$ admittance function for two frequency values, $f_1 = 10$ Hz and $f_2 = 100$ Hz, versus dimensionless wave number $\bar{k} = k_x / k_{\mathrm{S}}^{\mathrm{R}}$, where $k_{\mathrm{S}}^{\mathrm{R}}$ is the shear wave number of the half space.

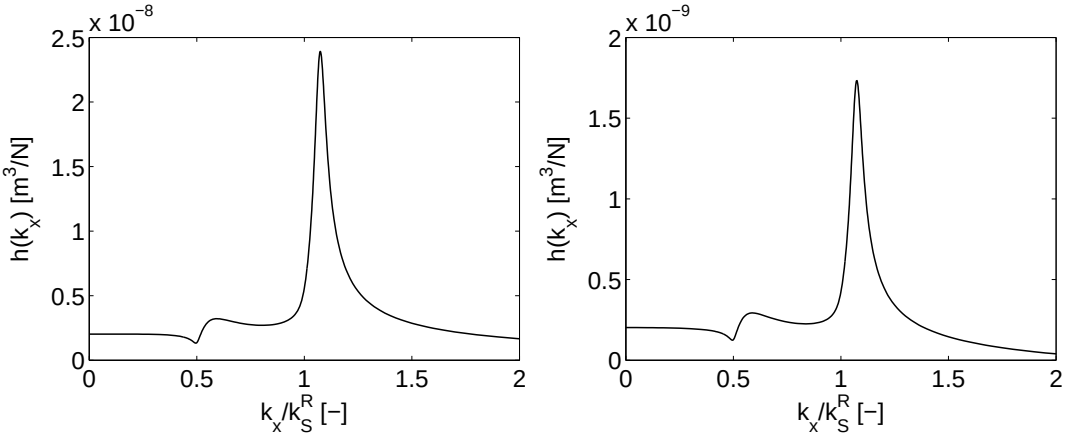

Figure 2.10: Modulus of the $\tilde{h}(k_x, \omega)$ admittance function at frequencies (a) $\omega = 2\pi \times 10$ Hz and (b) $\omega = 2\pi \times 100$ Hz, for the case of the homogeneous half space.

The curves show one sharp peak at $\bar{k} = 1.07$. As at this value $k_{\mathrm{S}}^2 - k_x^2 < 0$, this peak corresponds to an evanescent wave, the Rayleigh surface wave that propagates with a phase velocity slightly smaller than the velocity of the shear wave. The dip at the dimensionless wave number $k_x = 0.5 k_{\mathrm{S}}^{\mathrm{R}}$ corresponds to the compressional wave that propagates with a velocity $C_{\mathrm{P}} = 2C_{\mathrm{S}}$ in the current material. The dip shows that the compressional waves excited by the vertical surface strip load do not play an important role in the vertical response at the soil surface. Considering that the peaks and dips in the figures corresponding to the low and high frequency cases are at the same wavenumbers, it can be stated that both waves are non dispersive in the homogeneous half space.

Figure 2.11 shows the same admittance functions for the case of the layered half space. In the figure corresponding to the low frequency case, the peak of the Rayleigh wave at $k_x = 1.07 k^{\mathrm{R}}$ and the dip of the compressional wave at $k_x = 0.5 k_{\mathrm{S}}^{\mathrm{R}}$ can be found. The peak near the dip of the compressional wave corresponds to the second Rayleigh mode of the layered

half space. turning to the high frequency case, it can be seen that the peak of the Rayleigh wave is shifted toward higher wave number values, and several additional Rayleigh modes appear between the dip of the compressional wave and the first Rayleigh peak.

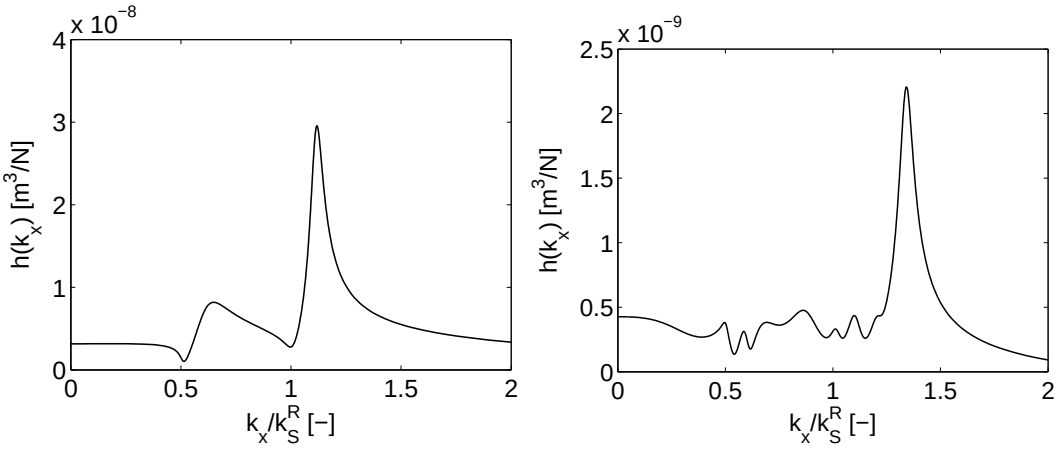

Figure 2.11: Modulus of the $\tilde{h}(k_x, \omega)$ admittance function at frequencies (a) $\omega = 2\pi \times 10$ Hz and (b) $\omega = 2\pi \times 100$ Hz, for the case of the layer on a half space.

The apparent phase velocity of the different propagating waves is given by $c_x = \omega/k_x$. Figure 2.12 displays the modulus of the admittance function $\tilde{h}(c_x, \omega)$ versus the frequency and the phase velocity. The admittance is multiplied by the frequency ω in order to emphasize the high frequencies where the curves are attenuated due to the soil's material damping. The shaded lines show the dispersion curves of the different soils. For the case of the homogeneous half space, the dispersion curve is a single horizontal line, referring to the non dispersive behavior of this soil. In the figure corresponding to the layered half space, the velocity of the Rayleigh wave is near the shear velocity of the half space at low frequencies, and reaches the shear wave velocity of the layer at higher frequencies, where the wavelength is smaller than the layer depth. The higher Rayleigh modes are also observable in the figure 2.8(b). These modes show a similar dispersive behavior.

The double inverse Fourier transform of the surface velocity $\hat{v}_z(x, \omega)$ results in the space-time representation of the vertical surface velocity $v_z(x, t)$. Figure 2.13 shows this velocity function versus the horizontal coordinate x for the case of the homogeneous half space and for different time values. The figures show that the impulse load around $x = 0$ generates impulses propagating in the positive and in the negative x direction, symmetrically. A sharp peak propagates with the velocity of the Rayleigh wave, and a small dip propagates with approximately a double propagation velocity.

Figure 2.14 shows the velocity function $v_z(x, t)$ for the case of the layer on a half space. As for the case of the homogeneous half space, a sharp peak propagates with a smaller velocity and a small dip with approximately double speed, but due to the inhomogeneous soil model, the shape of the Rayleigh impulse changes as it propagates in the positive x direction.

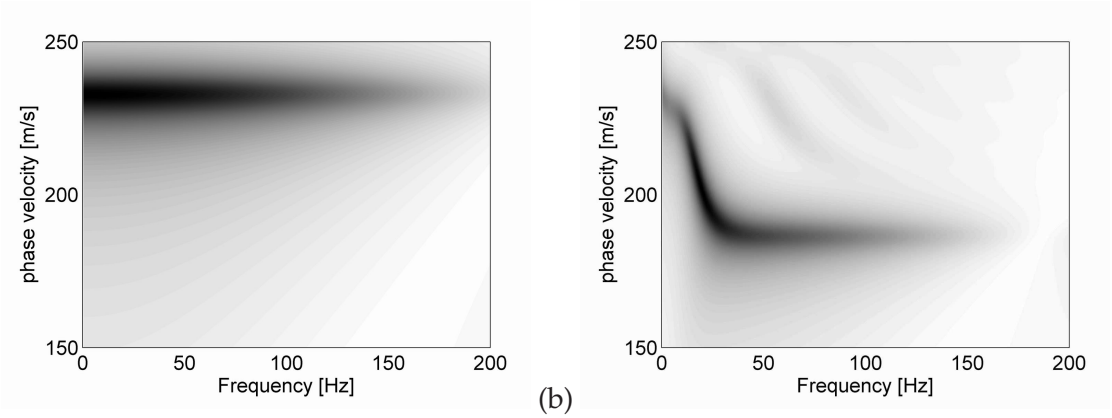

Figure 2.12: Modulus of the function $\omega\tilde{h}(c_x, \omega)$ for the case of (a) the homogeneous half space and (b) the layer on a half space.

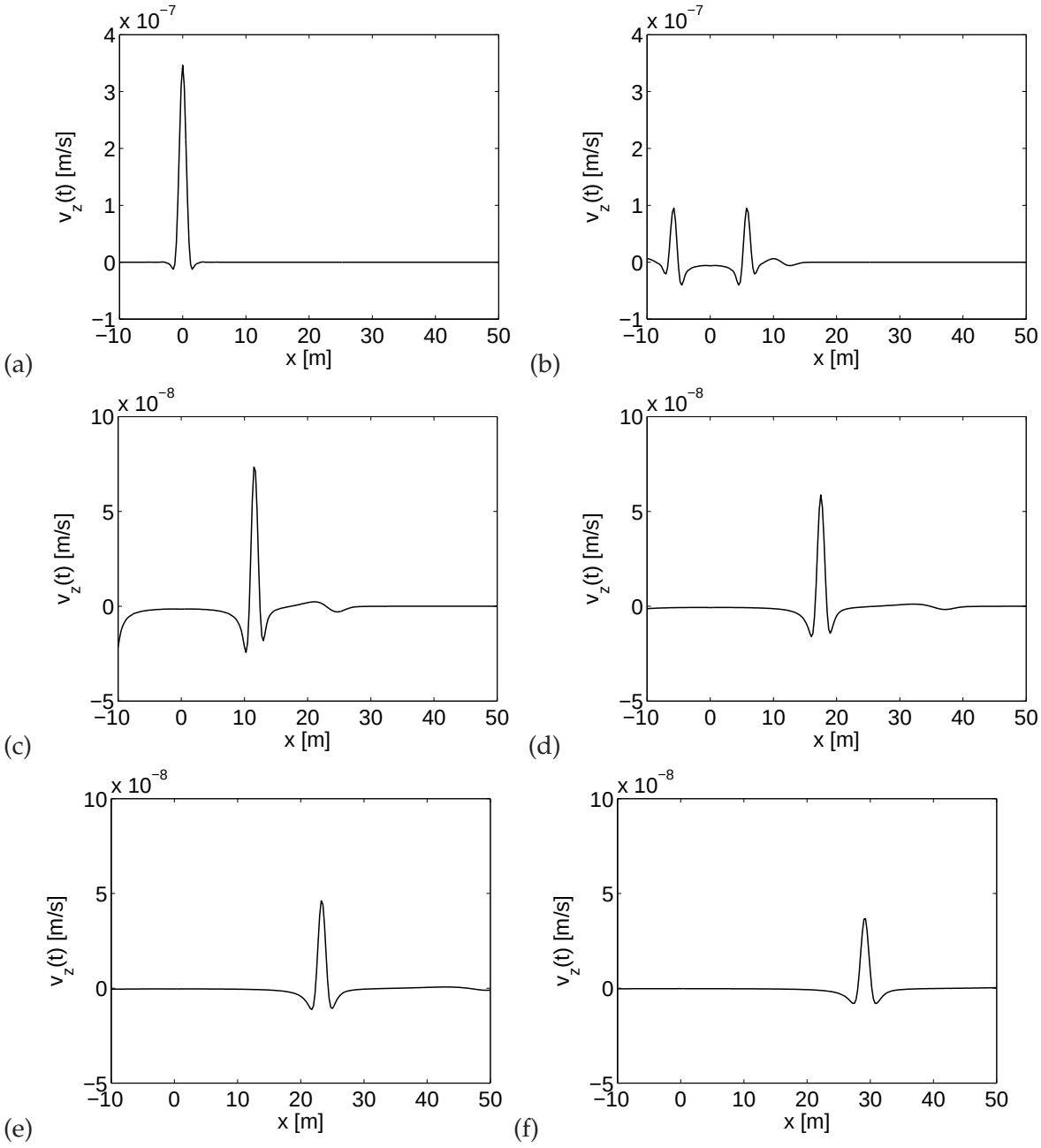

Figure 2.13: Time history of the vertical component of the surface velocity $v_z(t)$ at the surface of the homogeneous half space, at the time (a) $t = 0$ s, (b) $t = 0.025$ s, (c) $t = 0.05$ ms, (d) $t = 0.075$ ms, (e) $t = 0.1$ ms and (f) $t = 0.125$ ms.

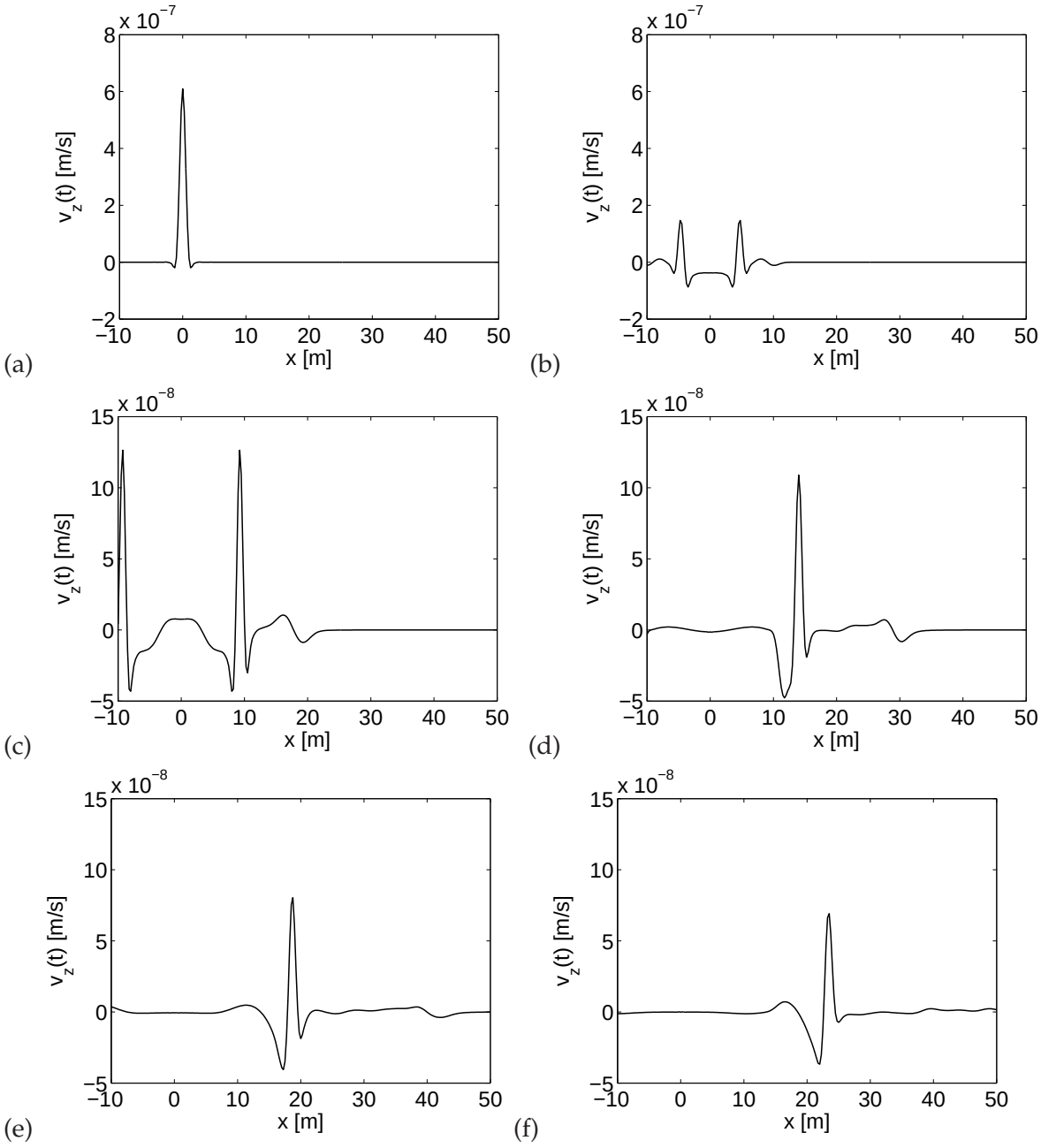

Figure 2.14: Time history of the vertical component of the surface velocity $v_z(t, x)$ at the surface of the layered half space, at the time (a) $t = 0$ s, (b) $t = 0.025$ s, (c) $t = 0.05$ ms, (d) $t = 0.075$ ms, (e) $t = 0.1$ ms and (f) $t = 0.125$ ms.

Chapter 3

Dynamic soil-structure interaction

3.1 Introduction

Using the methodology described in the previous section, the incident displacement wave field $\mathbf{u}_{\text{inc}}$ excited by tractions on the surface of a layered half space can be computed. in this section, the problem of dynamic soil-structure interaction (SSI) is tackled. This problem describes the interaction between this incident wave field and the displacements of a structure embedded in the layered soil.

Modeling of such a phenomenon is an involved task, as the soil and the structure have basically different geometrical and physical properties. The soil is an unbounded continuous medium, while the structure is finite in space, and slender in lots of the cases. The stiffness of the soil and the structure can differ by several orders of magnitude.

Based on these differences, hybrid methods have been developed for the modeling of dynamic soil-structure interaction. The family of sub-structuring methods [McN71] divides the total addressed medium into substructures, and solves the problem in each of the substructures so that continuity and equilibrium conditions are prescribed at the domain boundaries. In most of the cases related to soil-structure interaction, the two substructures are the infinite soil and the finite structure, and for the case of hybrid models, different numerical techniques are used for the modeling of wave propagation in the two substructures. Typically, the finite element method is used for the structure, and the boundary element method is used for the soil, as published by many authors: [Wol85], [], [].

More recently, domain decomposition methods, combined with substructuring have been introduced [Tal94], [FR91], [dLBFM$^+$98], [AC92], [Clo90]. The basic idea of domain decomposition is (1) to define new unknown displacement fields so that the continuity equation on the soil-structure interface a-priori holds, (2) to solve boundary value problems in each substructure using these new fields as boundary conditions, (3) and to enforce the other coupling conditions in a weak sense.

This section of the thesis introduces a substructuring method combined with domain decomposition, used to solve the dynamic SSI problem. In the current method, a boundary element method is used for the modeling of the soil domain, and a finite element method is used to model the structure. A subdomain method proposed by Aubry and Clouteau is described, and the discretized equations of dynamic SSI are derived. Finally, an efficient Component Mode Synthesis method capable to simplify the computation of the structural response is described.

3.2 The subdomain formulation

3.2.1 Basic assumptions

A weak coupling between the incident wave field and the structural vibrations is assumed. This means that the incident wave field is computed in the absence of the structure, and in a second step, the interaction between this wave field and the structural vibrations is computed in the absence of the vibration source. This assumption makes the computations easier to carry out, but, of course, can only be valid if the distance between the vibration source and the structure is large enough in terms of wavelength.

The infinite layered soil domain is displayed in figure 3.1(a). For the sake of clearness, the layer boundaries are not displayed in the figure. This soil domain is denoted by Ω_g, where the index g refers to the ground. It is assumed that the incident displacement wave field $\mathbf{u}_{\text{inc}}$ exists in this domain with zero surface tractions on the domain's boundary surface $\Gamma_{0\text{inc}}$.

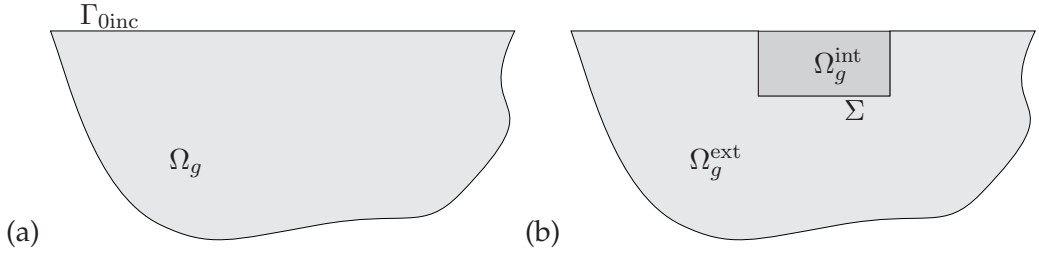

Figure 3.1: Domain definition

The ground domain Ω_g is split up into two subdomains: $\Omega_g = \Omega_g^{\text{ext}} \cup \Omega^{\text{int}}$. Ω_g^{int} denotes the soil excavation (the place of the building's foundation), Ω_g^{ext} stands for the total infinite soil domain without the excavation, as shown in figure 3.1(b). The interface between the two domains is denoted by Σ.

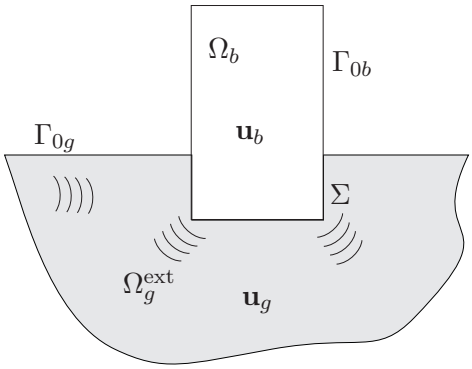

Figure 3.2: Domain definition

In figure 3.2 the external soil domain and the structural domain can be seen. The structural domain is denoted by Ω_b, the subscript b refers to the building. The building is bounded by the traction free surface Γ_{0b} and the soil-structure interface Σ, while the ground is bounded by the traction free surface Γ_{0b} and the soil structure interface.

The basic assumptions regarding the ground displacement field $\mathbf{u}_g$ and the structural displacements $\mathbf{u}_b$ are the following. The equilibrium equation (2.3) holds in the soil domain Ω_g^{ext} for the ground displacement field $\mathbf{u}_g$:

$$\nabla \cdot \boldsymbol{\sigma}(\mathbf{u}_g) + \rho \mathbf{b}_g = \rho \ddot{\mathbf{u}}_g \quad \text{in } \Omega_g^{\text{ext}} \tag{3.1}$$

The free soil surface Γ_{0g} is characterized by zero traction boundary condition:

$$\mathbf{t}_g(\mathbf{u}_g) = \mathbf{0} \quad \text{on } \Gamma_{0g} \tag{3.2}$$

The equilibrium equation (2.3) also holds in the structural domain Ω_b for the structural displacements $\mathbf{u}_b$:

$$\nabla \cdot \boldsymbol{\sigma}(\mathbf{u}_b) + \rho \mathbf{b}_b = \rho \ddot{\mathbf{u}}_b \quad \text{in } \Omega_b \tag{3.3}$$

The free structural boundary Γ_{0b} is characterized by zero traction boundary condition:

$$\mathbf{t}_b(\mathbf{u}_b) = \mathbf{0} \quad \text{on } \Gamma_{0b} \tag{3.4}$$

Displacement continuity between the soil displacements and the building displacements is assumed on the soil-structure interface Σ:

$$\mathbf{u}_g = \mathbf{u}_b \quad \text{on } \Sigma \tag{3.5}$$

On the interface, the soil and the structural tractions are in equilibrium:

$$\mathbf{t}_g(\mathbf{u}_g) + \mathbf{t}_b(\mathbf{u}_b) = \mathbf{0} \quad \text{on } \Sigma \tag{3.6}$$

3.2.2 Domain decomposition

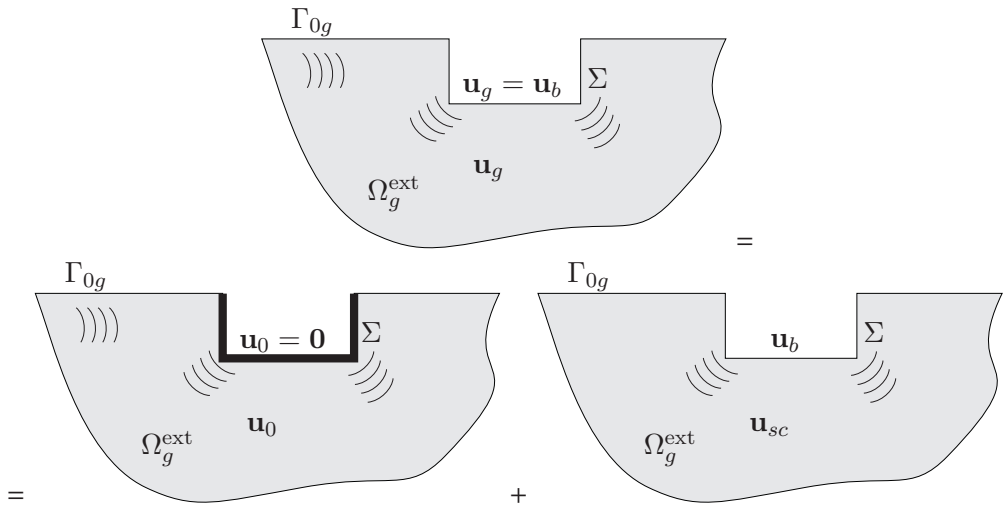

Figure 3.3: The ground displacement field $\mathbf{u}_g$ is decomposed into a displacement field $\mathbf{u}_0$ and a scattered displacement field $\mathbf{u}_{sc}$.

In the following, the domain decomposition method proposed by Aubry and Clouteau is described [AC92], [Clo90], [Clo99a], [Clo99b]. The soil displacement field $\mathbf{u}_g$ is decomposed into the sum of two displacement fields $\mathbf{u}_0$ and $\mathbf{u}_{sc}$, as shown in figure 3.3.

$$\mathbf{u}_g = \mathbf{u}_0 + \mathbf{u}_{sc}(\mathbf{u}_b) \quad \text{in } \Omega_g \tag{3.7}$$

The displacement field $\mathbf{u}_0$ contains the incident wave field and its reflections from the rigid soil-structure interface Σ:

$$\mathbf{u}_0 = \mathbf{0} \quad \text{on } \Sigma \tag{3.8}$$

The displacement field $\mathbf{u}_{sc}(\mathbf{u}_b)$ is the so-called scattered wave field which is radiated to the infinite soil domain Ω_b^{ext} due to the structural motion $\mathbf{u}_b$ at the soil-structure interface Σ:

$$\mathbf{u}_{sc}(\mathbf{u}_b) = \mathbf{u}_b \quad \text{on } \Sigma \tag{3.9}$$

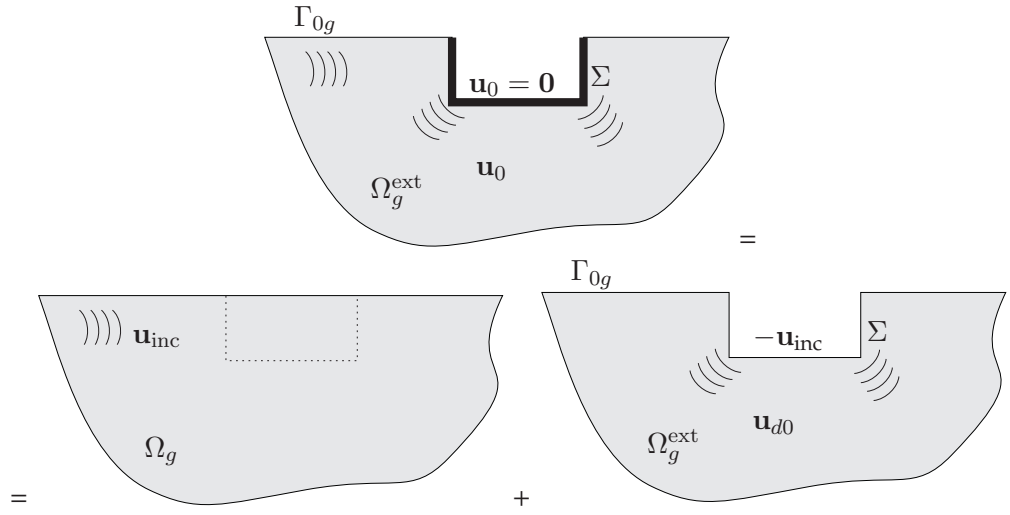

Figure 3.4: The displacement field $\mathbf{u}_0$ is decomposed into the incident wave field $\mathbf{u}_{\text{inc}}$ and a locally diffracted displacement field $\mathbf{u}_{d0}$.

The displacement field $\mathbf{u}_0$ is further decomposed into two displacement fields, the first of which is the incident wave field $\mathbf{u}_{\text{inc}}$ present in the infinite soil domain without excavation, and the second is a locally diffracted displacement field $\mathbf{u}_{d0}$ defined in the external soil domain, as shown in figure 3.4:

$$\mathbf{u}_0 = \mathbf{u}_{\text{inc}} + \mathbf{u}_{d0} \quad \text{in } \Omega_g \tag{3.10}$$

where

$$\mathbf{u}_{d0} = -\mathbf{u}_{\text{inc}} \quad \text{on } \Sigma \tag{3.11}$$

3.3 Variational formulation

The equation of motion of the dynamic soil-structure interaction problem can be derived from the principle of virtual work written to the structural domain. The principle of virtual work states that for any virtual displacement field $\mathbf{v}$ imposed on the structure, the total work of the internal and inertial forces is in equilibrium with the total work of the external loads. Writing this theorem in the frequency domain to the structural displacement field $\hat{\mathbf{u}}_b$ in the domain Ω_b results in:

$$\int_{\Omega_b} \hat{\boldsymbol{\epsilon}}(\hat{\mathbf{v}}) : \hat{\boldsymbol{\sigma}}_b(\hat{\mathbf{u}}_b) \mathrm{d}\Omega - \omega^2 \int_{\Omega_b} \hat{\mathbf{v}} \cdot \rho_b \hat{\mathbf{u}}_b \mathrm{d}\Omega = \int_{\Sigma} \hat{\mathbf{v}} \cdot \hat{\mathbf{t}}_b(\hat{\mathbf{u}}_b) \mathrm{d}\Sigma \tag{3.12}$$

where the first term on the left hand side expresses the total internal work of the flexible forces, the second term expresses the internal work made by the inertial forces, and the right hand side expresses the total external work made by the external tractions on the soil-structure interface. Here, use had been made of the zero traction condition on the free structural boundary, and zero internal structural forces $\hat{\mathbf{b}}_b = \mathbf{0}$ have been assumed.

Making use of the force equilibrium on the interface Σ, as expressed in equation (3.6), and introducing the decomposition equation (3.7), the following expression is obtained:

$$\int_{\Omega_b} \hat{\boldsymbol{\epsilon}}(\hat{\mathbf{v}}) : \hat{\boldsymbol{\sigma}}_b(\hat{\mathbf{u}}_b)\mathrm{d}\Omega - \omega^2 \int_{\Omega_b} \hat{\mathbf{v}} \cdot \rho_b \hat{\mathbf{u}}_b \mathrm{d}\Omega + \int_{\Sigma} \hat{\mathbf{v}} \cdot \hat{\mathbf{t}}_g(\hat{\mathbf{u}}_{sc}(\hat{\mathbf{u}}_b))\mathrm{d}\Sigma = -\int_{\Sigma} \hat{\mathbf{v}} \cdot \hat{\mathbf{t}}_g(\hat{\mathbf{u}}_0)\mathrm{d}\Sigma \quad (3.13)$$

In order to get the discretized form of equation (3.13), the structural and soil domains are discretized, and all the displacement fields are expressed using their nodal samples and global shape functions. For the case of the structural displacements, $\hat{\mathbf{u}}_b = \mathbf{N}_b \underline{\hat{\mathbf{u}}}_b$, where $\mathbf{N}_b$ denotes the structural shape functions and the vector $\underline{\hat{\mathbf{u}}}_b$ collects the nodal samples of the structural displacements. Similarly, for the case of a Galerkin approach, the same shape functions are used for the virtual displacement field: $\hat{\mathbf{v}} = \mathbf{N}_b \underline{\hat{\mathbf{v}}}$. If the different components of the strain tensor $\hat{\boldsymbol{\epsilon}}$ are collected in a vector $\hat{\boldsymbol{\varepsilon}} = \{\hat{\epsilon}_{xx}, \hat{\epsilon}_{yy}, \hat{\epsilon}_{zz}, \hat{\epsilon}_{xy}, \hat{\epsilon}_{yz}, \hat{\epsilon}_{zx}\}^{\mathrm{T}}$, then the strain-displacement relation (2.2) can be expressed in the form of $\hat{\boldsymbol{\varepsilon}} = \mathbf{L}\hat{\mathbf{u}}$, where the matrix $\mathbf{L}$ contains differential operators [Zie86]. Similarly, as the different elements of the stress tensor $\hat{\boldsymbol{\sigma}}$ are collected in the vector $\hat{\sigma} = \{\hat{\sigma}_{xx}, \hat{\sigma}_{yy}, \hat{\sigma}_{zz}, \hat{\sigma}_{xy}, \hat{\sigma}_{yz}, \hat{\sigma}_{zx}\}^{\mathrm{T}}$, then the stress-strain relations (2.4) can be written as $\hat{\sigma} = \mathbf{D}\hat{\varepsilon}$, where the 6×6 matrix $\mathbf{D}$ contains the Lamé coefficients. Introducing these notations, equation (3.13) can be written in the form:

$$\underline{\hat{\mathbf{v}}}^{\mathrm{T}} \int_{\Omega_b} \mathbf{N}_b^{\mathrm{T}} \mathbf{L}^{\mathrm{T}} \mathbf{D} \mathbf{L} \mathbf{N}_b \mathrm{d}\Omega \underline{\hat{\mathbf{u}}}_b - \omega^2 \underline{\hat{\mathbf{v}}}^{\mathrm{T}} \int_{\Omega_b} \mathbf{N}_b^{\mathrm{T}} \rho_b \mathbf{N}_b \mathrm{d}\Omega \underline{\hat{\mathbf{u}}}_b + \underline{\hat{\mathbf{v}}}^{\mathrm{T}} \int_{\Sigma} \mathbf{N}_b^{\mathrm{T}} \hat{\mathbf{t}}_g(\hat{\mathbf{u}}_{sc}(\mathbf{N}_b))\mathrm{d}\Sigma \underline{\hat{\mathbf{u}}}_b = -\underline{\hat{\mathbf{v}}}^{\mathrm{T}} \int_{\Sigma} \mathbf{N}_b^{\mathrm{T}} \hat{\mathbf{t}}_g(\hat{\mathbf{u}}_0)\mathrm{d}\Sigma \quad (3.14)$$

Taking into account, that the principle of virtual work holds for any virtual displacement field $\hat{\mathbf{v}}$, the term $\underline{\hat{\mathbf{v}}}^{\mathrm{T}}$ can be omitted, resulting in

$$\left(\mathbf{K}_b - \omega^2 \mathbf{M}_b + \hat{\mathbf{K}}_g\right) \underline{\hat{\mathbf{u}}}_b = \underline{\hat{\mathbf{f}}}_b \quad (3.15)$$

where $\mathbf{K}_b$ and $\mathbf{M}_b$ are the finite element stiffness and mass matrices of the structure, respectively:

$$\mathbf{K}_b = \int_{\Omega_b} \mathbf{N}_b^{\mathrm{T}} \mathbf{L}^{\mathrm{T}} \mathbf{D} \mathbf{L} \mathbf{N}_b \mathrm{d}\Omega \quad (3.16a)$$

$$\mathbf{M}_b = \int_{\Omega_b} \mathbf{N}_b^{\mathrm{T}} \rho_b \mathbf{N}_b \mathrm{d}\Omega \quad (3.16b)$$

These matrices are computed by means of a finite element method [ZT88]. The matrix

$$\hat{\mathbf{K}}_g = \int_{\Sigma} \mathbf{N}_b^{\mathrm{T}} \hat{\mathbf{t}}_g(\hat{\mathbf{u}}_{sc}(\mathbf{N}_b))\mathrm{d}\Sigma \quad (3.17)$$

stands for the stiffness of the soil, and the vector

$$\underline{\hat{\mathbf{f}}}_b = \int_{\Sigma} \mathbf{N}_b^{\mathrm{T}} \hat{\mathbf{t}}_g(\hat{\mathbf{u}}_0)\mathrm{d}\Sigma \quad (3.18)$$

denotes the nodal loading forces. These quantities are computed by means of a boundary element method, as will be described in chapter 4.

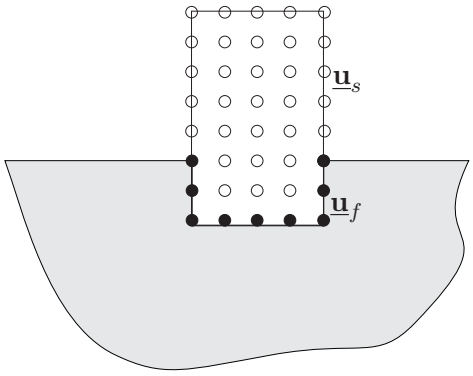

Figure 3.5: The structural displacement degrees of freedom are separated into DOF of the soil-structure interface $\mathbf{u}_f$ and DOF of the superstructure $\mathbf{u}_s$

3.4 The structural response

Building a sufficiently fine mesh of a large building can result in a FE model with a large number of degrees of freedom (DOF). In order to reduce computational costs, a number of reduction methods have been worked out which seek for the structural displacements in a subspace of all the DOF. The family of Component Mode Synthesis (CMS) [CB68], [Bal96] methods choose the subspace spanned by the first few modes of the structural components.

3.4.1 The Craig-Bampton modal decomposition method

The Craig-Bampton modal decomposition method [CB68] is a CMS method which works with the modes of two components, the superstructure and the foundation. Therefore, it is very useful for SSI problems, where (1) the same soil-foundation system with different superstructures or superstructural excitations, or (2) the same superstructure with different foundations or ground-borne excitations is investigated.

The structural displacement DOF are separated in two groups, as shown in figure 3.5:

$$\underline{\mathbf{u}}_b = \begin{Bmatrix} \underline{\mathbf{u}}_s \\ \underline{\mathbf{u}}_f \end{Bmatrix} \tag{3.19}$$

where $\underline{\mathbf{u}}_f$ stands for the displacements at the soil-structure interface (foundation), and $\underline{\mathbf{u}}_s$ denotes the remaining displacement DOF of the structure (superstructure). This separation results in the following basic equation of dynamic SSI:

$$\left(\begin{bmatrix} \mathbf{K}_{ss} & \mathbf{K}_{sf} \\ \mathbf{K}_{fs} & \mathbf{K}_{ff} + \hat{\mathbf{K}}_g \end{bmatrix} - \omega^2 \begin{bmatrix} \mathbf{M}_{ss} & \mathbf{M}_{sf} \\ \mathbf{M}_{fs} & \mathbf{M}_{ff} \end{bmatrix} \right) \begin{Bmatrix} \underline{\mathbf{u}}_s \\ \underline{\mathbf{u}}_f \end{Bmatrix} = \begin{Bmatrix} \mathbf{0} \\ \underline{\mathbf{f}}_g \end{Bmatrix} \tag{3.20}$$

The displacement of the foundation is written as a superposition of flexible foundation modes $\boldsymbol{\phi}_{fj}$ with free boundary conditions.

$$\underline{\mathbf{u}}_f = \sum_j \boldsymbol{\phi}_{fj} \alpha_{fj} = \boldsymbol{\Phi}_f \boldsymbol{\alpha}_f \tag{3.21}$$

where the modes $\boldsymbol{\phi}_{fj}$ are the solutions of the eigenvalue problem

$$\mathbf{K}'_{ff} \boldsymbol{\phi}_{fj} = \omega_{fj}^2 \mathbf{M}'_{ff} \boldsymbol{\phi}_{fj} \tag{3.22}$$

The matrices $\mathbf{K}'_{bb}$ and $\mathbf{M}'_{bb}$ differ from the lower diagonal terms of the structural mass and stiffness matrices in Equation (3.20) at the DOF of the superstructure-foundation interface, as the modes are determined in the absence of the superstructure, with free boundary conditions.

The displacement of the superstructure is written as a superposition of the quasi-static transmission of the foundation's displacement to the superstructure and the modes of the superstructure clamped at the superstructure-foundation interface:

$$\underline{\mathbf{u}}_s = \mathbf{R}_{sf}\underline{\mathbf{u}}_f + \sum_j \boldsymbol{\phi}_{sj}\alpha_{sj} = \mathbf{R}_{sf}\mathbf{u}_f + \boldsymbol{\Phi}_s\boldsymbol{\alpha}_s \tag{3.23}$$

where the matrix $\mathbf{R}_{sf}$ describes the quasi-static transmission of the base motion. This can be determined by expressing $\underline{\mathbf{u}}_s$ in terms of $\underline{\mathbf{u}}_f$ in the static form ($\omega = 0$) of equation (3.20):

$$\mathbf{R}_{sf} = -\mathbf{K}_{ss}^{-1}\mathbf{K}_{sf} \tag{3.24}$$

The modes $\boldsymbol{\phi}_{sj}$ of the superstructure clamped at the foundation can be determined by solving the eigenvalue problem:

$$\mathbf{K}_{ss}\boldsymbol{\phi}_{sj} = \omega_{sj}^2\mathbf{M}_{ss}\boldsymbol{\phi}_{sj} \tag{3.25}$$

Defining $\boldsymbol{\Phi}_f^s = \mathbf{R}_{sf}\boldsymbol{\Phi}_f$ for the quasi-static transmission of the foundation modes, the decomposition can be expressed in the form:

$$\begin{Bmatrix}\underline{\mathbf{u}}_s\\ \underline{\mathbf{u}}_f\end{Bmatrix} = \begin{bmatrix}\boldsymbol{\Phi}_s & \boldsymbol{\Phi}_f^s\\ \mathbf{0} & \boldsymbol{\Phi}_f\end{bmatrix}\begin{Bmatrix}\boldsymbol{\alpha}_s\\ \boldsymbol{\alpha}_f\end{Bmatrix} \tag{3.26}$$

Introducing (3.26) into (3.20) results in the following equation:

$$\begin{bmatrix}\boldsymbol{\Phi}_s^{\mathrm{T}} & \mathbf{0}\\ \boldsymbol{\Phi}_f^{s\,\mathrm{T}} & \boldsymbol{\Phi}_f^{\mathrm{T}}\end{bmatrix}\left(\begin{bmatrix}\mathbf{K}_{ss} & \mathbf{K}_{sf}\\ \mathbf{K}_{fs} & \mathbf{K}_{ff}+\mathbf{K}_g\end{bmatrix} - \omega^2\begin{bmatrix}\mathbf{M}_{ss} & \mathbf{M}_{sf}\\ \mathbf{M}_{fs} & \mathbf{M}_{ff}\end{bmatrix}\right)\begin{bmatrix}\boldsymbol{\Phi}_s & \boldsymbol{\Phi}_f^s\\ \mathbf{0} & \boldsymbol{\Phi}_f\end{bmatrix}\begin{Bmatrix}\boldsymbol{\alpha}_s\\ \boldsymbol{\alpha}_f\end{Bmatrix} = \begin{bmatrix}\boldsymbol{\Phi}_s^{\mathrm{T}} & \mathbf{0}\\ \boldsymbol{\Phi}_f^{s\,\mathrm{T}} & \boldsymbol{\Phi}_f^{\mathrm{T}}\end{bmatrix}\begin{Bmatrix}\mathbf{0}\\ \mathbf{f}_f\end{Bmatrix} \tag{3.27}$$

what can be simplified as

$$\left(\begin{bmatrix}\boldsymbol{\Lambda}_s & \mathbf{0}\\ \mathbf{0} & \boldsymbol{\kappa}_{ff}\end{bmatrix} - \omega^2\begin{bmatrix}\mathbf{I} & \boldsymbol{\mu}_{sf}\\ \boldsymbol{\mu}_{fs} & \boldsymbol{\mu}_{ff}\end{bmatrix}\right)\begin{Bmatrix}\boldsymbol{\alpha}_s\\ \boldsymbol{\alpha}_f\end{Bmatrix} = \begin{Bmatrix}\mathbf{0}\\ \boldsymbol{\Phi}_f^{\mathrm{T}}\mathbf{f}_f\end{Bmatrix} \tag{3.28}$$

where $\boldsymbol{\Lambda}_s = \mathrm{diag}\left\{\omega_{sj}^2\right\}$ contains the squares of the eigenfrequencies of the superstructure, $\mathbf{I}$ is a unit matrix and

$$\boldsymbol{\kappa}_{ff} = \boldsymbol{\Phi}_f^{\mathrm{T}}(\mathbf{K}_{ff}+\hat{\mathbf{K}}_g)\boldsymbol{\Phi}_f + \boldsymbol{\Phi}_f^{\mathrm{T}}\mathbf{K}_{fs}\boldsymbol{\Phi}_f^s \tag{3.29a}$$

$$\boldsymbol{\mu}_{sf} = \boldsymbol{\mu}_{fs}^{\mathrm{T}} = \boldsymbol{\Phi}_s^{\mathrm{T}}\mathbf{M}_{ss}\boldsymbol{\Phi}_f^s + \boldsymbol{\Phi}_s^{\mathrm{T}}\mathbf{M}_{sf}\boldsymbol{\Phi}_f \tag{3.29b}$$

$$\boldsymbol{\mu}_{ff} = \boldsymbol{\Phi}_f^{s\,\mathrm{T}}\mathbf{M}_{ss}\boldsymbol{\Phi}_f^s + \boldsymbol{\Phi}_f^{\mathrm{T}}\mathbf{M}_{fs}\boldsymbol{\Phi}_f^s + \boldsymbol{\Phi}_f^{s\,\mathrm{T}}\mathbf{M}_{sf}\boldsymbol{\Phi}_f + \boldsymbol{\Phi}_f^{\mathrm{T}}\mathbf{M}_{ff}\boldsymbol{\Phi}_f \tag{3.29c}$$

The solution of (3.28) results in the modal coordinates $\boldsymbol{\alpha}_s$ and $\boldsymbol{\alpha}_f$, which can be substituted into (3.26) to get the structural response.

3.4.2 Simplifications of the formulation

The presented formulation can be significantly simplified, if it is assumed that dynamic SSI does not play an important role in the ground borne structural vibrations and re-radiated noise. This assumption is very attractive from a computational point of view, because the determination of the soil's impedance with a 3D boundary element method can be avoided. Some assumptions have to be made, however, regarding the impedance difference between the soil and the foundation.

Response of a structure with flexible foundation on rigid soil

If the soil is much stiffer than the structure, then it can be assumed that the incident wave field is not affected by the structure, and the structure's foundation can be directly excited with the incident soil displacements. In this case, the displacements of the foundation will be similar to the incoming wave field: $\underline{\mathbf{u}}_f \approx \underline{\mathbf{u}}_{\text{inc}}$. When applying the Craig-Bampton decomposition technique, $\underline{\mathbf{u}}_f$ is written as a superposition of foundation modes. The $\boldsymbol{\alpha}_f$ modal coordinates can be determined by projecting the incident wave field on the $\boldsymbol{\Phi}_f$ flexible foundation modes:

$$\boldsymbol{\Phi}_f^{\mathrm{T}} \underline{\mathbf{u}}_{\text{inc}} \approx \boldsymbol{\Phi}_f^{\mathrm{T}} \underline{\mathbf{u}}_f = \boldsymbol{\Phi}_f^{\mathrm{T}} \boldsymbol{\Phi}_f \boldsymbol{\alpha}_f \tag{3.30}$$

This means that the modal coordinates of the foundation modes can be obtained as:

$$\boldsymbol{\alpha}_f = \left[\boldsymbol{\Phi}_f^{\mathrm{T}} \boldsymbol{\Phi}_f \right]^{-1} \boldsymbol{\Phi}_f^{\mathrm{T}} \underline{\mathbf{u}}_{\text{inc}} \tag{3.31}$$

After having determined $\boldsymbol{\alpha}_f$, the modal coordinates of the superstructure modes can be determined from the first equation of (3.28) as

$$\left(\boldsymbol{\Lambda}_s - \omega^2 \mathbf{I} \right) \boldsymbol{\alpha}_s = \omega^2 \left(\boldsymbol{\Phi}_s^{\mathrm{T}} \mathbf{M}_{ss} \boldsymbol{\Phi}_f^s + \boldsymbol{\Phi}_s^{\mathrm{T}} \mathbf{M}_{sf} \boldsymbol{\Phi}_f \right) \boldsymbol{\alpha}_f \tag{3.32}$$

Considering that the left-hand side of equation (3.34) is diagonal, the structural response can be computed in a very efficient way.

Response of a structure with rigid foundation to displacement excitation

If the incident wave field is uniform at the building's foundation, then it can be assumed that only rigid body modes of the foundation are excited by the incident wave field. The uniform wave motion can be the result of a low frequency vibration source mechanism or the vertical incidence of P-waves. In this case, the superstructure is supported by a totally rigid foundation. The (in general six) rigid body modes of the foundation are collected in the matrix $\mathbf{R}_{f0}$, their modal coordinates are collected in the displacement vector $\mathbf{u}_0$. The quasi-static transmission of the rigid body base motion is a rigid body motion of the superstructure, the corresponding nodal displacements are collected in the matrix $\mathbf{R}_{s0} = \mathbf{R}_{sf} \mathbf{R}_{f0}$:

$$\begin{Bmatrix} \underline{\mathbf{u}}_s \\ \underline{\mathbf{u}}_f \end{Bmatrix} = \begin{bmatrix} \boldsymbol{\Phi}_s & \mathbf{R}_{s0} \\ \mathbf{0} & \mathbf{R}_{f0} \end{bmatrix} \begin{Bmatrix} \boldsymbol{\alpha}_s \\ \mathbf{u}_0 \end{Bmatrix} \tag{3.33}$$

Applying these notations, the first equation of (3.28) can be written as

$$\left(\boldsymbol{\Lambda}_s - \omega^2 \mathbf{I} \right) \boldsymbol{\alpha}_s = \omega^2 \boldsymbol{\Phi}_s^{\mathrm{T}} \mathbf{M}_{s0} \mathbf{u}_0 \tag{3.34}$$

where

$$\mathbf{M}_{s0} = \mathbf{M}_{ss}\mathbf{R}_{s0} + \mathbf{M}_{sf}\mathbf{R}_{f0} \tag{3.35}$$

Here, the left hand side of equation (3.32) is diagonal, just like for the case of the rigid foundation.

Chapter 4

The mitigation of fictitious eigenfrequencies of the boundary element method in elastodynamics

4.1 Introduction

As it was mentioned in equation (3.17) of section (3.18), the soil's dynamic stiffness $\hat{\mathbf{K}}_g$ and the loading term $\hat{\underline{\mathbf{f}}}_b$ due to the incident wave field $\mathbf{u}_{\text{inc}}$ can be computed by means of a boundary element method. This section aims to briefly introduce the BEM for elastodynamics, and to deal with the problem of fictitious eigenfrequencies.

The problem of fictitious eigenfrequencies is related to the boundary element method used for exterior problems. Exterior problems are the computation of radiated wave fields to exterior unbounded domains by vibrating surfaces; the computation of scattered wave fields from rigid or elastic surfaces; or the determination of the impedance of cavities or foundations embedded into an infinite elastic domain. As the frequency domain boundary element method is applied to these exterior problems, undesired computational errors can occur. These errors appear close to the eigenfrequencies of the interior domain, i.e. the cavity or soil excavation filled with the external material.

When dynamic soil-structure interaction problems are considered in the higher frequency range, where the modal density of the embedded foundations is large, the effect of these fictitious eigenfrequencies becomes very important [Pyl04]. Therefore, different upgraded solution techniques mitigating the effect of the fictitious eigenfrequencies need to be developed.

As the first applications of the boundary element method for the computation of dynamic problems are related to applications in acoustics [SF62] or electromagnetics, the problem of fictitious eigenfrequencies was also first discovered in this fields of engineering. In the following section of this chapter, the boundary element method for elastodynamics is introduced, and the problem of fictitious eigenfrequencies is demonstrated. The demonstration method is based on the work of Schenck [Sch68] that was originally performed in the field of acoustic scattering problems.

4.2 The non-uniqueness problem of the exterior boundary integral equation

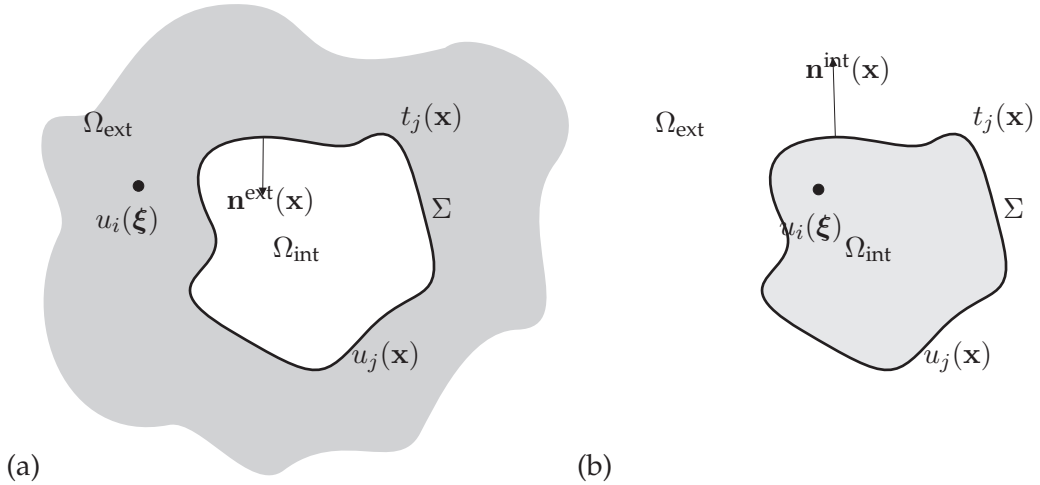

Figure 4.1: Definition of exterior and interior domains

The representation theorem of elastodynamics relates the displacement field $u_i(\boldsymbol{\xi}, \omega)$ in a closed domain Ω_{int} or in an infinite unbounded exterior domain Ω_{ext} to displacements $u_j(\mathbf{x}, \omega)$ and tractions $t_j(\mathbf{x}, \omega)$ on the domain's boundary Σ.

For the case of exterior problems, where the external wave field radiated by or scattered from the boundary Σ to the infinite external domain Ω_{ext} is searched, the representation theorem can be written in the form

$$c(\boldsymbol{\xi})u_i(\boldsymbol{\xi}, \omega) = \int_\Sigma t_j^{\text{ext}}(\mathbf{u})(\mathbf{x}, \omega)u_{ij}^G(\boldsymbol{\xi}, \mathbf{x}, \omega)\mathrm{d}\Sigma - \int_\Sigma t_{ij}^{\text{ext}G}(\boldsymbol{\xi}, \mathbf{x}, \omega)u_j(\mathbf{x}, \omega)\mathrm{d}\Sigma \tag{4.1}$$

where $\mathbf{x}$ denotes points on the boundary, $\boldsymbol{\xi}$ stands for an arbitrary point in the full space, $u_{ij}^G(\boldsymbol{\xi}, \mathbf{x}, \omega)$ and $t_{ij}^G(\boldsymbol{\xi}, \mathbf{x}, \omega)$ denote the Green's displacement and traction tensors, and

$$c(\boldsymbol{\xi}) = \begin{cases} 1 & \text{if } \boldsymbol{\xi} \in \Omega_{\text{ext}} \\ 0.5 & \text{if } \boldsymbol{\xi} \in \Sigma \\ 0 & \text{if } \boldsymbol{\xi} \in \Omega_{\text{int}} \end{cases} \tag{4.2}$$

In equation (4.1) the surface tractions are related to the external unit normal vector $\mathbf{n}^{\text{ext}}(\mathbf{x})$ on the boundary Σ, as shown in figure 4.1a. This external normal vector points out from the external domain.

For the case of interior problems, where the displacement field radiated into the bounded internal domain Ω_{int} is of interest, the representation theorem can be written as

$$c(\boldsymbol{\xi})u_i(\boldsymbol{\xi}, \omega) = \int_\Sigma t_j^{\text{int}}(\mathbf{u})(\mathbf{x}, \omega)u_{ij}^G(\boldsymbol{\xi}, \mathbf{x}, \omega)\mathrm{d}\Sigma - \int_\Sigma t_{ij}^{\text{int}G}(\boldsymbol{\xi}, \mathbf{x}, \omega)u_j(\mathbf{x}, \omega)\mathrm{d}\Sigma \tag{4.3}$$

where

$$c(\boldsymbol{\xi}) = \begin{cases} 1 & \text{if } \boldsymbol{\xi} \in \Omega_{\text{int}} \\ 0.5 & \text{if } \boldsymbol{\xi} \in \Sigma \\ 0 & \text{if } \boldsymbol{\xi} \in \Omega_{\text{ext}} \end{cases} \tag{4.4}$$

and the tractions are defined using the internal unit normal $\mathbf{n}^{\text{int}}(\mathbf{x})$. Taking into account that $\mathbf{n}^{\text{int}}(\mathbf{x}) = -\mathbf{n}^{\text{ext}}(\mathbf{x})$, equation (4.3) can be rewritten in the form:

$$c(\boldsymbol{\xi})u_i(\boldsymbol{\xi},\omega) = -\int_\Sigma t_j^{\text{ext}}(\mathbf{u})(\mathbf{x},\omega)u_{ij}^G(\boldsymbol{\xi},\mathbf{x},\omega)\mathrm{d}\Sigma + \int_\Sigma t_{ij}^{\text{ext}G}(\boldsymbol{\xi},\mathbf{x},\omega)u_j(\mathbf{x},\omega)\mathrm{d}\Sigma \tag{4.5}$$

In the following, for the sake of brevity, the $()^{\text{ext}}$ and $()^{\text{int}}$ indices will be omitted, and the tractions will be always used as defined by the external normal $\mathbf{n}^{\text{ext}}$.

The surface tractions and displacements are not independent, a defined displacement or traction field on the boundary determines the other unknown quantity. In a Neumann problem the known quantities are the surface tractions, in a Dirichlet problem the surface displacements are prescribed.

The determination of the radiated wave field is generally carried out by means of a boundary element method. The surface is discretized into boundary elements. The displacements and tractions are approximated on the surface using their nodal values u_{nj} and t_{nj}, and shape functions $N_n(\mathbf{x})$. Writing independent equations for well chosen nodal points $\boldsymbol{\xi} \in \Sigma$ on the boundary, a system of linear equations is obtained:

$$\mathbf{Hu} = \mathbf{Gt} \tag{4.6}$$

where $\mathbf{u}$ and $\mathbf{t}$ contain the nodal displacements and tractions, respectively, and the matrices $\mathbf{H}$ and $\mathbf{G}$ are derived from the Green's tractions and displacements. For the case of the exterior equation, these matrices are given by:

$$G_{mn} = \int_\Sigma N_n(\mathbf{x})u_{ij}^G(\boldsymbol{\xi}_m,\mathbf{x},\omega)\mathrm{d}\Sigma \tag{4.7a}$$

$$H_{mn} = \frac{\delta_{mn}}{2} + \int_\Sigma N_n(\mathbf{x})t_{ij}^G(\boldsymbol{\xi}_m,\mathbf{x},\omega)\mathrm{d}\Sigma \tag{4.7b}$$

For the case of the interior equation, the matrices are defined as:

$$G_{mn} = \int_\Sigma N_n(\mathbf{x})u_{ij}^G(\boldsymbol{\xi}_m,\mathbf{x},\omega)\mathrm{d}\Sigma \tag{4.8a}$$

$$H_{mn} = \frac{\delta_{mn}}{2} - \int_\Sigma N_n(\mathbf{x})t_{ij}^G(\boldsymbol{\xi}_m,\mathbf{x},\omega)\mathrm{d}\Sigma \tag{4.8b}$$

In the following, it will be shown that the exterior integral equation (4.1) corresponding to a Neumann problem has a non-unique solution at the eigenfrequencies of the corresponding interior Dirichlet problem.

First, we are searching for the internal displacements $u_{1i}(\boldsymbol{\xi},\omega)$ of the closed domain Ω_{int} and the corresponding surface tractions $t_{1j}(\mathbf{x},\omega) = t_j(\mathbf{u}_1)(\mathbf{x},\omega)$ on Σ, with zero displacement boundary conditions on the interface Σ, as shown in figure 4.2. Therefore, we write the interior surface integral equation for $\boldsymbol{\xi} \in \Sigma$ as:

$$\frac{1}{2}u_{1i}(\boldsymbol{\xi},\omega) = -\int_\Sigma t_j(\mathbf{u}_1)(\mathbf{x},\omega)u_{ij}^G(\boldsymbol{\xi},\mathbf{x},\omega)\mathrm{d}\Sigma + \int_\Sigma t_{ij}^G(\boldsymbol{\xi},\mathbf{x},\omega)u_{1j}(\mathbf{x},\omega)\mathrm{d}\Sigma \tag{4.9}$$

Making use of the zero displacement boundary condition on the boundary Σ, the left hand side and the second term on the right hand side vanishes:

$$0 = \int_\Sigma t_j(\mathbf{u}_1)(\mathbf{x},\omega)u_{ij}^G(\boldsymbol{\xi},\mathbf{x},\omega)\mathrm{d}\Sigma \quad \boldsymbol{\xi} \in \Sigma \tag{4.10}$$

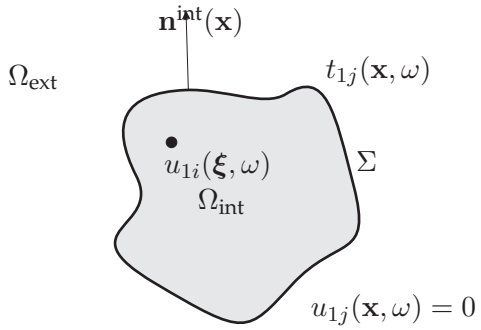

Figure 4.2: Problem 1.

or, in discretized form:

$$\mathbf{0} = \mathbf{G}\mathbf{t}_1 \tag{4.11}$$

The resulting eigenvalue problem has nontrivial surface traction solution $t_{1jk}(\mathbf{x})$ at the eigenfrequencies $\bar{\omega}_k$ of the internal domain. These tractions can be substituted into equation (4.5) in order to find the corresponding displacement field at any $\boldsymbol{\xi} \in \Omega_{\text{int}}$.

$$u_{1ik}(\boldsymbol{\xi}) = -\int_\Sigma t_{1jk}(\mathbf{x}) u_{ij}^G(\boldsymbol{\xi},\mathbf{x},\bar{\omega}_k)\mathrm{d}\Sigma \quad \boldsymbol{\xi} \in \Omega_{\text{int}} \tag{4.12}$$

For later use we write the interior integral equation (4.5) with the zero displacement boundary conditions for $\boldsymbol{\xi} \in \Omega_{\text{ext}}$:

$$0 = -\int_\Sigma t_{1j}(\mathbf{u}_1)(\mathbf{x},\omega) u_{ij}^G(\boldsymbol{\xi},\mathbf{x},\omega)\mathrm{d}\Sigma \quad \boldsymbol{\xi} \in \Omega_{\text{ext}} \tag{4.13}$$

In a second problem, we solve an external problem by imposing the modal tractions $t_{1jk}(\mathbf{x})$ on the surface Σ at the eigenfrequency $\bar{\omega}_k$. We are searching for the resulting surface displacements $u_{2j}(\mathbf{x},\bar{\omega}_k)$ and externally radiated displacement field $u_{2i}(\boldsymbol{\xi},\bar{\omega}_k)$. Writing the exterior surface integral (4.1) with $\boldsymbol{\xi} \in \Sigma$:

$$\frac{1}{2}u_{2i}(\boldsymbol{\xi},\bar{\omega}_k) = \int_\Sigma t_{1jk}(\mathbf{x}) u_{ij}^G(\boldsymbol{\xi},\mathbf{x},\bar{\omega}_k)\mathrm{d}\Sigma - \int_\Sigma t_{ij}^G(\boldsymbol{\xi},\mathbf{x},\bar{\omega}_k) u_{2j}(\mathbf{x},\bar{\omega}_k)\mathrm{d}\Sigma \tag{4.14}$$

Due to (4.10), the first term of the right hand side vanishes, and the surface displacements can be determined by solving the integral equation

$$\frac{1}{2}u_{2i}(\boldsymbol{\xi},\bar{\omega}_k) = -\int_\Sigma t_{ij}^G(\boldsymbol{\xi},\mathbf{x},\bar{\omega}_k) u_{2j}(\mathbf{x},\bar{\omega}_k)\mathrm{d}\Sigma \quad \boldsymbol{\xi} \in \Sigma \tag{4.15}$$

The radiated displacement field can then be determined by evaluating the exterior surface integral (4.1) with $\boldsymbol{\xi} \in \Omega_{\text{ext}}$:

$$u_{2i}(\boldsymbol{\xi},\bar{\omega}_k) = \int_\Sigma t_{1jk}(\mathbf{x}) u_{ij}^G(\boldsymbol{\xi},\mathbf{x},\bar{\omega}_k)\mathrm{d}\Sigma - \int_\Sigma t_{ij}^G(\boldsymbol{\xi},\mathbf{x},\bar{\omega}_k) u_{2j}(\mathbf{x},\bar{\omega}_k)\mathrm{d}\Sigma \tag{4.16}$$

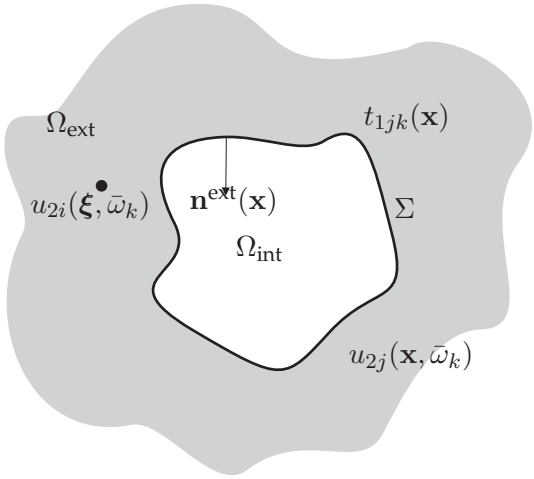

Figure 4.3: Problem 2.

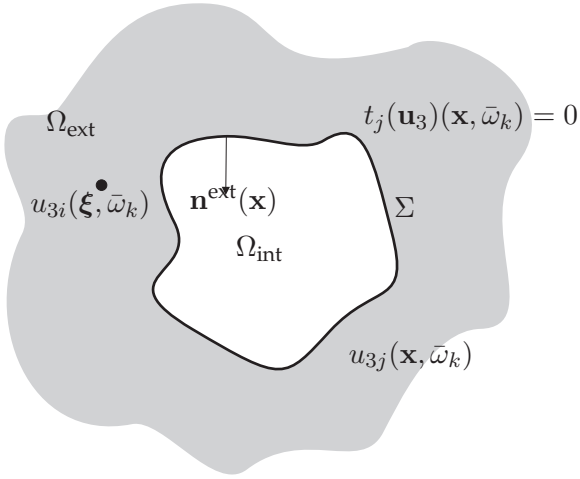

Figure 4.4: Problem 3.

Due to (4.13), this integral simplifies to

$$u_{2i}(\boldsymbol{\xi}, \bar{\omega}_k) = -\int_{\Sigma} t_{ij}^{G}(\boldsymbol{\xi}, \mathbf{x}, \bar{\omega}_k) u_{2j}(\mathbf{x}, \bar{\omega}_k) \mathrm{d}\Sigma \quad \boldsymbol{\xi} \in \Omega_{\text{ext}} \tag{4.17}$$

With physical considerations we can state that the $u_{2i}(\boldsymbol{\xi}, \bar{\omega}_k)$ displacement field is non zero, as it is radiated by non zero tractions into an infinite domain. From (4.15) it follows then that the surface displacements $u_{2j}(\mathbf{x}, \bar{\omega}_k)$ also differ from zero.

For later use, we write the external integral equation (4.1) with the modal traction constraint for the case $\boldsymbol{\xi} \in \Omega_{\text{int}}$

$$0 = \int_{\Sigma} t_{1jk}(\mathbf{x}) u_{ij}^{G}(\boldsymbol{\xi}, \mathbf{x}, \bar{\omega}_k) \mathrm{d}\Sigma - \int_{\Sigma} t_{ij}^{G}(\boldsymbol{\xi}, \mathbf{x}, \bar{\omega}_k) u_{2j}(\mathbf{x}, \bar{\omega}_k) \mathrm{d}\Sigma \quad \boldsymbol{\xi} \in \Omega_{\text{int}} \tag{4.18}$$

Finally, we are searching for the solution $\mathbf{u}_3$ of the exterior boundary integral equation (4.1) by applying zero stresses on the surface Σ at the eigenfrequency $\bar{\omega}_k$. Writing the exterior

equation for $\boldsymbol{\xi} \in \Sigma$:

$$\frac{1}{2}u_{3i}(\boldsymbol{\xi},\bar{\omega}_k) = \int_\Sigma t_j(\mathbf{u}_3)(\mathbf{x},\bar{\omega}_k)u_{ij}^G(\boldsymbol{\xi},\mathbf{x},\bar{\omega}_k)\mathrm{d}\Sigma - \int_\Sigma t_{ij}^G(\boldsymbol{\xi},\mathbf{x},\bar{\omega}_k)u_{3j}(\mathbf{x},\bar{\omega}_k)\mathrm{d}\Sigma \tag{4.19}$$

substituting $t_j(\mathbf{u}_3)(\mathbf{x},\bar{\omega}_k) = 0$, the integral equation simplifies to

$$\frac{1}{2}u_{3i}(\boldsymbol{\xi},\bar{\omega}_k) = -\int_\Sigma t_{ij}^G(\boldsymbol{\xi},\mathbf{x},\bar{\omega}_k)u_{3j}(\mathbf{x},\bar{\omega}_k)\mathrm{d}\Sigma \quad \boldsymbol{\xi} \in \Sigma \tag{4.20}$$

As (4.15) and (4.20) are identical, the $u_{3j}(\mathbf{x},\bar{\omega}_k) = u_{2j}(\mathbf{x},\bar{\omega}_k)$ non zero solution satisfies (4.20).

So it has been found that the exterior surface integral equation with zero surface traction boundary conditions has a non-zero displacement solution $u_{3i}(\boldsymbol{\xi},\bar{\omega}_k)$ at the eigenfrequencies of the internal domain with zero displacement boundary conditions. Therefore, for any traction boundary condition and at the eigenfrequency $\bar{\omega}_k$, the solution of the exterior radiation problem is non unique, and can be written as $u_i(\boldsymbol{\xi},\bar{\omega}_k) + Au_{3i}(\boldsymbol{\xi},\bar{\omega}_k)$, where A is an arbitrary constant.

4.3 Mitigation of the fictitious eigenfrequencies

In order to overcome the problem of fictitious eigenfrequencies in the BEM, several efficient solution methods have been proposed. The first improved integral formulation was proposed by Brundrit [Bru65] in acoustics. Brundrit proposed to use an indirect integral formulation with layer potentials, and proved that this formulation does not suffer from the aforementioned problem.

One of the most fruitful improved integral methods are based on an integral equation that is a combination of the original surface integral and its normal derivative with respect to the surface normal vector. The first approach in this field was made by Panich [Pan65]. This method, in its original form was computationally very expensive, but it has been further developed by Kussmaul [Kus69], Burton and Miller [BM71], and later by Zaman [Zam94] in order to obtain an easily applicable integral equation with unique solution for all wave numbers.

An other family of the improved integral equations is assembled by simultaneously writing the interior and exterior surface integrals or by utilizing the integral equation in points of the interior region. The first approach in this field was made by Kupradze [Kup65] and Copley [Cop67], and their method has been further developed by Schenck [Sch68] to gain the CHIEF method that is still very popular and wich is widely implemented in acoustic softwares.

A third family of improved integral formulations was founded by Ursell and Jones [Urs73], [Urs78]. They gained a unique solution by applying a modified Green's function that is built up as the sum of the original Green's function and a wave function analytic in the exterior domain and on the boundary. For this wave function, Ursell proposed an infinite sum of spherical harmonics, and Jones improved the formulation to a finite series of Hankel functions.

In the following, the adoptation of Schenk's CHIEF method to elastodynamics will be considered. It will be shown how the CHIEF method can mitigate the effect of fictitious

eigenfrequencies in elastodynamics. Later, Schenk's method will be compared to the modified Burton and Miller method [PCD04]. It will be shown in a numerical example that the adoptation of Schenk's method can be more efficient than the modified Burton and Miller method.

4.3.1 The CHIEF method

In the following it will be shown that the solution $u_{3j}(\mathbf{x}, \bar{\omega}_k)$ does not necessarily satisfy the integral equation for $\boldsymbol{\xi} \in \Omega_{\text{int}}$. Writing the exterior equation (4.1) for interior $\boldsymbol{\xi}$ points, we gain

$$0 = \int_\Sigma t_j(\mathbf{u}_3)(\mathbf{x}, \bar{\omega}_k) u_{ij}^G(\boldsymbol{\xi}, \mathbf{x}, \omega) \mathrm{d}\Sigma - \int_\Sigma t_{ij}^G(\boldsymbol{\xi}, \mathbf{x}, \omega) u_{3j}(\mathbf{x}, \bar{\omega}_k) \mathrm{d}\Sigma \quad \boldsymbol{\xi} \in \Omega_{\text{int}} \tag{4.21}$$

As $\mathbf{u}_3$ corresponds to zero tractions on Σ, $t_j(\mathbf{u}_3) = 0$, and the first integral vanishes:

$$0 = -\int_\Sigma t_{ij}^G(\boldsymbol{\xi}, \mathbf{x}, \omega) u_{3j}(\mathbf{x}, \bar{\omega}_k) \mathrm{d}\Sigma \quad \boldsymbol{\xi} \in \Omega_{\text{int}} \tag{4.22}$$

On the surface Σ, $u_{3j}(\mathbf{x}, \bar{\omega}_k) = u_{2j}(\mathbf{x}, \bar{\omega}_k)$, so

$$0 = -\int_\Sigma t_{ij}^G(\boldsymbol{\xi}, \mathbf{x}, \omega) u_{2j}(\mathbf{x}, \bar{\omega}_k) \mathrm{d}\Sigma \quad \boldsymbol{\xi} \in \Omega_{\text{int}} \tag{4.23}$$

which, after making use of (4.18) and (4.12), can be written as

$$0 = -\int_\Sigma t_{1jk}(\mathbf{x}) u_{ij}^G(\boldsymbol{\xi}, \mathbf{x}, \bar{\omega}_k) \mathrm{d}\Sigma = u_{1ik}(\boldsymbol{\xi}) \quad \boldsymbol{\xi} \in \Omega_{\text{int}} \tag{4.24}$$

Thus, $u_{3j}(\mathbf{x}, \bar{\omega}_k)$ satisfies the internal integral equation only for those source points $\boldsymbol{\xi} \in \Omega_{\text{int}}$ where $u_{1ik}(\boldsymbol{\xi}) = 0$. In other words, if we demand that the solution of the external problem should satisfy the integral equation for $\boldsymbol{\xi} \in \Omega_{\text{int}}$, where $\boldsymbol{\xi}$ is not located on a zero value of the internal displacement mode $u_{1ik}(\boldsymbol{\xi})$, then the $u_{3j}(\mathbf{x}, \bar{\omega}_k)$ term will be excluded from the solution set, and the uniqueness of the solution is ensured.

The CHIEF method (the acronym is from Combined Helmholtz Integral Equation Formulation) is a combined integral equation method. It searches for the radiated exterior displacement field by discretizing the exterior surface integral for $\boldsymbol{\xi} \in \Sigma$, as well as for $\boldsymbol{\xi} \in \Omega_{\text{int}}$. The discretized surface integral written for N_s nodal $\boldsymbol{\xi}$ points of the surface Σ, results in matrices $\mathbf{H}_s$ and $\mathbf{G}_s$. A further number of N_i discretized equations are written by locating $\boldsymbol{\xi}$ in N_i chosen internal points, resulting in the matrices $\mathbf{H}_i$ and $\mathbf{G}_i$. The combined discretized integral equation then takes the form

$$\begin{bmatrix} \mathbf{H}_s \\ \mathbf{H}_i \end{bmatrix} \{\mathbf{u}\} = \begin{bmatrix} \mathbf{G}_s \\ \mathbf{G}_i \end{bmatrix} \{\mathbf{t}\} \tag{4.25}$$

This system of equations consists of $N_s + N_i$ equations for N_s unknowns, and is therefore solved by means of a least mean squares method.

4.3.2 The modified Burton and Miller method

An other solution technique, first proposed by Burton and Miller [BM71] for the acoustic exterior problem is to use a combined external boundary integral equation. The combined integral equation is a linear combination of the exterior surface integral equation:

$$\frac{u_i(\boldsymbol{\xi},\omega)}{2} = \int_\Sigma t_j(\mathbf{u})(\mathbf{x},\omega) u_{ij}^G(\boldsymbol{\xi},\mathbf{x},\omega)\mathrm{d}\Sigma - \int_\Sigma t_{ij}^G(\boldsymbol{\xi},\mathbf{x},\omega) u_j(\mathbf{x},\omega)\mathrm{d}\Sigma \tag{4.26}$$

and its derivative with respect to the variable $\boldsymbol{\xi}$ in the surface normal direction ξ_n:

$$\frac{\partial u_i(\boldsymbol{\xi},\omega)}{2\partial\xi_n} = \int_\Sigma t_j(\mathbf{u})(\mathbf{x},\omega) \frac{\partial u_{ij}^G(\boldsymbol{\xi},\mathbf{x},\omega)}{\partial\xi_n}\mathrm{d}\Sigma - \int_\Sigma \frac{\partial t_{ij}^G(\boldsymbol{\xi},\mathbf{x},\omega)}{\partial\xi_n} u_j(\mathbf{x},\omega)\mathrm{d}\Sigma \tag{4.27}$$

The linear combination of the two equations can be written as

$$\begin{aligned} & \frac{1}{2}\left(u_i(\boldsymbol{\xi},\omega) + \alpha\frac{\partial u_i(\boldsymbol{\xi},\omega)}{\partial\xi_n}\right) \\ = & \int_\Sigma t_j(\mathbf{u})(\mathbf{x},\omega)\left(u_{ij}^G(\boldsymbol{\xi},\mathbf{x},\omega) + \alpha\frac{\partial u_{ij}^G(\boldsymbol{\xi},\mathbf{x},\omega)}{\partial\xi_n}\right)\mathrm{d}\Sigma \\ - & \int_\Sigma \left(t_{ij}^G(\boldsymbol{\xi},\mathbf{x},\omega) + \alpha\frac{\partial t_{ij}^G(\boldsymbol{\xi},\mathbf{x},\omega)}{\partial\xi_n}\right) u_j(\mathbf{x},\omega)\mathrm{d}\Sigma \end{aligned} \tag{4.28}$$

where α is the coupling parameter. The fictitious eigenfrequencies of equation (4.26) are those of the interior domain clamped at the interface Σ, while the critical frequencies of equation (4.27) are the eigenfrequencies of the internal domain with free boundary conditions. As these eigenfrequencies never coincide, the linear combination (4.28) yields a unique solution for all wavenumbers.

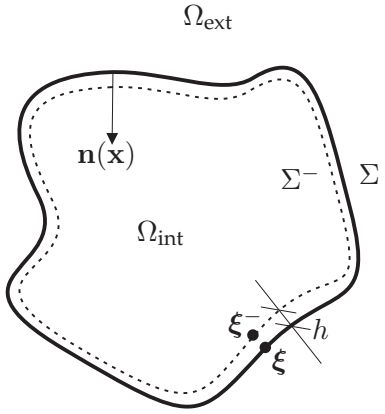

Figure 4.5: Location of the internal surface Σ^- for the Burton-Miller method

In the implementation method proposed by Clouteau, the normal derivatives are ap-

proximated numerically by means of finite difference schemes:

$$\frac{\partial u_i(\boldsymbol{\xi},\omega)}{\partial \xi_n} \approx \frac{u_i(\boldsymbol{\xi},\omega) - u_i(\boldsymbol{\xi}^-,\omega)}{h} \tag{4.29a}$$

$$\frac{\partial u_{ij}^G(\boldsymbol{\xi},\mathbf{x},\omega)}{\partial \xi_n} \approx \frac{u_{ij}^G(\boldsymbol{\xi},\mathbf{x},\omega) - u_{ij}^G(\boldsymbol{\xi}^-,\mathbf{x},\omega)}{h} \tag{4.29b}$$

$$\frac{\partial t_{ij}^G(\boldsymbol{\xi},\mathbf{x},\omega)}{\partial \xi_n} \approx \frac{t_{ij}^G(\boldsymbol{\xi},\mathbf{x},\omega) - t_{ij}^G(\boldsymbol{\xi}^-,\mathbf{x},\omega)}{h} \tag{4.29c}$$

where the points $\boldsymbol{\xi}^- = \boldsymbol{\xi} + h\mathbf{n}^{\text{ext}}$ are located on the surface Σ^- that is in the internal domain Ω_{int}, at a distance h from the original surface Σ (figure 4.5).

The discretization of equation 4.28 with the finite difference approximations results in a system of equations written in the form:

$$\left(\mathbf{H} + \frac{\alpha}{h+\alpha}\mathbf{H}^-\right)\mathbf{u} = \left(\mathbf{G} + \frac{\alpha}{h+\alpha}\mathbf{G}^-\right)\mathbf{t} \tag{4.30}$$

where the $\mathbf{H}$ and $\mathbf{G}$ matrices contain the Green's functions with the source points $\boldsymbol{\xi}$ located on the boundary surface Σ, while the $\mathbf{H}^-$ and $\mathbf{G}^-$ matrices contain the Green's functions with the source points $\boldsymbol{\xi}^-$ located on the internal surface Σ^-.

This scheme makes the Burton and Miller method easily implementable in any BE code. The choice of the method's free parameters, i.e. the coupling parameter and the distance between surface and internal points have been investigated by several authors. Amini [Ami90] proposed in acoustic applications that the coupling parameter should be inversely proportional to the wavenumber. Pyl [PCD04] investigated the coupling parameter in elastodynamics, for the case of embedded circular foundations in a homogeneous half-space. The results shows that if the distance h is chosen equal to the element length and a frequency independent imaginary coupling parameter is used, the modified Burton and Miller method can be efficiently used for mitigating the fictitious eigenfrequencies.

4.4 Numerical examples

In the following, numerical examples will be considered to compare the two methods. The impedance functions of two-dimensional cavities embedded in a full space will be computed by means of the boundary element method based on the Green's functions of the two-dimensional elastic full space.

The elastic full space is characterized by the shear wave velocity: $c_S = 200$ m/s, compressional wave velocity $c_P = 400$ m/s and mass density: $\rho = 2000$ kg/m^3. Three different material damping ratios are investigated: $\beta_1 = 0$, $\beta_2 = 0.01$, $\beta_3 = 0.02$.

A two-dimensional boundary element code with constant shape functions is used to compute the matrices $\mathbf{G}(\omega)$ and $\mathbf{H}(\omega)$, which are used to compute the impedance functions of the cavities. In order to obtain the impedance matrix that relates nodal displacements to nodal forces, a diagonal matrix $\mathbf{D}$ is introduced, the elements of which contain the width of the boundary elements. The dynamic impedance matrix $\mathbf{S}$ of the cavity can then be computed as

$$\mathbf{S}(\omega) = \mathbf{D}\mathbf{G}^{-1}(\omega)\mathbf{H}(\omega) \tag{4.31}$$

In the numerical examples modal impedance functions $\mathbf{S}_\Phi(\omega)$ will be investigated, which are obtained by projecting the impedance $\mathbf{S}(\omega)$ to displacement modes $\mathbf{\Phi}$ of the cavities:

$$\mathbf{S}_\Phi(\omega) = \mathbf{\Phi}^{\mathrm{T}}\mathbf{S}(\omega)\mathbf{\Phi} \tag{4.32}$$

.

4.4.1 Circular cavity

A circular cavity of radius $R = 3$ m is first investigated over the frequency domain $f \in [0 \text{ Hz}; 200 \text{ Hz}]$. A dimensionless frequency a_0 is defined by the relation $a_0 = 2\pi f R/c$, where $c = 200$ m/s. The range of the dimensionless frequency is approximately $a_0 \in [0; 20]$.

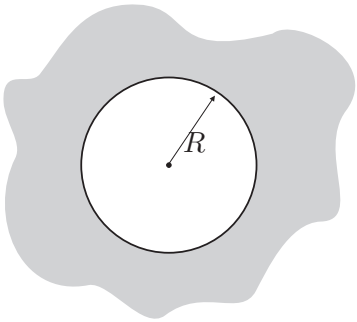

Figure 4.6: Circular cavity with radius R in a two-dimensional homogeneous domain

The dynamic modes of the internal domain

The fictitious eigenfrequencies of the exterior BE method are the eigenfrequencies of the complementary, interior domain with zero displacement boundary conditions. In order to find these modes, a FE model of the internal domain has been constructed. It consists of 1241 nodes and 1200 quadrilateral plate elements.

Table 4.1: Dimensionless eigenfrequencies a_{0i} of the circular excavation with zero displacement boundary condition along the cavity wall

3.36	3.84	5.22	5.39	6.63	6.77	6.96	7.05	8.16	8.53
8.59	9.28	9.45	9.99	10.01	10.25	10.26	10.28	10.70	11.43
11.62	11.64	11.85	11.91	11.93	12.17	12.87	13.14	13.38	13.42
13.51	13.54	13.79	14.32	14.36	14.79	14.80	14.99	15.02	

Below $a_0 = 15$, 60 eigenmodes could be found with zero displacement boundary condition at the cavity wall. Most of the modes are double due to the symmetry of the geometry. The different eigenfrequencies of the modes are listed in Table 4.1, and the first nine different mode shapes are plotted in Figure 4.7. It is important to notice that for $a_0 < 5$ only two modes are present, for $5 < a_0 < 10$ another 12 modes can be found, and for $10 < a_0 < 15$ the excavation has 25 modes.

For the boundary element computations, the boundary is meshed using $n_E = 131$ constant elements. This fulfills the criterium that 7 elements are used per smallest shear wavelength at the maximal frequency $f_{\max} = 200$ Hz.

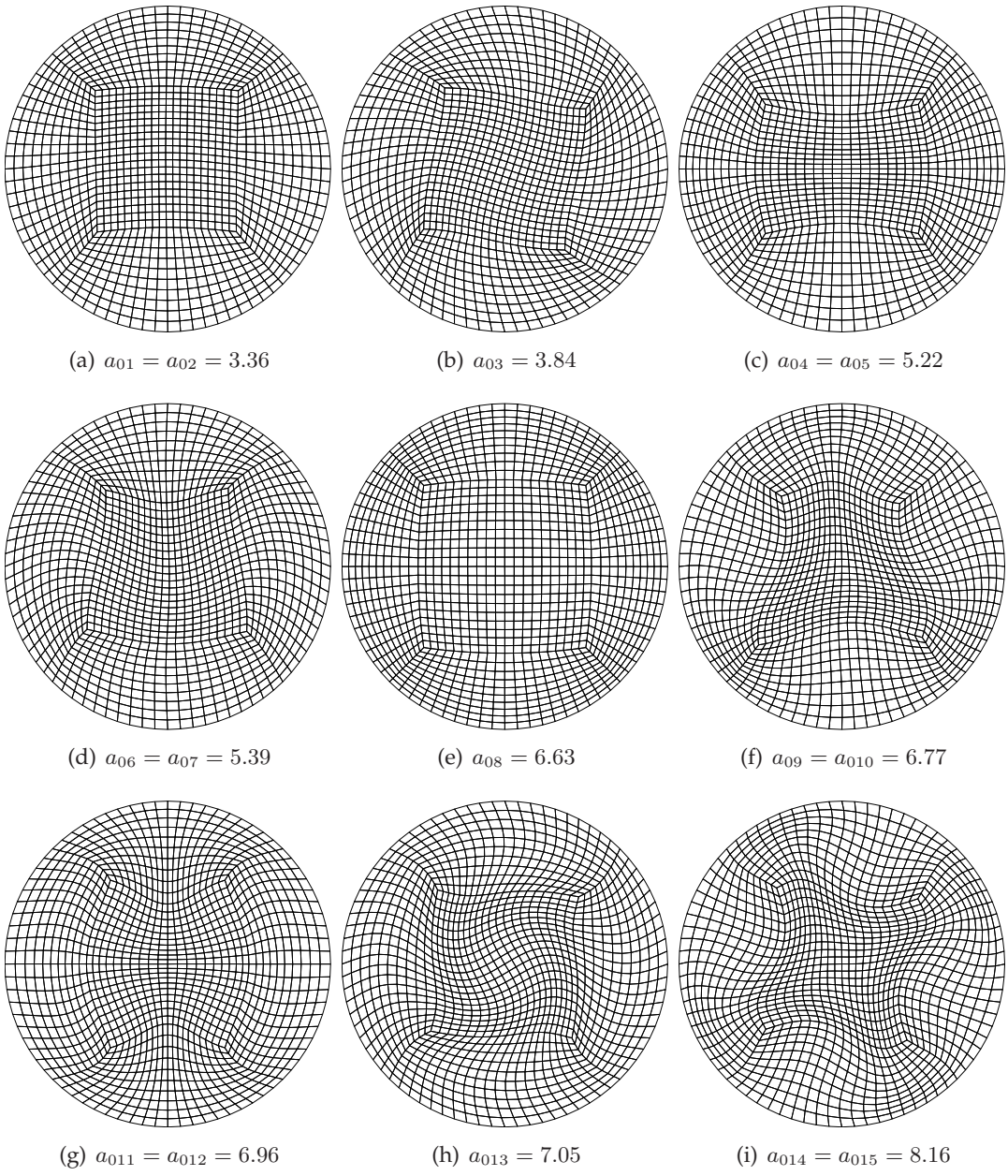

(a) $a_{01} = a_{02} = 3.36$ (b) $a_{03} = 3.84$ (c) $a_{04} = a_{05} = 5.22$

(d) $a_{06} = a_{07} = 5.39$ (e) $a_{08} = 6.63$ (f) $a_{09} = a_{010} = 6.77$

(g) $a_{011} = a_{012} = 6.96$ (h) $a_{013} = 7.05$ (i) $a_{014} = a_{015} = 8.16$

Figure 4.7: Mode shapes of the circular excavation with zero displacement boundary condition along the cavity wall

The dynamic modes of the excavated domain can be found by means of the boundary element method, by searching for the frequencies where the **G** matrix of equation (4.11) has a zero eigenvalue. As it was stated before, at these frequencies, the corresponding exterior problem with zero traction boundary conditions has a non zero displacement field solution. This is ensured if the matrix **H** is also singular at the eigenfrequency. Figure 4.8 plots the condition numbers of the matrices **G** and **H** of the circular excavation over the whole frequency scale. It can be seen that the critical frequencies of the two matrices coincide.

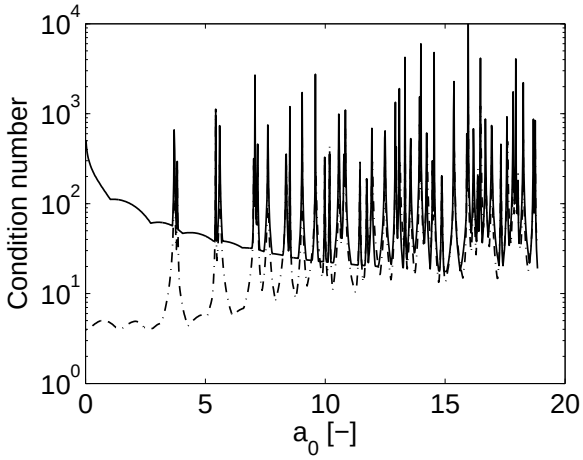

Figure 4.8: Condition numbers of the matrix **G** (solid line) and the matrix **H** (dashed-dotted line) for the case of the circular excavation.

The impedance of the cavity

Three impedance functions are considered. $S_{hh}(a_0)$ corresponds to a rigid body translation motion of the cavity, $S_{\phi\phi}(a_0)$ for a rigid body torsional mode, $S_{rr}(a_0)$ for a radial expansion. Due to the simplicity of the problem, some of the numerically computed impedance functions can be compared with analytical solutions. The horizontal modal impedance $S_{hh}(a_0)$ can be expressed analytically as [WC96]

$$S_{hh}(a_0) = G\pi a_0^2 \frac{A(a_0) + B(a_0) - 4}{A(a_0)B(a_0) - A(a_0) - B(a_0)} \tag{4.33}$$

where

$$A(a_0) = a_0 \frac{H_0^{(2)}(a_0)}{H_1^{(2)}(a_0)} \tag{4.34a}$$

$$B(a_0) = qa_0 \frac{H_0^{(2)}(qa_0)}{H_1^{(2)}(qa_0)} \tag{4.34b}$$

and

$$q = \sqrt{\frac{1-2\nu}{2(1-\nu)}} \tag{4.35}$$

and $H_0^{(2)}$ and $H_1^{(2)}$ are Hankel functions of the second kind and order zero and one.

Figure 4.9 shows the impedance curves $K_{hh}(a_0)$ and $C_{hh}(a_0)$ for the case of $\beta = 0$, obtained using the conventional BEM and with the analytical expression. There is a very good correspondence between the analytical and numerical results, except for seven frequency values. At these frequencies sharp peaks appear in the numerical solution, due to the non-uniqueness of the integral formulation.

The impedance functions of the cavity have been computed using the original integral equation, and also with both mentioned mitigation methods. For the CHIEF method 20

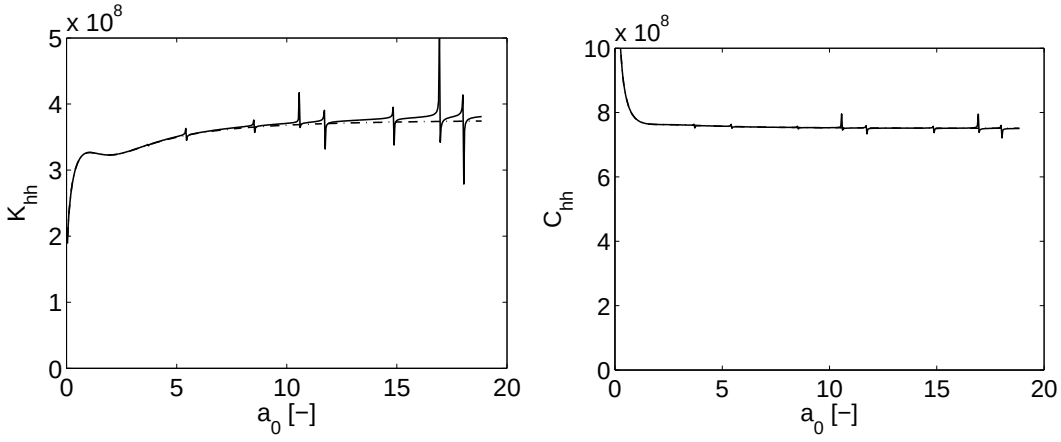

Figure 4.9: Horizontal impedance functions (a) K_{hh} and (b) C_{hh} of the circular cavity obtained by the analytical solution (dash-dotted curve) and by means of the BEM (solid curve).

internal points distributed randomly in the interior domain were used, as shown in figure 4.10a. The non-square system of equations (4.25) of the CHIEF method has been solved by means of a least mean squares algorithm in the form

$$\mathbf{S} = \mathbf{D}\left[\mathbf{G}_s^{\mathrm{T}}\mathbf{G}_s + \mathbf{G}_i^{\mathrm{T}}\mathbf{G}_i\right]^{-1}\left[\mathbf{G}_s^{\mathrm{T}}\mathbf{H}_s + \mathbf{G}_i^{\mathrm{T}}\mathbf{H}_i\right] \tag{4.36}$$

For the case of the modified Burton-Miller algorithm, the distance between the surface and the internal points has been chosen to be equal to the element length, as shown in figure 4.10b, and the coupling parameter has been chosen to $\alpha = i2R/a_{0_{\max}}$.

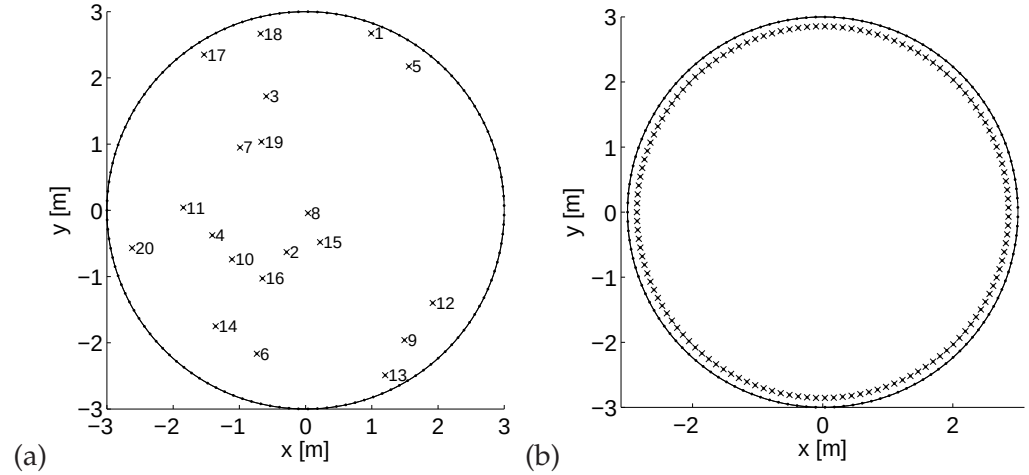

Figure 4.10: Boundary element mesh of the circular cavity (a) for the CHIEF method with 20 randomly chosen internal points, (b) for the Burton-Miller method with $\bar{h} = 1$.

Figure 4.11 compares the impedance curves obtained using the three solution methods.

The effect of fictitious eigenfrequencies is clearly visible in the form of sharp peaks in the figures corresponding to the original integral equation. In figure 4.11a the eigenfrequencies of the internal domain are marked by dotted vertical lines. For the case of the projected

impedance functions only a few internal resonances result in erroneous impedance values, but for the single elements of the **S** matrix the fictitious eigenfrequencies are very dense above $a_0 = 5$. It can be further seen that the material damping of the elastic medium drastically reduces the magnitude of the peaks.

Turning to the second and third columns, it can be stated in general that both methods reduce the amplitude of the peaks at the fictitious eigenfrequencies. For the case of the undamped medium, the CHIEF method gives much better results for all presented impedance curves. Increasing the material damping of the medium, the difference between the two methods decreases.

Comparing the computational cost of the methods, the CHIEF method is more efficient. For the case of the Burton and Miller approach, the number of internal points is equal to the number of surface points, which doubles the computational effort to generate the boundary element system matrices. For the CHIEF method and for this example, 20 interior points were sufficient for accurate results over the total frequency range. As for the CHIEF method the internal points can be placed far from the surface, a numerical integration with a few Gaussian points on the surface elements can be sufficient. For the case of the Burton-Miller approach, the internal points are near to the surface, demanding for a large number of Gaussian points.

Convergence study on the number of CHIEF points

A convergence analysis on the number of CHIEF points has been carried out for the case of the circular cavity. The impedance curves projected on the modes have been recomputed with an increasing number of randomly located CHIEF points. Figure 4.12 shows the real part of the modal impedance at the critical frequencies versus the number of CHIEF points. The results show that a good convergence can be reached with 15 internal points.

4.4.2 Rectangular cavity

A rectangular cavity with side lengths $L_x = 5$ m, $L_y = 3$ m is investigated over the same frequency range $f \in [0 \text{ Hz}; 200 \text{ Hz}]$. The dimensionless frequency a_0 is defined by the relation $a_0 = 2\pi f R/c_S$, where $R = \sqrt{L_x^2 + L_y^2}/2$.

The dynamic modes of the internal domain

The eigenfrequencies of the internal domain with zero displacement boundary conditions have been computed by the 2D finite element method, using a FE mesh of 792 nodes and 735 quadrilateral shell elements. The first few modal shapes are shown in figure 4.14, the lower eigenfrequencies are given in table 4.2.

Table 4.2: Dimensionless eigenfrequencies a_{0i} of the rectangular cavity with zero displacement boundary condition along the cavity wall

4.31	5.42	5.78	6.73	6.86	7.08	8.37	8.85	8.97	9.46
9.70	10.05	10.44	10.85	10.92	11.36	11.42	11.79	12.54	12.60
12.75	12.92	13.10	13.29	13.53	13.77	14.29	14.33	14.59	15.33
15.36	15.57	15.74	15.85	15.93	16.20	16.26	16.31	16.45	17.08

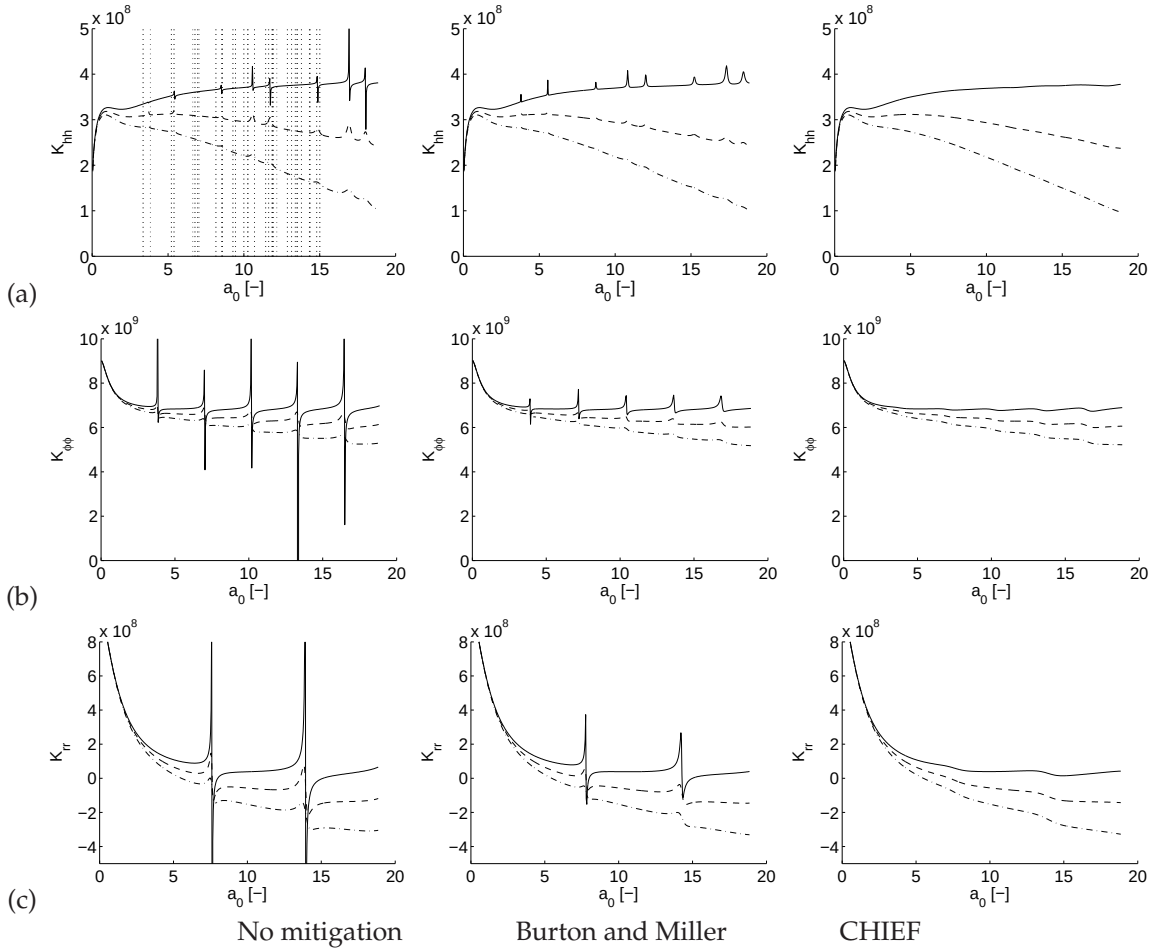

Figure 4.11: Stiffness functions of the circular embedded cavity for different material damping ratios (solid line for $\beta = 0$, dashed line for $\beta = 0.01$, dash-dotted line for $\beta = 0.02$).

The impedance of the cavity

The boundary of the rectangular domain is meshed using $n_E = 108$ elements. This fulfills the criterium that 7 elements are used per smallest shear wavelength at the maximal frequency $f_{\max} = 200$ Hz.

Figure 4.15a shows the boundary element mesh of the rectangular domain with the 20 randomly distributed CHIEF points, while figure 4.15b displays the internal points used for the Burton Miller approach.

Three impedance functions are considered. $S_{xx}(a_0)$ and $S_{yy}(a_0)$ correspond to a rigid body horizontal and vertical translation motions of the cavity, respectively, $S_{\phi\phi}(a_0)$ for a rigid body torsional mode. The real (stiffness) components of these functions are plotted in Figure 4.16 for all three damping coefficients. The same conclusions can be drawn as for the case of the circular cavity. The CHIEF method reduces the effect of the fictitious eigenfrequencies better than the Burton Miller approach, and uses much less internal points.

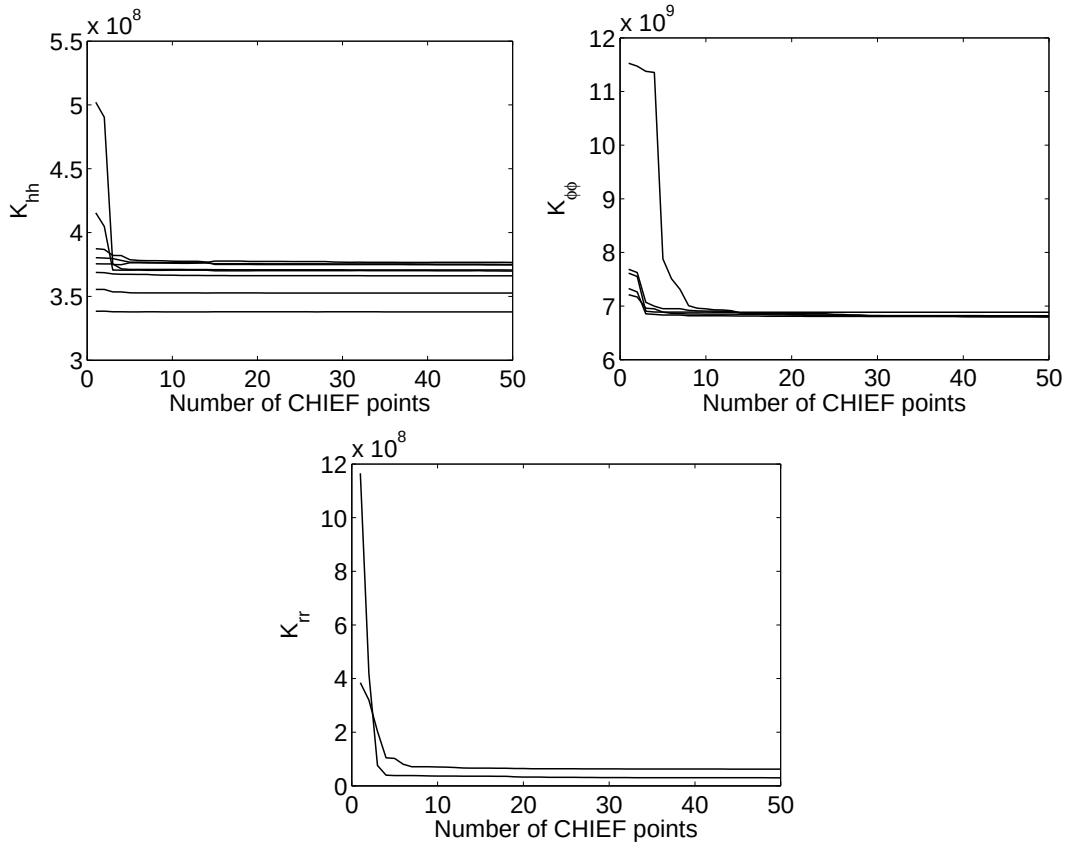

Figure 4.12: Real part of the modal impedance curves of the circular cavity at the eigenfrequencies of the internal domain for an increasing number of CHIEF points

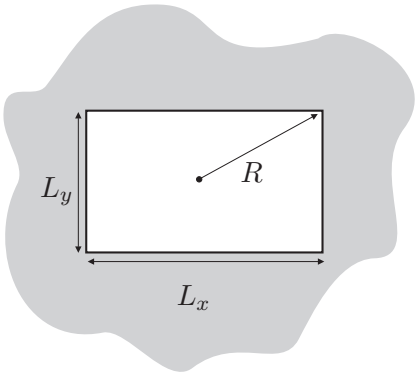

Figure 4.13: Rectangular cavity

4.5 Conclusions

In this chapter, the non-uniqueness problem of the external boundary value problem of elastodynamics was investigated. Two methods have been compared that are capable to mitigate the fictitious eigenfrequencies of the exterior boundary element method. Numerical examples considering impedance functions of two-dimensional embedded cavities in an

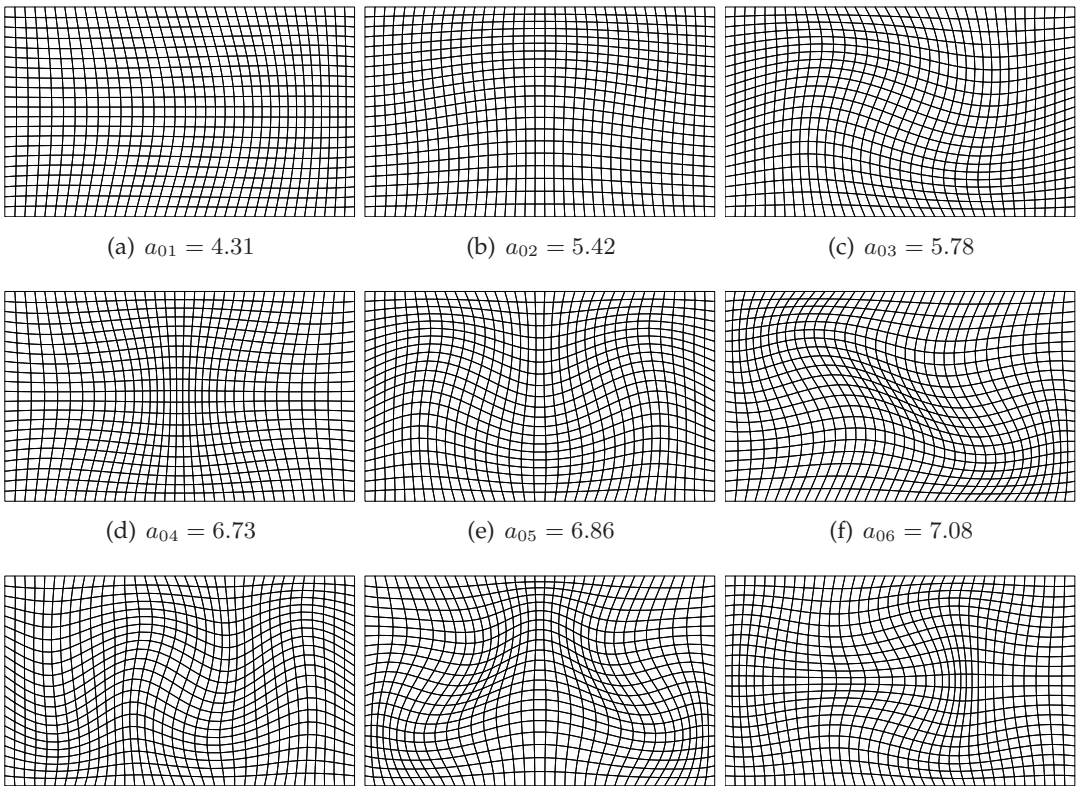

(a) $a_{01} = 4.31$ (b) $a_{02} = 5.42$ (c) $a_{03} = 5.78$

(d) $a_{04} = 6.73$ (e) $a_{05} = 6.86$ (f) $a_{06} = 7.08$

(g) $a_{07} = 8.37$ (h) $a_{08} = 8.85$ (i) $a_{09} = 8.97$

Figure 4.14: Mode shapes of the rectangular cavity with zero displacement boundary condition along the cavity wall

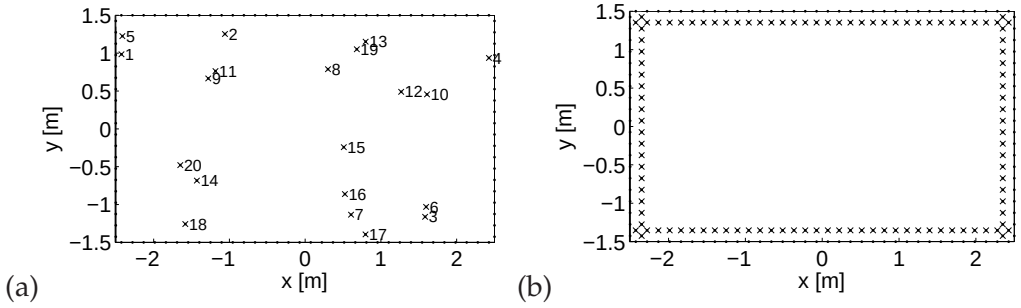

Figure 4.15: Boundary element mesh of the rectangular cavity (a) for the CHIEF method with 20 CHIEF interior points, (b) for the Burton-Miller approach with $\bar{h} = 1$.

elastic full space have been investigated in order to compare the two approaches. The results show that the effect of the critical eigenfrequencies can be very significant in an undamped medium, but as the material damping increases, the significance of the negative effect decreases drastically. Both considered mitigation methods have been found capable to handle the problem of fictitious eigenfrequencies. The drawback of the modified Burton and Miller method is that the choice of the coupling parameter α is crucial, and no general rule can be defined to find the appropriate surface integral equation. The CHIEF method has been

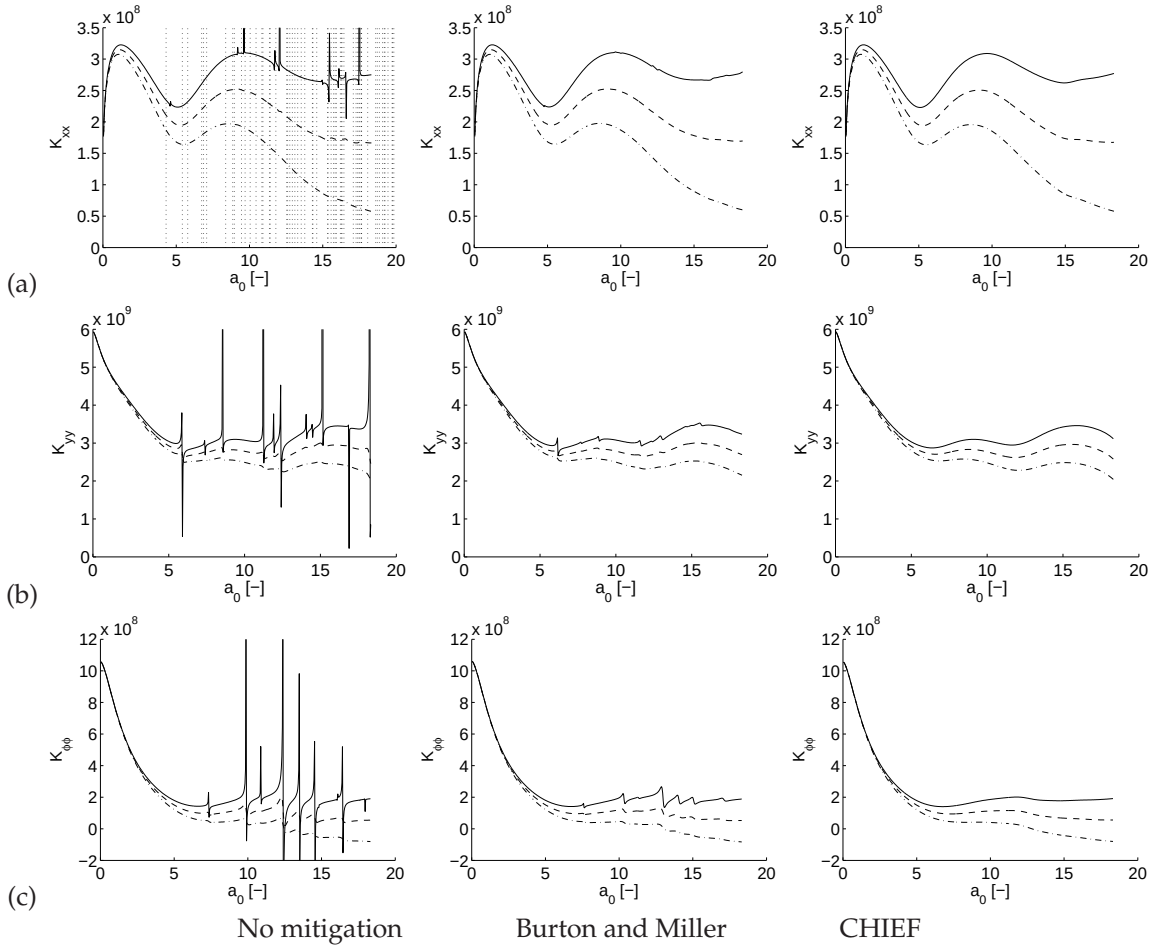

Figure 4.16: Stiffness functions of the rectangular embedded cavity for different material damping ratios (solid line for $\beta = 0$, dashed line for $\beta = 0.01$, dash-dotted line for $\beta = 0.02$).

found more robust and computationally more effective. For the case of the simple geometries considered, a relative small number of randomly located CHIEF points could mitigate the problem of the fictitious eigenfrequencies.

Chapter 5

Re-radiated noise

5.1 Introduction

In the third subproblem, the computed structural displacements $\mathbf{u}_b$ are finally used as vibration input for the computation of ground-borne noise in the building's enclosures.

For typical room dimensions in office buildings or family dwellings, the targeted frequency range is relative low. Therefore, deterministic methods can be used to solve the boundary value problem of sound radiation into a closed space.

Acoustic finite elements [AB94] [Pet98] provide a straightforward method to solve the boundary value problem. The benefit of the application of the FEM for the computation of the sound field in a closed volume is that arbitrary geometry can be modeled. The FEM is capable to handle inhomogeneous media, but, in the case of acoustic modeling this feature is rarely exploited. The drawback of the FEM is that as the element size has to be much smaller than the acoustic wavelength, at high frequencies lots of elements are needed to mesh the full 3D domain. An other disadvantage of the FEM is that the method exhibits numerical dispersion in that the wave number of the numerical solution differs from the wave number of the exact solution [DBB99].

As an alternative, the acoustic boundary element method [BB81] can be used to compute the internal sound field [FDGA06]. This results in a smaller mesh, as the problem dimension is reduced by one. However, the conventional BE formulation based on the Green's function of an acoustic full space results in a fully populated, frequency dependent system of equations, making the solution procedure computationally expensive. These difficulties can be avoided by using the Green's functions of the room [GPVR00] and by formulating a direct integral representation of the internal sound pressure in terms of the walls' velocities. In this form, the boundary element method can provide a more efficient solution than finite elements.

Recently, in the framework of the CONVURT (COntrol of Noise and Vibrations from Underground Railway Traffic) project [www03], a Rayleigh integral based method has been developed and validated for the case of underground railway induced noise in rooms [NFM+06]. This method computes the Green's functions of the room by an image source method, and provides a direct integral representation of the internal pressure in terms of the normal surface velocity. The drawback of the method is that for the case of low wall absorption, lots of image sources have to be taken into account for the computation of the Green's function, what makes the computations expensive.

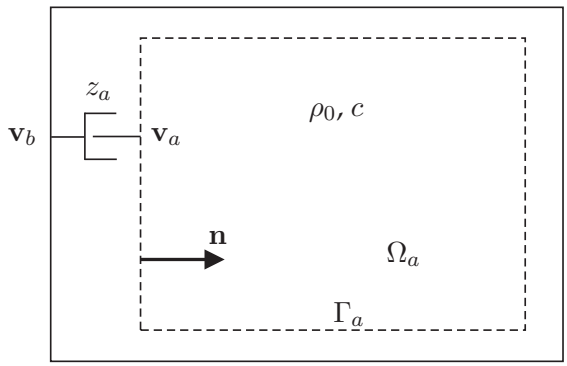

Figure 5.1: The acoustic domain

In the present thesis, an alternative method, a spectral finite element method is introduced for the solution of the acoustic problem. Finite element methods express the internal sound filed as a superposition of simple local or global shape functions, spectral finite element methods [Doy97] [LKL99] use exact solutions of the problem as shape functions. The method introduced here writes the internal sound pressure as a superposition of acoustic room modes. These modes are computed analytically, therefore, no mesh is needed for the computations, and the dispersion error is avoided. The introduced methodology is capable to handle the wall absorption in the form of impedance boundary condition. For the case of low wall absorption or uniform impedance distribution on the walls, the method can also lead to a direct boundary integral representation of the internal sound pressure.

In the following parts of the present chapter, the acoustic radiation problem is introduced, followed by the derivation of the governing equation of the spectral finite element method. The application to a rectangular shoe-box shaped room is discussed in details, and finally, a numerical example demonstrates the capabilities of the method.

5.2 Problem statement

Acoustic wave propagation in the air is governed by the equations of the sound field, giving the relationship of the acoustic pressure p and the acoustic particle velocity vector $\mathbf{v}_a$ in the elastic acoustic medium. The linearized equations of the sound field can be written in the time domain as:

$$\frac{1}{c^2}\dot{p}(\mathbf{x},t) + \rho_0 \nabla \cdot \mathbf{v}_a(\mathbf{x},t) = 0 \tag{5.1}$$

and

$$\rho_0 \dot{\mathbf{v}}_a(\mathbf{x},t) + \nabla p(\mathbf{x},t) = \mathbf{0} \tag{5.2}$$

where $\mathbf{x}$ denotes an arbitrary point in the acoustic medium, t stands for the time, ρ_0 denotes the mass density of the air and c stands for the speed of sound.

When the acoustic response of a closed room to the radiation of the vibrating walls is sought, an interior acoustic problem has to be solved. In an interior problem, the equations of the sound field are solved in a closed acoustic domain Ω_a with a closed boundary Γ_a, as shown in figure 5.1.

A weak coupling between the structural and acoustic vibrations is assumed, meaning that the presence of the sound pressure in the room does not have an effect on the build-

ing's vibrations. So, the structural vibrations can be computed in the absence of the acoustic medium, and in a second step, these vibrations are used as boundary condition in the acoustic computations. This assumption is valid, as the mass density of the air inside the room is much smaller than the density of the vibrating walls. The coupling between the walls' vibration and the acoustic sound field can be written as:

$$p(\mathbf{x},t) = z_a(\mathbf{x})\left[\mathbf{v}_b(\mathbf{x},t) - \mathbf{v}_a(\mathbf{x},t)\right]\mathbf{n}(\mathbf{x}) \qquad \mathbf{x} \in \Gamma_a \tag{5.3}$$

where $\mathbf{n}(\mathbf{x})$ is the internal normal vector of Γ_a, $\mathbf{v}_b(\mathbf{x},t) = \dot{\mathbf{u}}_b(\mathbf{x},t)$ denotes the structural velocity constraint, and $z_a(\mathbf{x})$ stands for the acoustic impedance of the walls.

In order to get rid of the derivatives with respect to time, the governing equations are transformed into the frequency domain by means of a Fourier transform. The resulting equations can be written as:

$$\frac{\mathrm{i}\omega}{c^2}\hat{p}(\mathbf{x},\omega) + \rho_0 \nabla \cdot \hat{\mathbf{v}}_a(\mathbf{x},\omega) = 0 \tag{5.4}$$

and

$$\rho_0 \mathrm{i}\omega \hat{\mathbf{v}}_a(\mathbf{x},\omega) + \nabla \hat{p}(\mathbf{x},\omega) = 0 \tag{5.5}$$

The combination of (5.4) and (5.5) gives the Helmholtz equation:

$$\nabla^2 \hat{p}(\mathbf{x},\omega) + k^2 \hat{p}(\mathbf{x},\omega) = 0 \qquad \mathbf{x} \in \Omega_a \tag{5.6}$$

where $k = \omega/c$ is the acoustic wavenumber.

The boundary condition (5.3) can be transformed to:

$$\hat{p}(\mathbf{x},\omega) = z_a\,(\mathbf{x},\omega)(\hat{\mathbf{v}}_b(\mathbf{x},\omega) - \hat{\mathbf{v}}_a(\mathbf{x},\omega))\,\mathbf{n}(\mathbf{x}) \qquad \mathbf{x} \in \Gamma_a \tag{5.7}$$

Here, a frequency dependent wall impedance can be considered.

5.3 A spectral finite element method

Assume that the pressure $\hat{p}(\mathbf{x},\omega)$ can be written as a superposition of modes in the domain Ω_a:

$$\hat{p}(\mathbf{x},\omega) = \sum_n \Psi_n(\mathbf{x})\hat{Q}_n(\omega) \tag{5.8}$$

where $\Psi_n(\mathbf{x})$ denotes a pressure mode of the internal domain with a corresponding eigenfrequency ω_n, and $\hat{Q}_n(\omega)$ denotes the mode's participation factor or modal coordinate.

The modes are chosen in such a way that they and their spatial derivatives satisfy some orthogonality conditions. The orthogonality condition for the modes can be defined as:

$$\int_{\Omega_a} \Psi_n(\mathbf{x})\Psi_m(\mathbf{x})\mathrm{d}\Omega = \delta_{nm} \tag{5.9}$$

where δ_{nm} is the Cronecker-delta. The orthogonality condition for the spatial derivatives can be written as:

$$\int_{\Omega_a} \nabla\Psi_n(\mathbf{x})\nabla\Psi_m(\mathbf{x})\mathrm{d}\Omega = \delta_{nm}k_n k_m \tag{5.10}$$

where $k_n = \omega_n/c$ is the modal wave number.

The governing equation of the spectral finite element method can be derived by writing the Gauss theorem on the vector field $\Psi_n(\mathbf{x})\nabla\hat{p}$ in the domain Ω_a and on its boundary Γ_a as:

$$\int_{\Omega_a} \nabla\left(\Psi_n(\mathbf{x})\nabla\hat{p}(\mathbf{x},\omega)\right)\mathrm{d}\Omega = -\int_{\Gamma_a} \Psi_n(\mathbf{x})\nabla\hat{p}(\mathbf{x},\omega)\mathbf{n}(\mathbf{x})\mathrm{d}\Gamma \tag{5.11}$$

The minus sign on the right hand side is due to the inward normal $\mathbf{n}(\mathbf{x})$ of the boundary. The left-hand side can be elaborated using the chain-rule, resulting in:

$$\int_{\Omega_a} \nabla\Psi_n(\mathbf{x})\nabla\hat{p}(\mathbf{x},\omega)\mathrm{d}\Omega + \int_{\Omega_a} \Psi_n(\mathbf{x})\nabla^2\hat{p}(\mathbf{x},\omega)\mathrm{d}\Omega = -\int_{\Gamma_a} \Psi_n(\mathbf{x})\nabla\hat{p}(\mathbf{x},\omega)\mathbf{n}(\mathbf{x})\mathrm{d}\Gamma \tag{5.12}$$

Multiplying the second equation of the sound field (5.5) by the normal vector $\mathbf{n}(\mathbf{x})$ and combining the resulting equation with the boundary condition (5.7) yields:

$$\nabla\hat{p}(\mathbf{x},\omega)\mathbf{n}(\mathbf{x}) = \rho_0\mathrm{i}\omega\left(\frac{\hat{p}(\mathbf{x},\omega)}{z_a(\mathbf{x},\omega)} - \hat{\mathbf{v}}_b(\mathbf{x},\omega)\mathbf{n}(\mathbf{x})\right) \tag{5.13}$$

This can be substituted into the right-hand side of (5.12) in order to get:

$$\begin{aligned}\int_{\Omega_a} \nabla\Psi_n(\mathbf{x})\nabla\hat{p}(\mathbf{x},\omega)\mathrm{d}\Omega + \int_{\Omega_a} \Psi_n(\mathbf{x})\nabla^2\hat{p}(\mathbf{x},\omega)\mathrm{d}\Omega + \rho_0\mathrm{i}\omega\int_{\Gamma_a} \Psi_n(\mathbf{x})\frac{\hat{p}(\mathbf{x},\omega)}{z_a(\mathbf{x},\omega)}\mathrm{d}\Gamma \\ = \rho_0\mathrm{i}\omega\int_{\Gamma_a} \Psi_n(\mathbf{x})\hat{\mathbf{v}}_b(\mathbf{x},\omega)\mathbf{n}(\mathbf{x})\mathrm{d}\Gamma\end{aligned} \tag{5.14}$$

Further substituting the Helmholtz equation (5.6) in the second term of the left-hand side of (5.14) results in:

$$\begin{aligned}\int_{\Omega_a} \nabla\Psi_n(\mathbf{x})\nabla\hat{p}(\mathbf{x},\omega)\mathrm{d}\Omega - k^2\int_{\Omega_a} \Psi_n(\mathbf{x})\hat{p}(\mathbf{x},\omega)\mathrm{d}\Omega + \rho_0\mathrm{i}\omega\int_{\Gamma_a} \Psi_n(\mathbf{x})\frac{\hat{p}(\mathbf{x},\omega)}{z_a(\mathbf{x},\omega)}\mathrm{d}\Gamma \\ = \rho_0\mathrm{i}\omega\int_{\Gamma_a} \Psi_n(\mathbf{x})\hat{\mathbf{v}}_b(\mathbf{x},\omega)\mathbf{n}(\mathbf{x})\mathrm{d}\Gamma\end{aligned} \tag{5.15}$$

Making use of the modal decomposition of $\hat{p}(\mathbf{x},\omega)$ (as defined in equation (5.8)) yields:

$$\begin{aligned}&\sum_m \int_{\Omega_a} \nabla\Psi_n(\mathbf{x})\nabla\Psi_m(\mathbf{x})\mathrm{d}\Omega\hat{Q}_m(\omega) - k^2\sum_m \int_{\Omega_a} \Psi_n(\mathbf{x})\Psi_m(\mathbf{x})\mathrm{d}\Omega\hat{Q}_m(\omega) \\ &+\rho_0\mathrm{i}\omega\sum_m \int_{\Gamma_a} \frac{\Psi_n(\mathbf{x})\Psi_m(\mathbf{x})}{z_a(\mathbf{x},\omega)}\mathrm{d}\Gamma\hat{Q}_m(\omega) = \rho_0\mathrm{i}\omega\int_{\Gamma_a} \Psi_n(\mathbf{x})\hat{\mathbf{v}}_b(\mathbf{x},\omega)\mathbf{n}(\mathbf{x})\mathrm{d}\Gamma\end{aligned} \tag{5.16}$$

Taking the orthogonality conditions (5.9) and (5.10) into account, this can be simplified to

$$\begin{aligned}\sum_m k_n k_m\delta_{nm}\hat{Q}_m(\omega) - k^2\sum_m \delta_{nm}\hat{Q}_m(\omega) + \rho_0\mathrm{i}\omega\sum_m \int_{\Gamma_a} \frac{\Psi_n(\mathbf{x})\Psi_m(\mathbf{x})}{z_a(\mathbf{x},\omega)}\mathrm{d}\Gamma\hat{Q}_m(\omega) \\ = \rho_0\mathrm{i}\omega\int_{\Gamma_a} \Psi_n(\mathbf{x})\hat{\mathbf{v}}_b(\mathbf{x},\omega)\mathbf{n}(\mathbf{x})\mathrm{d}\Gamma\end{aligned} \tag{5.17}$$

Further elaborating the left-hand side, the final form of the governing equation is obtained:

$$k_n^2\hat{Q}_n(\omega) + \mathrm{i}k\sum_m D_{nm}(\omega)\hat{Q}_m(\omega) - k^2\hat{Q}_n(\omega) = \mathrm{i}kz_0\int_{\Gamma_a} \Psi_n(\mathbf{x})\hat{\mathbf{v}}_b(\mathbf{x},\omega)\mathbf{n}(\mathbf{x})\mathrm{d}\Gamma \tag{5.18}$$

where

$$D_{nm}(\omega) = \int_{\Gamma_a} \frac{\Psi_n(\mathbf{x})\Psi_m(\mathbf{x})}{\bar{z}_a(\mathbf{x},\omega)} \mathrm{d}\Gamma \tag{5.19}$$

and

$$\bar{z}_a(\mathbf{x},\omega) = \frac{z_a(\mathbf{x},\omega)}{z_0} = \frac{z_a(\mathbf{x},\omega)}{\rho_0 c} \tag{5.20}$$

is the normalized acoustic impedance.

Equation (5.18) can also be expressed in matrix form as:

$$\left(\mathbf{\Lambda} + \mathrm{i}k\mathbf{D} - k^2\mathbf{I}\right)\mathbf{Q} = \mathbf{F} \tag{5.21}$$

where the column vector $\mathbf{Q}$ contains the modal coordinates, $\mathbf{\Lambda} = \mathrm{diag}\left\{k_n^2\right\}$ is the diagonal generalized acoustic stiffness matrix containing the modal wave numbers, $\mathbf{D}$ is the generalized damping matrix, $\mathbf{I}$ denotes the unit matrix and $\mathbf{F}$ stands for the generalized acoustic load vector. The n-th element F_n of this vector is given by

$$F_n = \mathrm{i}kz_0 \int_{\Gamma_a} \Psi_n(\mathbf{x})\hat{\mathbf{v}}_b(\mathbf{x},\omega)\mathbf{n}(\mathbf{x})\mathrm{d}\Gamma \tag{5.22}$$

Equation (5.21) can be used to compute the modal coordinates Q_n if the modes, the excitation velocity and the impedance boundary conditions are known. Finally, the internal pressure response can be obtained by evaluating equation (5.8).

5.3.1 Application to a room

The spectral finite element method provides a computationally efficient way for solving the acoustic wave equation in a closed acoustic domain if the modes Ψ_n of the domain are a-priori known.

For a general problem with arbitrary geometry, this is unfortunately not the case. However, for practical applications for the computation of ground borne noise in buildings with conventional shoe-box shaped rooms, the method is a very efficient way of noise prediction.

For a rectangular room domain defined by the coordinates $0 < x < L_x$, $0 < y < L_y$ and $0 < z < L_z$, the pressure modes $\Psi_n(\mathbf{x})$ with rigid boundary conditions can be written in the form [Pie91]

$$\Psi_n(\mathbf{x}) = \Psi_n(x,y,z) = B_n \cos\left(\frac{\pi l_{x_n} x}{L_x}\right)\cos\left(\frac{\pi l_{y_n} y}{L_y}\right)\cos\left(\frac{\pi l_{z_n} z}{L_z}\right) \tag{5.23}$$

where B_n stands for the modal amplitude and the l_{x_n}, integers l_{y_n}, l_{z_n} give the number of half wavelengths along the three coordinate axes, as shown in figure 5.2.

The wave number k_n of the n-th mode can be given as

$$k_n = \sqrt{k_{x_n}^2 + k_{y_n}^2 + k_{z_n}^2} \tag{5.24}$$

where

$$k_{x_n} = \frac{\pi l_{x_n}}{L_x}, \qquad k_{y_n} = \frac{\pi l_{y_n}}{L_y}, \qquad k_{z_n} = \frac{\pi l_{z_n}}{L_y} \tag{5.25}$$

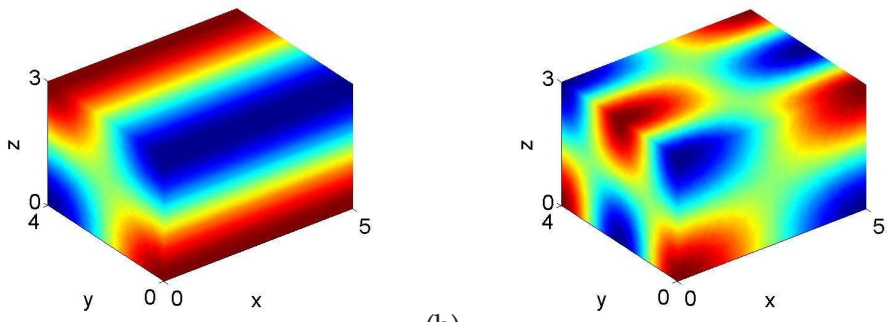

(a) (b)

Figure 5.2: (a) Mode $l_{x_n} = 0$, $l_{y_n} = 1$, $l_{z_n} = 1$ and (b) mode $l_{x_n} = 1$, $l_{y_n} = 2$, $l_{z_n} = 1$ of a shoe-box shaped room with dimensions $L_x = 5$, $L_y = 4$, $L_z = 3$.

The modal amplitude B_n can be determined from the orthogonality condition (5.9):

$$\int_0^{L_x}\int_0^{L_y}\int_0^{L_z}\left[B_n\cos\left(\frac{\pi l_{x_n}x}{L_x}\right)\cos\left(\frac{\pi l_{y_n}y}{L_y}\right)\cos\left(\frac{\pi l_{z_n}z}{L_z}\right)\right]^2 \mathrm{d}z\mathrm{d}y\mathrm{d}x = 1 \tag{5.26}$$

resulting in:

$$B_n = \sqrt{\frac{2^s}{V}} \tag{5.27}$$

where $V = L_xL_yL_z$ is the room's volume and s denotes the number of non-zero values in the set $\{l_{x_n}, l_{y_n}, l_{z_n}\}$.

The damping matrix of a shoe-box shaped room

In the general case of spatially varying acoustic wall impedance $z_a(\mathbf{x},\omega)$, the $D_{nm}(\omega)$ values have to be determined by numerically evaluating the surface integral (5.19) for each mode-pair. However, for some simple cases of impedance distribution, this surface integral can be evaluated analytically.

Constant wall absorption The simplest case is the constant wall absorption over the whole room surface, where

$$D_{nm}(\omega) = \frac{\int_{\Gamma_a}\Psi_n(\mathbf{x})\Psi_m(\mathbf{x})\mathrm{d}\Gamma}{\bar{z}_a(\omega)} \tag{5.28}$$

The integral term in (5.28) can be expressed easily by splitting the boundary surface Γ_a into three sub-surfaces $\Gamma_a = \Gamma_x \cup \Gamma_y \cup \Gamma_z$, as shown in figure 5.3.

Here, for example, Γ_x denotes the surface (two faces of the rectangle) parallel to the yz plane. For this particular surface, the integral can be expressed as:

$$\int_{\Gamma_x}\Psi_n(\mathbf{x})\Psi_m(\mathbf{x})\mathrm{d}\Gamma = \begin{cases} B_nB_mA_x2^{1-s} & \begin{array}{l} l_{y_n} = l_{y_m} \text{ and} \\ \text{if } l_{z_n} = l_{z_m} \text{ and} \\ l_{x_m} - l_{x_n} \text{ is even} \end{array} \\ 0 & \text{otherwise} \end{cases} \tag{5.29}$$

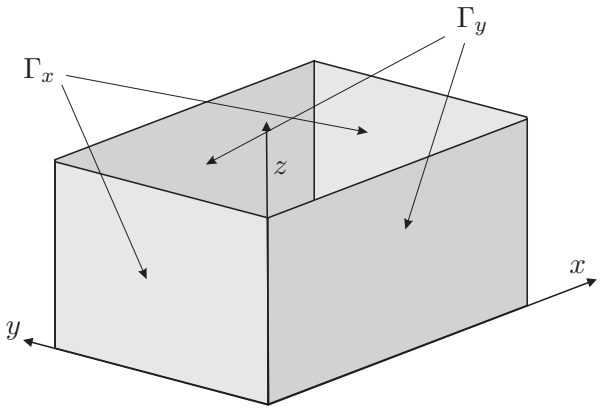

Figure 5.3: The boundary surface Γ_a is split up into three sub-surfaces, Γ_x, Γ_y and Γ_z.

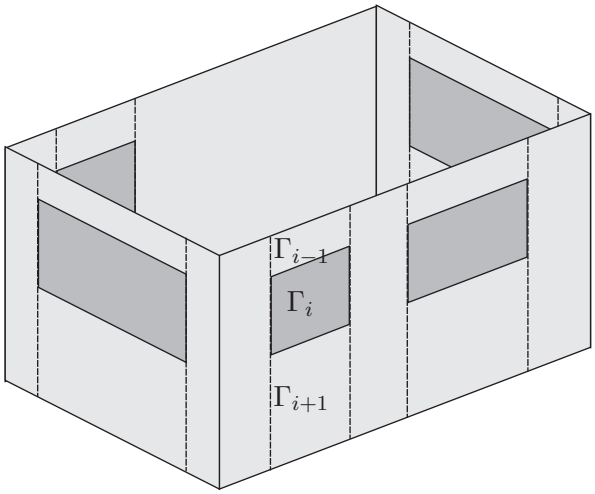

Figure 5.4: For the case of rectangular impedance distribution, the total surface Γ_a is split up into rectangular sub-surfaces Γ_i with constant acoustic impedance.

where $A_x = L_y L_z$, and s denotes the number of non zero values in the set $\{l_{y_n}, l_{z_n}\}$. The integral expressions for the sub-surfaces Γ_y and Γ_z can be obtained by the cyclic permutation of the variables l_{x_n}, l_{y_n} and l_{z_n}.

Rectangular wall absorption distribution A second simple but practically important case is the rectangular wall absorption distribution, where the room's surface Γ_a can be split up into a number of rectangular faces Γ_i, and the impedance has a constant value on each face, as shown in figure 5.4.

For this case the $D_{nm}(\omega)$ values can be expressed as:

$$D_{nm}(\omega) = \int_{\Gamma_a} \frac{\Psi_n(\mathbf{x})\Psi_m(\mathbf{x})}{\bar{z}_a(\mathbf{x},\omega)} \mathrm{d}\Gamma = \sum_{i=1}^{N_\Gamma} \frac{\int_{\Gamma_i} \Psi_n(\mathbf{x})\Psi_m(\mathbf{x})\mathrm{d}\Gamma}{\bar{z}_{ai}(\omega)} \tag{5.30}$$

The surface integral on the right-hand side of (5.30) can be evaluated analytically for each rectangular face. Considering a face parallel with the xy plane at the position $x_1 < x < x_2$,

$y_1 < y < y_2$ and $z = L_z$, the integral can be written as:

$$\begin{aligned}\int_{\Gamma_i} \Psi_n(\mathbf{x})\Psi_m(\mathbf{x})\mathrm{d}\Gamma &= \int_{x_1}^{x_2}\int_{y_1}^{y_2} \Psi_n(x,y,L_z)\Psi_m(x,y,L_z)\mathrm{d}y\mathrm{d}x \\ &= B_n B_m \cos(\pi l_{z_n}) \cos(\pi l_{z_m})\, I_x I_y \end{aligned} \tag{5.31}$$

where

$$I_x = \int_{x_1}^{x_2} \cos\left(\frac{\pi l_{x_n} x}{L_x}\right) \cos\left(\frac{\pi l_{x_m} x}{L_x}\right) \mathrm{d}x \tag{5.32a}$$

$$I_y = \int_{y_1}^{y_2} \cos\left(\frac{\pi l_{y_n} y}{L_y}\right) \cos\left(\frac{\pi l_{y_m} y}{L_y}\right) \mathrm{d}y \tag{5.32b}$$

The expression for the integral I_x is further split up into two parts:

$$I_x = \frac{I_{x_1} + I_{x_2}}{2} \tag{5.33}$$

where

$$I_{x_1} = x_2 \mathrm{sinc}\left(\frac{\pi(l_{x_n} + l_{x_m})x_2}{L_x}\right) - x_1 \mathrm{sinc}\left(\frac{\pi(l_{x_n} + l_{x_m})x_1}{L_x}\right) \tag{5.34a}$$

and

$$I_{x_2} = x_2 \mathrm{sinc}\left(\frac{\pi(l_{x_n} - l_{x_m})x_2}{L_x}\right) - x_1 \mathrm{sinc}\left(\frac{\pi(l_{x_n} - l_{x_m})x_1}{L_x}\right) \tag{5.34b}$$

For the expression of I_y, the formulas (5.33-5.34b) can be applied with the proper replacement of the variables (x by y).

The loading term

As the normal surface velocity $\hat{v}(\mathbf{x}) = \hat{\mathbf{v}}_b(\mathbf{x})\mathbf{n}(\mathbf{x})$ can have any arbitrary distribution over the surface, the loading term on the right-hand side of (5.18) has to be evaluated numerically. For the evaluation of this integral, a surface mesh has to be introduced.

The surface velocity distribution is represented by its nodal samples $v_j = v(\mathbf{x}_j)$ and shape functions $N_j(\mathbf{x})$ that are chosen so that $N_j(\mathbf{x}_i) = \delta_{ij}$. With these definitions, the integral can be written as

$$\int_{\Gamma_a} \Psi_n(\mathbf{x})\hat{v}(\mathbf{x},\omega)\mathrm{d}\Gamma = \sum_j \hat{v}_j(\omega) \int_{\Gamma_a} \Psi_n(\mathbf{x}) N_j(\mathbf{x})\mathrm{d}\Gamma \tag{5.35}$$

Here, the integral term on the right hand side has to be evaluated numerically for each mode and shape function pair.

5.4 Numerical example

In the following, a numerical example will be considered in order to demonstrate the capabilities of the described method. In the numerical example, the interior noise in a shoe-box shaped room due to simple structural velocity excitation distributions on the wall is computed.

Table 5.1: Modal numbers and eigenfrequencies of the first few modes of the room.

n	l_{x_n}	l_{y_n}	l_{z_n}	f_n[Hz]	n	l_{x_n}	l_{y_n}	l_{z_n}	f_n[Hz]
1	0	0	0	0.00	21	3	0	1	117.71
2	1	0	0	34.30	22	1	0	2	119.37
3	0	1	0	42.88	23	0	1	2	122.11
4	1	1	0	54.91	24	2	2	1	123.80
5	0	0	1	57.17	25	3	1	1	125.28
6	1	0	1	66.67	26	1	1	2	126.83
7	2	0	0	68.60	27	0	3	0	128.63
8	0	1	1	71.46	28	1	3	0	133.12
9	1	1	1	79.26	29	2	0	2	133.33
10	2	1	0	80.90	30	3	2	0	133.95
11	0	2	0	85.75	31	4	0	0	137.20
12	2	0	1	89.30	32	2	1	2	140.06
13	1	2	0	92.36	33	0	3	1	140.76
14	2	1	1	99.06	34	0	2	2	142.92
15	3	0	0	102.90	35	4	1	0	143.74
16	0	2	1	103.06	36	1	3	1	144.88
17	1	2	1	108.62	37	3	2	1	145.63
18	2	2	0	109.81	38	2	3	0	145.78
19	3	1	0	111.48	39	1	2	2	146.98
20	0	0	2	114.33	40	4	0	1	148.63

5.4.1 Model description

The dimensions of the room are: $L_x = 5\ \mathrm{m}$, $L_y = 4\ \mathrm{m}$ and $L_z = 3\ \mathrm{m}$. The material properties of the air inside the room are given by $c = 343\ \mathrm{m/s}$ and $\rho_0 = 1.125\ \mathrm{kg/m^3}$.

At relative low frequencies, the acoustic impedance can be computed from the walls' acoustic absorption coefficient α, which gives the ratio of the absorbed and the incident acoustic energy when a normal incident acoustic plane wave is reflected from the surface. The relation between the acoustic absorption coefficient and the wall's impedance can be approximated as

$$z_a = \rho_0 c \frac{1 + \sqrt{1-\alpha}}{1 - \sqrt{1-\alpha}} \tag{5.36}$$

Three different frequency independent absorption coefficients are considered: $\alpha = 0$ describes the non realistic case of no absorption, $\alpha = 0.01$ describes a strongly reflecting room, and $\alpha = 0.1$ describes a weakly reflecting room.

5.4.2 The acoustic modes of the room

The acoustic modes of the room with rigid boundary conditions can be obtained by evaluating equation (5.23). The modal numbers and the eigenfrequencies of the first few modes of the room are given in table 5.1. The total number of modes as a function of upper frequency limit is plotted in figure 5.5.

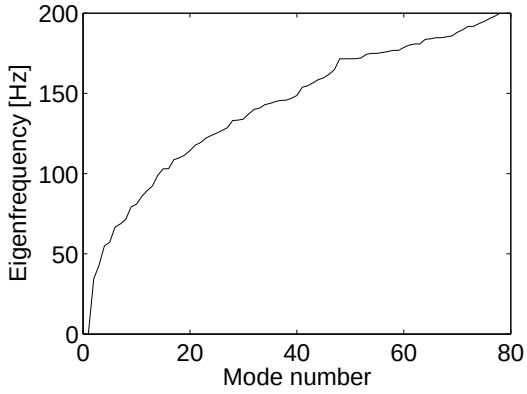

Figure 5.5: Eigenfrequencies of the rectangular room as a function of mode number

5.4.3 The response to a uniform vibration excitation on one wall

In the numerical example, one wall of the room vibrates with a uniform frequency independent normal velocity of $\hat{v} = 1\ \mathrm{m/s/Hz}$, and the remaining five walls are still. The vibrating wall is in the $x = 0$ plane, as shown in figure 5.6. This vibration pattern leads to a sparse generalized excitation vector $\mathbf{F}$. Only those values of the vector will be non zero, where the corresponding mode does not vary in the yz plane. In other words, where $l_{y_n} = l_{z_n} = 0$.

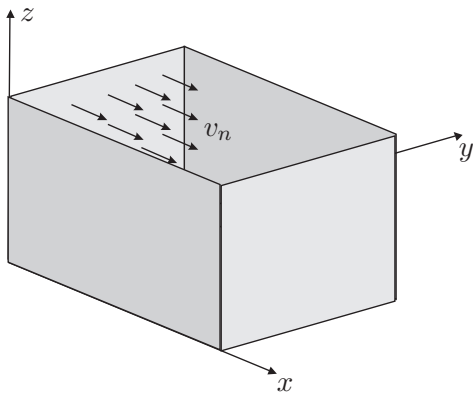

Figure 5.6: Uniform normal structural velocity distribution on the wall at $x = 0$

The modal coordinates $Q_n(\omega)$ of the room's pressure response are shown in figure 5.7. Figure 5.7a corresponds to $\alpha = 0$, the non realistic case of no absorption, where the room's walls are perfectly reflecting. In this case, the matrix $\mathbf{D}$ in equation (5.21) vanishes, and the total left hand side is diagonal. This means that the modal coordinate $Q_n(\omega)$ of the n-th mode is fully determined by the projection of the excitation velocity on the n-th mode $\Psi_n(\mathbf{x})$ and this mode's eigenfrequency ω_n as

$$Q_n = \frac{\mathrm{i}kz_0}{k_n^2 - k^2} \int_\Gamma \Psi_n(\mathbf{x}) \hat{\mathbf{v}}_b(\mathbf{x}, \omega) \mathbf{n}(\mathbf{x}) \mathrm{d}\Gamma \tag{5.37}$$

Comparing the location of the peaks in figure 5.7a with the eigenfrequencies in table 5.1, it can be seen that those modes are excited where $l_{y_n} = l_{z_n} = 0$. This result is in accordance

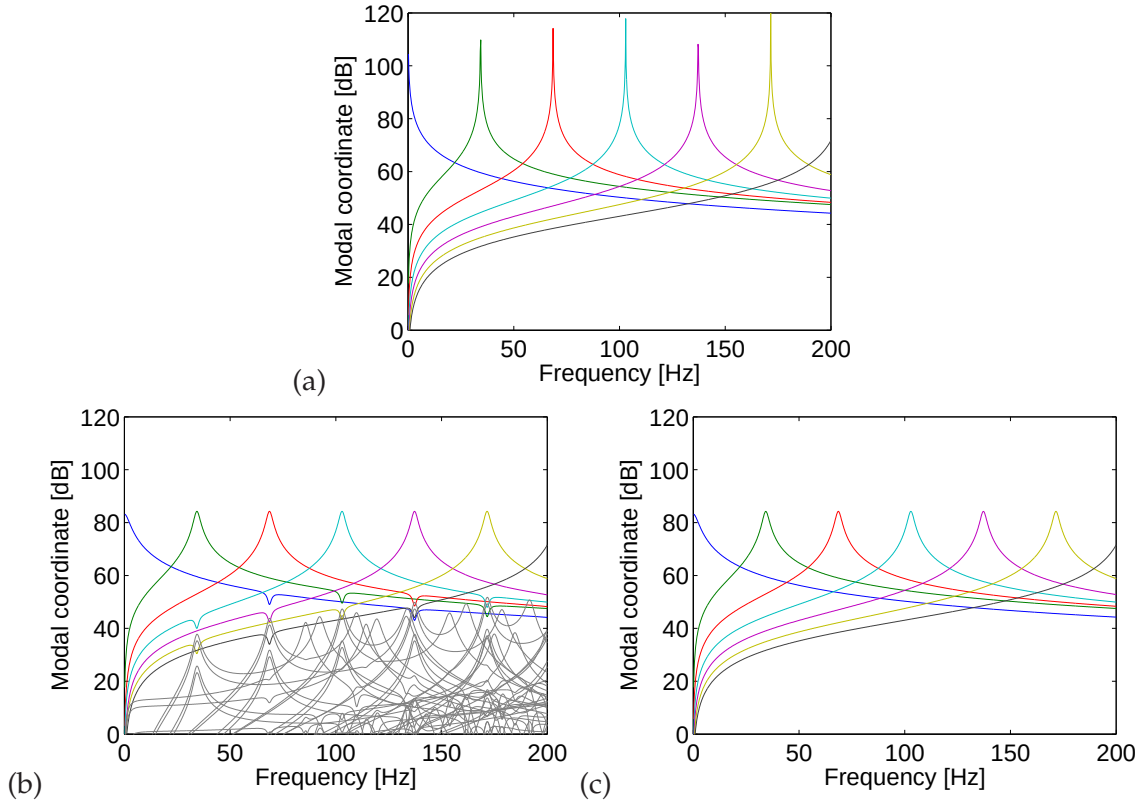

Figure 5.7: Modal coordinates $Q(\omega)$ of the room's pressure response due to the unit velocity excitation of one wall for (a) $\alpha = 0$, (b) $\alpha = 0.1$ and (c) $\alpha = 0.1$ with the diagonal truncation of the matrix $\mathbf{D}$.

with the simple vibration distribution.

For the case of the non zero wall absorption values, the matrix $\mathbf{D}$ in equation (5.21) does not vanish, what makes the linear system of equations more complicated. The structure of the matrix is plotted in figure 5.8(a) for the present case of constant wall absorption over the wall's surface. In the figure, the matrix is normalized by the acoustic impedance, and the $\bar{z}_a D_{nm}$ values are shown. The figure shows that the matrix is sparse, it has a dominating diagonal part and small magnitude off-diagonal elements. These off-diagonal elements are responsible for the coupling between different modes. Figure 5.7b shows the modal coordinates of the pressure response for the case of the highest wall absorption value considered, $\alpha = 0.1$. The dominating modes are the same as for the case of no absorption, but the sharp resonance peaks at the eigenfrequencies are significally damped. The effect of mode coupling can be detected in the figure: there is a small dip in the curve of mode $(l_{x_n}, 0, 0)$ at the eigenfrequency of mode $(l_{x_n} \pm 2, 0, 0)$. Moreover, lots of higher order modes (plotted with gray in the figure) are also excited in the investigated frequency range due to the mode coupling. However, the participation factor of these modes is more than 30 dB smaller than the magnitude of the dominating modes. So, their participation in the pressure response may be neglected.

The effect of mode coupling can easily be disregarded by truncating the matrix $\mathbf{D}$ to

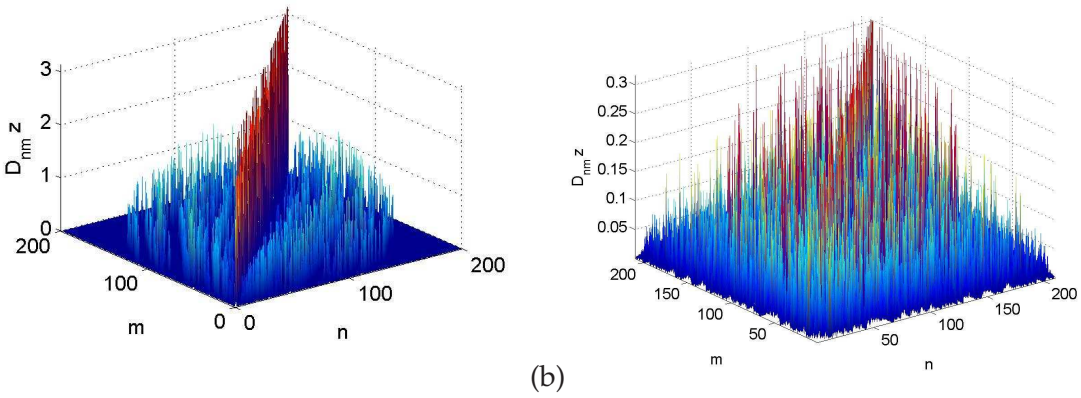

(a) (b)

Figure 5.8: The normalized damping matrix $\bar{z}_a(\omega)D_{nm}(\omega)$ for the case of the (a) uniform impedance distribution over the whole room surface and (b) the rectangular impedance distribution defined by the wall openings

diagonal. For this case, the modal coordinate Q_n can be directly computed as

$$Q_n = \frac{\mathrm{i}kz_0 \int_\Gamma \Psi_n(\mathbf{x})\hat{\mathbf{v}}_b(\mathbf{x},\omega)\mathbf{n}(\mathbf{x})\mathrm{d}\Gamma}{k_n^2 + \mathrm{i}k\int_\Gamma \frac{\Psi_n^2(\mathbf{x})}{\bar{z}_a(\mathbf{x},\omega)}\mathrm{d}\Gamma - k^2} \tag{5.38}$$

Figure 5.7c shows the modal coordinates of the pressure response for this case. Comparing figures 5.7b and 5.7c, it can be stated that the truncation has a very slight effect on the amplitude of the dominating modes, and therefore, it has a negligible effect on the pressure response. From a computational point of view, the truncation leads to a very fast algorithm for the determination of the re-radiated noise, even when the wall absorption is accounted for.

5.4.4 Modeling of wall openings by absorbing boundary condition

As the described spectral finite element method can only handle shoe-box shaped domains with a closed boundary, it is not able to handle the case of wall openings. However, as wall openings can often be modeled with absorbing boundary condition, their influence on the re-radiated noise in the room can be approximated.

Figure 5.9 displays the three wall openings defined on the surface of the room model. One window is located at $0.5 \leq x \leq 1$, $y = 4$, $1 \leq z \leq 2.5$. A second window is located at $3 \leq x \leq 4.5$, $y = 4$, $1 \leq z \leq 2.5$. The door is defined at $3 \leq x \leq 4.5$, $y = 4$, $0 \leq z \leq 2.5$. The absorbing boundary condition is an acoustic impedance of $z_a = \rho_0 c$ and zero structural velocity at the wall openings.

Figure 5.8(b) shows the structure of the normalized damping matrix $\bar{z}_a D_{nm}$ for this case of the boundary condition. Comparing this matrix with the damping matrix of the uniform wall impedance boundary condition, the difference can be clearly seen. For the case of the non uniform impedance distribution, the matrix is not sparse any more and although its diagonal part still dominates, the matrix can not be approximated with its diagonal truncation.

Figure 5.10 shows the modal coordinates of the acoustic response for the case of the wall openings. Due to the wall openings, the effect of modal coupling is very significant, even for

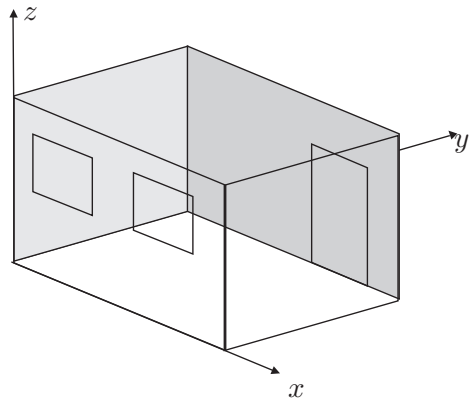

Figure 5.9: Wall openings defined on the surface of the room

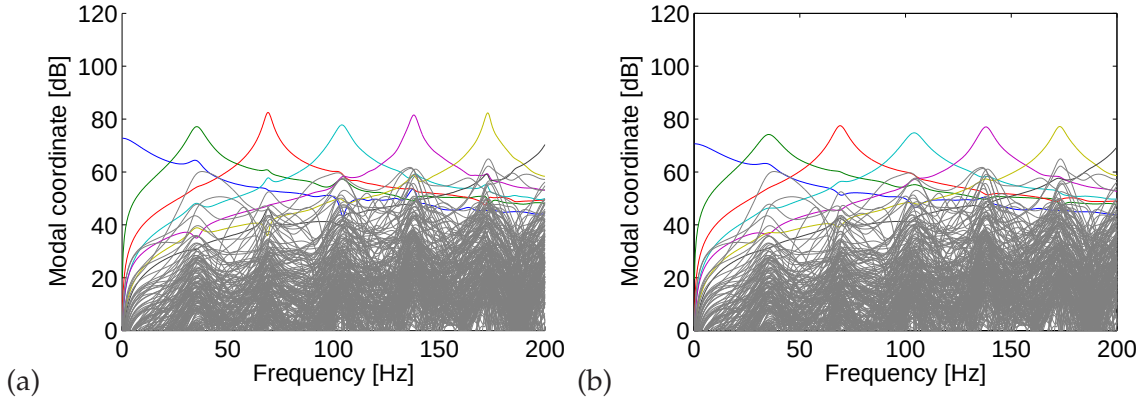

Figure 5.10: Modal coordinates $Q(\omega)$ of the room's pressure response due to the unit velocity excitation of one wall for the case of the wall openings and for (a) $\alpha = 0$, (b) $\alpha = 0.1$.

the zero absorption case $\alpha = 0$. As the two plots in figure 5.10 are close to identical, it can be stated that although the total surface of the wall openings is only 6% of the total surface of the walls and floors, the effect of the wall openings on the internal pressure response is much more important than the absorbing properties of the room's surfaces.

Chapter 6

Ground-borne noise and vibration in an office building due to surface rail traffic

6.1 Introduction

In the present chapter a complex numerical example is presented, as an application of the methodology described in sections 2-5. Ground-borne noise and vibrations in a portal frame office building due to the passage of a Thalys high-speed train on an uneven track are considered. The effect of dynamic soil-structure interaction on the structural vibrations and ground-borne sound is investigated, and the model is further used to investigate the effectiveness of vibration and noise isolation methods.

To the author's knowledge, this is the first application, when a coupled numerical model is used to describe the whole vibration chain starting from vibration generation by a moving vehicle and ending with the re-radiated noise in a building.

6.2 The incident wave field

Several authors recently published coupled train-track-soil models to predict the incident wave field generated by moving sources. The track is often represented by an infinite beam supported by distributed springs [MVB05], a layered infinite beam model [SJP99a], or a finite element model [Aue05]. For the modeling of the underlying ground, homogeneous half space models [MVB05] or layered half space models [SJP99a] [MK00] [SJP99b] are frequently used. In the present paper, the model of Lombaert et al. is used for the computation of the incident wave field. This model, originally developed for the prediction of road traffic induced vibrations [Lom01] [LD01] [LD03], and extended to handle the case of (high-speed) train excitation [LDKF06], consists of a lumped parameter vehicle model, infinite beams modeling the track, and a boundary element method based on the Green's functions of a layered half space to model the ground. The model accounts for the dynamic interaction between the train, the track and the soil.

The model of a moving vehicle on a longitudinally invariant track is used to compute the incident wave field. The invariance of the track in the longitudinal y-direction enables to

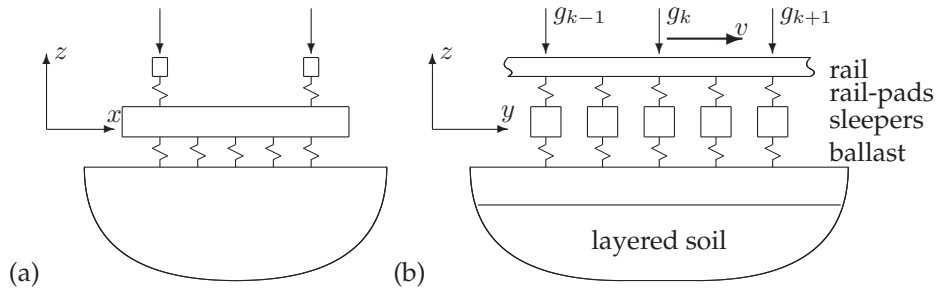

Figure 6.1: (a) Cross section of the track, in the x-z plane and (b) longitudinal section in the y-z plane

transform the spatial variable y into the longitudinal wavenumber k_y by means of a Fourier transform and compute the response to moving loads in the frequency-wavenumber domain [LDC00].

The vehicle is modeled by a set of concentrated masses, representing the train's axles, connected to the track by Hertzian springs. The invariant track is modeled by a pair of Euler beams representing the rails, distributed spring-dampers representing the rail pads, distributed mass for the sleepers and a spring-damper system for the ballast layer, as shown in figure 6.1. The track is laying on a horizontally layered soil, characterized by its shear wave velocity C_{S}, compressional wave velocity C_{P}, material density ρ, and hysteretic material damping ratio β for each homogeneous layer.

First, the vehicle-track interaction problem is solved in a frame of reference that is moving with the train velocity v along the invariant direction y. The compliance matrices of the vehicle $\hat{\mathbf{C}}^v(\omega)$ and the track-soil system $\hat{\mathbf{C}}^t(\omega)$ are written in the moving frame of reference. These matrices are used to compute the dynamic axle loads $\hat{\mathbf{g}}(\omega)$ arising due to the rail unevenness $\hat{\mathbf{u}}_{w/r}(\omega)$ as:

$$\left[\hat{\mathbf{C}}^v(\omega) + \hat{\mathbf{C}}^t(\omega)\right] \hat{\mathbf{g}}(\omega) = -\hat{\mathbf{u}}_{w/r}(\omega) \tag{6.1}$$

The elements of the vector $\hat{\mathbf{u}}_{w/r}(\omega)$ are the frequency content of the rail unevenness as experienced by the axles of the vehicle, while the elements of the vector $\hat{\mathbf{g}}(\omega)$ are the forces acting on the coupled track-soil model, as shown in figure 6.1.

The soil's stiffness, which is incorporated in the track-soil compliance matrix, is computed in the frequency-wavenumber domain by means of a boundary element method [Lom01] using the Green's functions of a layered half space.

In a second phase, the free field soil vibrations due to a set of moving axle loads $\hat{g}_k(\omega)$ are computed in the frequency-wavenumber domain [Lom01]:

$$\tilde{u}_{si}(x, k_y, z, \omega) = \sum_{k=1}^{n} \hat{g}_k(\omega - k_y v) \tilde{h}_{zi}(x, k_y, z, \omega) e^{ik_y y_k} \tag{6.2}$$

where $\tilde{h}_{zi}(x, k_y, z, \omega)$ is the transfer function in the frequency-wavenumber domain between a load on the track at position $y = 0$ and a point in the far field at coordinates $\{x, z\}$. The response in the spatial-time domain is then obtained by applying a double inverse Fourier transform.

A Thalys high-speed train [LDKF06] [DS01] traveling with a velocity $v = 80$ m/s on an uneven rail is modeled. The 200 m long train consists of two locomotives and eight

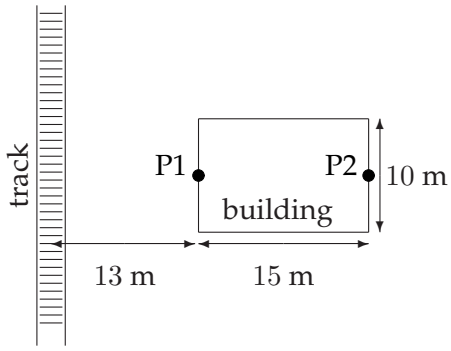

Figure 6.2: Ground plan of the site.

carriages, having a total number of 26 axles distributed over 13 bogies. Each axle is modeled by a concentrated mass of 2027 kg.

The track is modeled as a single ballasted track with a rail gauge of 1.435 m. The rail has a bending stiffness of 6.489×10^6 Nm^2 and a mass of 60.8375 kg/m.

The sleepers, the resilient rail pads and the ballast are modeled by smeared mass, springs and dashpots. The sleepers' dimensions are $2.5 \times 0.24 \times 0.21$ m, the sleeper distance is 0.6 m, and the smeared sleeper mass is 525 kg/m. The rail pad stiffness is 235.6×10^6 N/m^2 and the rail pad damping is 25.1×10^3 Ns/m^2. The ballast mass is 1750 kg/m, the ballast stiffness is 125.8×10^6 N/m^2, while the ballast damping is 41.3×10^3 Ns/m^2. The underlying soil is modeled as a homogeneous half space with a shear wave velocity $C_{\mathrm{S}} = 250$ m/s, a compressional wave velocity $C_{\mathrm{P}} = 500$ m/s, a mass density $\rho = 1750$ kg/m^3 and a material damping coefficient $\beta = 0.025$. The rail unevenness is characterized by its power spectral density $S_{u_{w/r}}(k_y)$ that decreases with the longitudinal wavenumber k_y as [LDKF06]:

$$S_{u_{w/r}}(k_y) = S_{u_{w/r}}(k_{y_0})(k_y/k_{y_0})^{-w}, \tag{6.3}$$

where $S_{u_{w/r}}(k_{y_0}) = 1.38 \times 10^{-8}$ m^3/rad, $k_{y_0} = 1$ rad/m and $w = 3.5$.

Figure 6.3 shows the vertical component of the free field incident velocity computed in two points, P1 and P2, as indicated in figure 6.2. P1 is located on the soil's surface at a distance of 13 m from the central line of the track, while P2 lies 28 m from the track. The dominating part of the frequency content is between 20 Hz and 80 Hz, but vibrations up to 150 Hz are also present in the incident wave field. The largest peaks around 50 Hz correspond to the resonance of the train's axles on the coupled track-soil system. The time history extends from -2 s until 2 s. The equidistant sharp peaks correspond to the 13 bogies of the train. Comparing the vibration levels in the two points, significant attenuation can be observed above 30 Hz, due to the geometrical and material damping in the soil.

6.3 The structural response

6.3.1 The office building model

The finite element mesh of the portal frame structure is shown in figure 6.4. The building's dimensions are 15 m $\times$ 10 m $\times$ 9.6 m, and the distance between the track's central line and the nearest edge of the structure is 13 m.

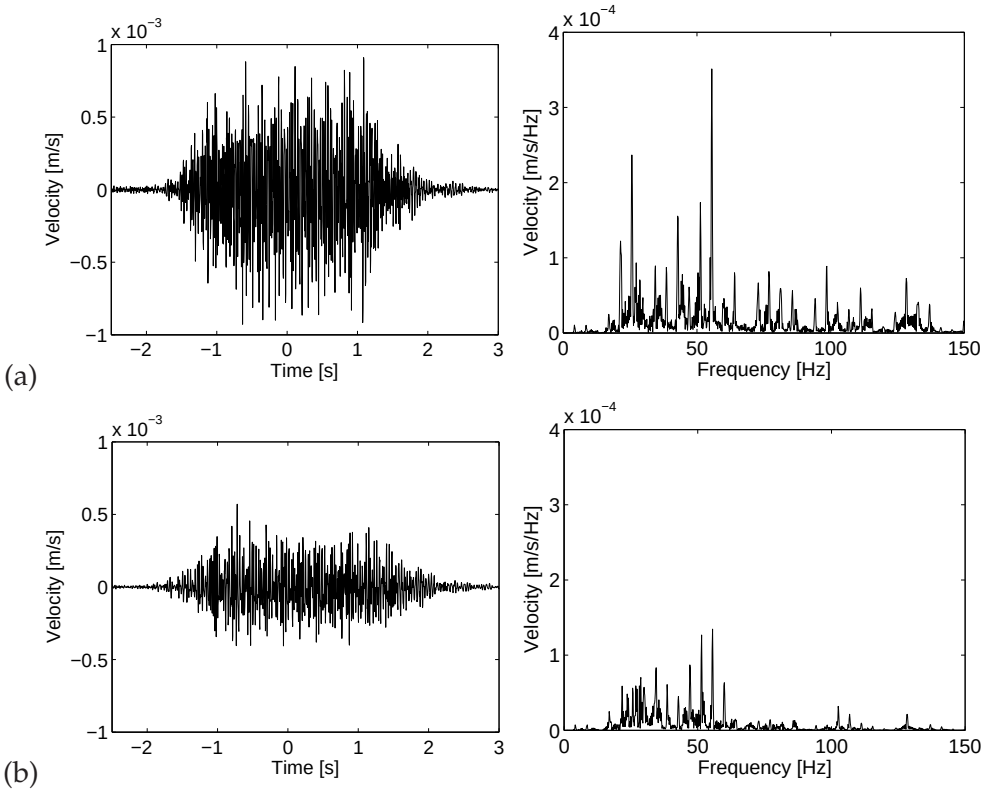

Figure 6.3: Time history and frequency content of the free field vertical velocity in the points (a) P1 and (b) P2.

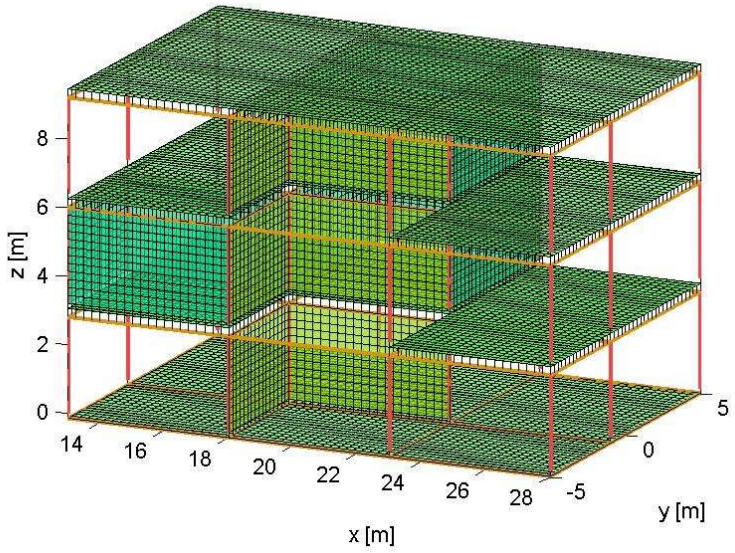

Figure 6.4: Finite element mesh of the office building.

The three story superstructure is supported by a 0.3 m thick reinforced concrete raft foundation. The basic structure consists of a reinforced concrete portal frame structure containing vertical columns of cross sectional dimensions 0.3×0.3 m and horizontal beams of dimensions 0.3×0.2 m. This frame structure supports three 0.3 m thick horizontal slabs. The structure has a reinforced concrete central core which surrounds the stair-case. The thickness of the core walls is 0.15 m. The structural model is extended with the in-fill walls of three rooms besides the core. Room 1 has dimensions $5 \times 6 \times 3$ m, and is located in the first floor, behind the core wall; room 2, which has the same dimensions, is located on the second floor; a smaller room 3 with dimensions $5 \times 4 \times 3$ m is located on the first floor, besides the core. The masonry in-fill walls are 0.06 m thick.

The finite element size is chosen as 0.25 m, which is fine enough for computations up to 200 Hz. The total model has 85518 degrees of freedom. A constant hysteretic structural damping of $\beta_s = 0.025$ is assumed.

6.3.2 The modes of the structure

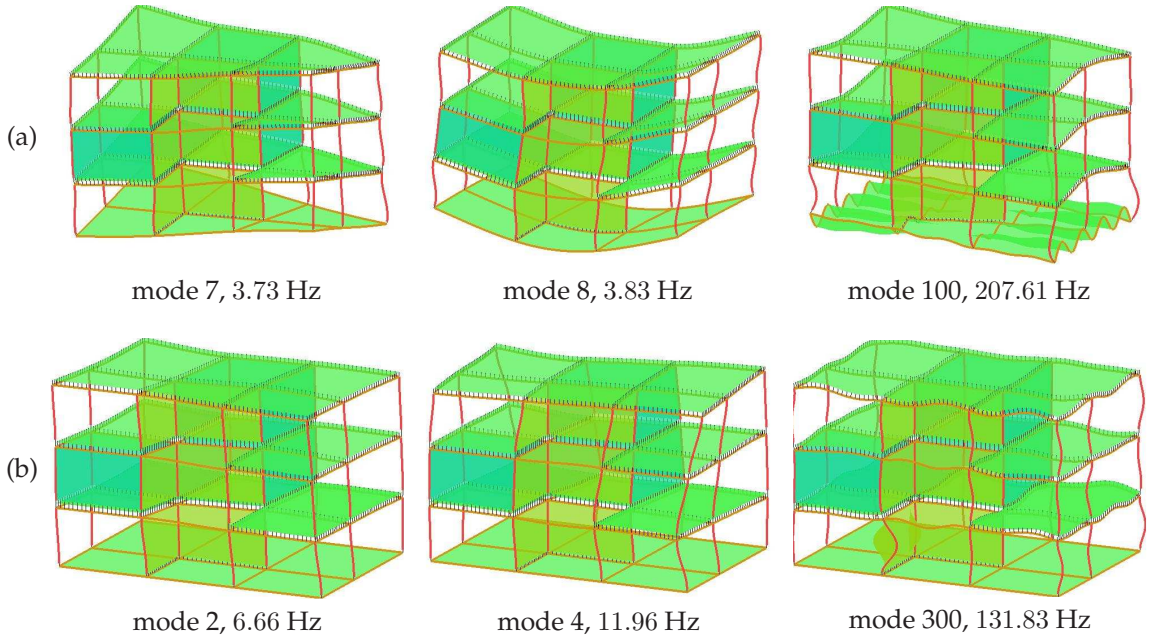

Figure 6.5: (a) Quasi-static transmission of flexible foundation modes on the superstructure and (b) flexible modes of the superstructure with clamped foundation.

According to the Rubin criterion [Rub75], all the modes up to $1.5 f_{\max}$ have to be taken into account in the modal superposition in order to have a kinematic base that is sufficient up to a frequency of $f_{\max}$. In the present study, all the foundation and superstructure modes up to 300 Hz have been accounted for. A few modes are displayed in figure 6.5. The lowest mode of the superstructure with a clamped base is at 2.60 Hz, and only 12 modes of the superstructure have been found under 20 Hz. These low frequency modes are the global torsional and bending modes of the whole building. Above 50 Hz, however, the modal density tends to be very high and the high frequency modal shapes show local bending modes

of the floor slabs and the core walls. The number of superstructure and foundation modes increases linearly with frequency in the higher frequency range. The total number of superstructure and foundation modes that is accounted for is equal to 829 and 203, respectively.

6.3.3 The stiffness of the soil

For the computation of the soil's stiffness, the same foundation mesh as introduced in figure 6.4 has been used in a boundary element method based on the Green's functions of a layered half-space. Figure 6.6 shows the real and imaginary part $k(\omega)$ and $c(\omega)$ of the soil's stiffness $\hat{K}_g(\omega) = \hat{k}(\omega) + i\omega\hat{c}(\omega)$ corresponding to the vertical rigid body displacement of the foundation. The functions show that the real part decreases slowly, while the imaginary part increases linearly with frequency in the higher frequency domain. This means that, at higher frequencies, the radiation damping dominates the soil's stiffness.

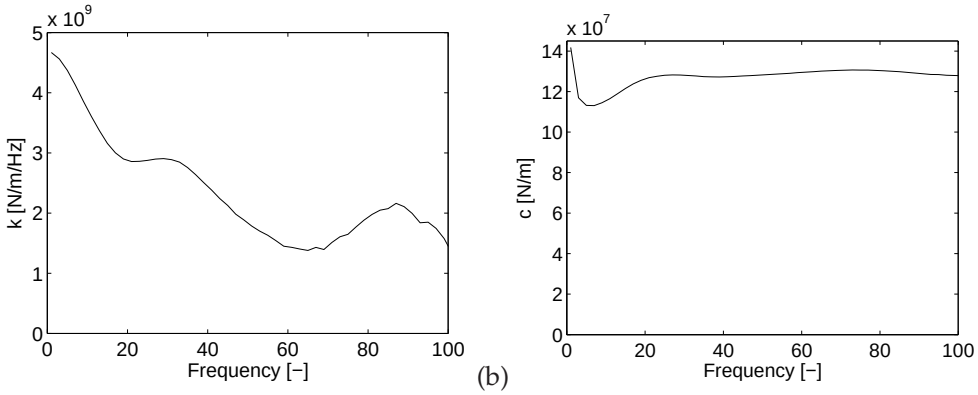

Figure 6.6: (a) Real and (b) imaginary part of the soil's stiffness corresponding to the vertical rigid body mode of the foundation.

6.3.4 Structural response

In the following, the structural response of the office building to the passage of the high-speed train is presented. Different modeling options are considered with respect to the effect of dynamic soil-structure interaction.

First, it is assumed that dynamic soil-structure interaction does not have a significant effect on the ground borne structural vibrations and re-radiated noise. This assumption is very attractive from a computational point of view, because the determination of the soil's stiffness with a 3D boundary element method can be avoided. Some assumptions have to be made, however, regarding the impedance difference between the soil and the foundation or the waveform of the incident wave field.

- If the incident wave field is uniform, then it can be assumed that only rigid body modes of the foundation are excited by the incident wave field. Furthermore, it is assumed that no SSI occurs. The modal coordinates $\mathbf{u}_0$ can be determined by using equation (3.31), where only the six rigid body foundation modes are incorporated in $\mathbf{\Phi}_f$.
- If the soil is much stiffer than the structure, it can be assumed that the incident wave field is not affected by the structure, and the structure's foundation can be directly

excited with the incident soil displacements. The modal coordinates $\boldsymbol{\alpha}_f$ of the foundation can be obtained by a least mean squares approximation of the incident wave field, using a superposition of the rigid and flexible foundation modes $\boldsymbol{\Phi}_f$, as given in equation (3.31).

- In the third modeling case, dynamic soil-structure interaction is accounted for with the assumption of a flexible foundation. The soil's stiffness and the loading forces are computed with the boundary element method and equation (3.28) is solved.

Figure 6.7 displays the vertical velocity in two points Q1 and Q2 of the building for the three modeling cases. The point Q1 is located on the ground level and Q2 is located on the floor of room 1, both at horizontal coordinates $x = 20.5$ m and $y = 2$ m.

For the case of the rigid foundation without dynamic soil-structure interaction (figure 6.7a), only very small vertical vibration levels are observed on the foundation (point Q1). This is due to the fact that the rigid body motion of the foundation results in a suppression of the horizontally propagating ground vibrations above 20 Hz, as their wavelength is smaller than the foundation's dimension in the x direction. However, a significant vibration amplification can be observed between the foundation (point Q1) and the first floor (point Q2) due to the first local bending modes of the floor slab in the frequency range between 20 Hz and 30 Hz.

As the dominant frequency range of soil vibrations is above 20 Hz, the assumption of a flexible foundation results in much larger vibration levels on the foundation (figures 6.7b and 6.7c). The vertical vibrations are strongly amplified at the local bending modes of the slabs at the first floor. The ground vibrations above 50 Hz are not transmitted up to the first floor, which is an effect of structural damping. Comparing figures 6.7b and 6.7c, the effect of dynamic soil-structure interaction on the structure with a flexible foundation can be investigated. As the soil is rather stiff, the vibration levels are similar for both cases. Soil structure interaction results in an attenuation of the incident wave field in the higher frequency range (above 50 Hz). It can be concluded that, in the present case, the effect of dynamic soil-structure interaction can be disregarded in good approximation, if the imposed wave field on the structure incorporating the flexible foundation is properly represented, according to equation (3.31).

6.4 Acoustic response

6.4.1 Acoustic properties

The dimensions of room 1 and room 2 are 5 m $\times$ 6 m $\times$ 2.8 m, while the size of room 3 is 5 m $\times$ 4 m $\times$ 2.8 m.

The sound velocity is equal to $c = 343$ m/s and the density of the air is $\rho_0 = 1.225$ kg/m^3. The absorption is assumed to be constant on the rooms' surface and over the whole frequency range. Two different absorption coefficients are considered for the three rooms: $\alpha = 0.03$ stands for a strongly reflecting room with uncovered concrete walls and an uncarpeted floor, while $\alpha = 0.15$ is typical for an unfurnished, carpeted room [MH94] [Har91]. Using Sabine's formula [Sab93], the reverberation time t_{rev} can be approximated from the room's volume V, the surface area A and the average absorption coefficient α as:

$$t_{\text{rev}} = \gamma \frac{V}{\alpha A}, \tag{6.4}$$

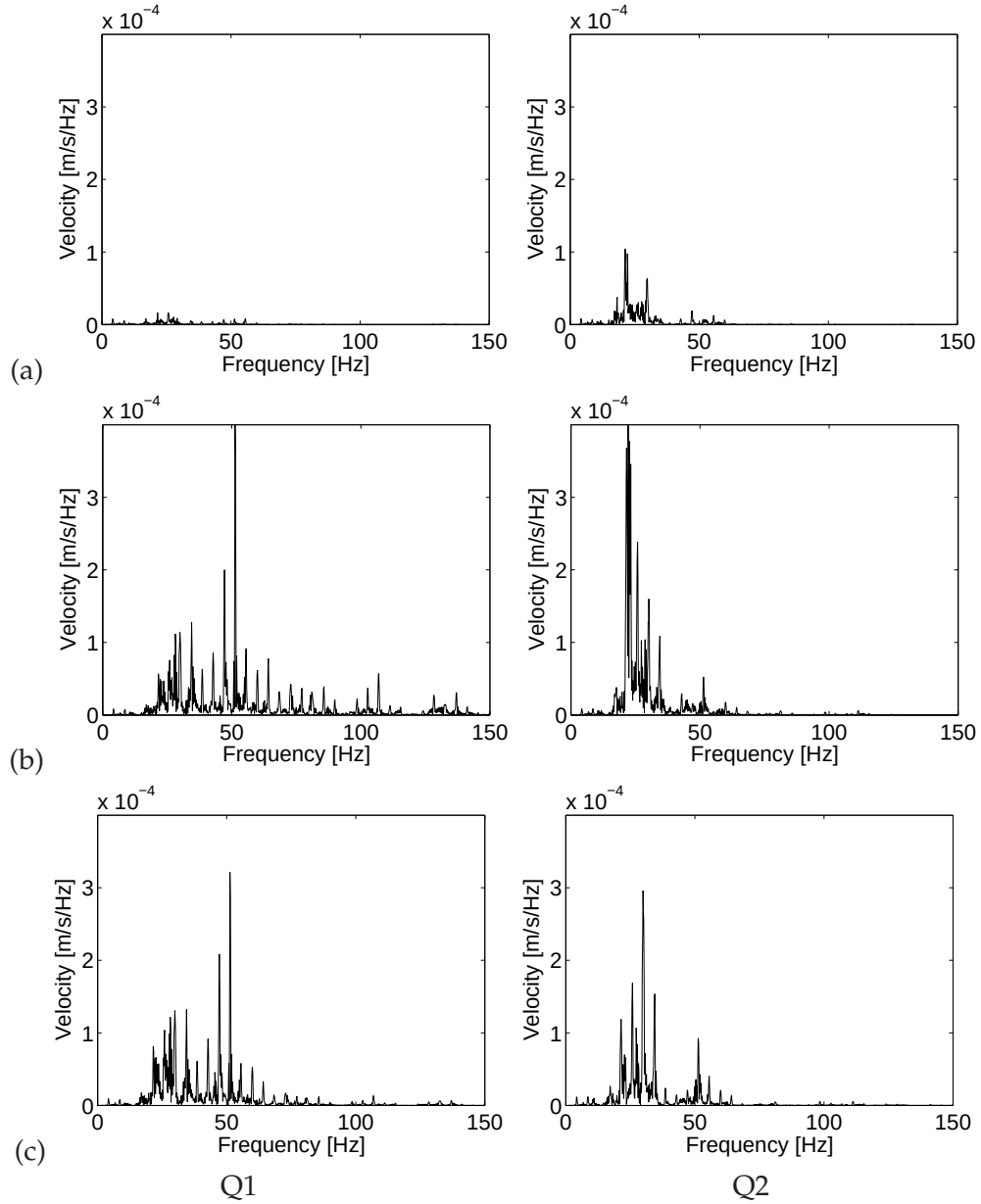

Figure 6.7: Frequency content of the vertical velocity in the points Q1 and Q2 for the case of (a) a rigid foundation without dynamic SSI, (b) a flexible foundation without SSI and (c) a flexible foundation with SSI.

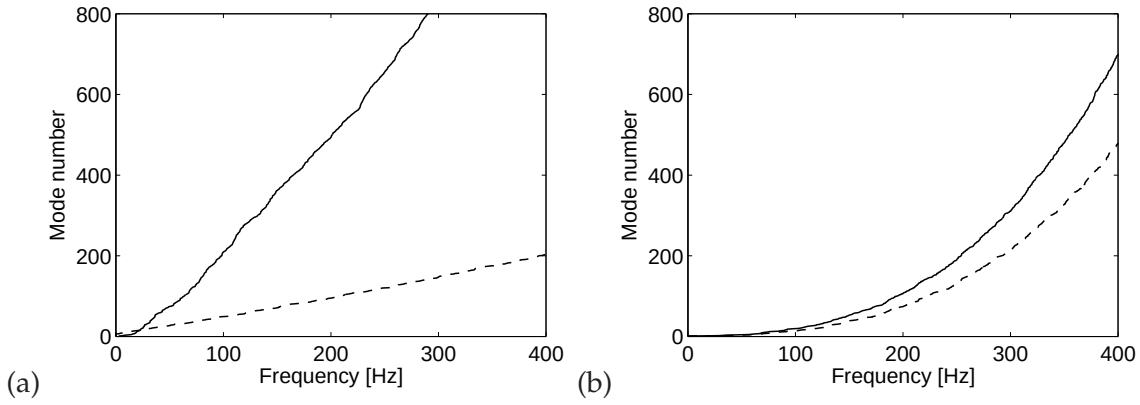

Figure 6.8: Number of (a) structural modes as a function of the upper frequency limit for the foundation (dashed line) and the superstructure (solid line) and (b) number of acoustic modes for room 1 (solid line) and room 3 (dashed line).

where $\gamma = 0.16$ s/m. For the case of the larger rooms (room 1 and room 2), the absorption coefficients $\alpha = 0.03$ and $\alpha = 0.15$ result in reverberation times of 3.3 s and 0.66 s, respectively, while for the case of the smaller room 3 these reverberation times are 3.68 s and 0.73 s.

6.4.2 Acoustic modes

The computational effort of the structural and acoustic computations is determined by the number of modes taken into account in the modal superposition. A modal base including all the acoustic modes up to 400 Hz has been used for the spectral finite element method. Figure 6.8 plots the number of structural and acoustic modes as a function of frequency. In the lower frequency range, the structural modal density is much higher than the acoustic. However, the number of structural modes increases linearly with frequency while the acoustic modal density increases more rapidly. With an upper frequency limit of 200 Hz, the computational times for determining the structural response and the acoustic response in a single room are of the same order of magnitude.

Referring to the frequency range of structural vibrations on the first floor, it is clear that the dominant frequencies of the acoustic response will be determined by the first few acoustic modes. The eigenfrequencies and modal numbers of these modes are listed in table 6.1.

6.4.3 Transfer functions

In the following, transfer functions are presented which relate the sound pressure in an internal point of room 1 to the vertical rigid body motion of the foundation. The point Q3 is located at $x = 20$ m, $y = 1.4$ m, $z = 4.32$ m, slightly shifted from the center of room 1 in order to find the contribution of as many modes as possible.

Figure 6.9 shows the transfer functions in the time and the frequency domain, for the case of all the absorption coefficients. These transfer functions can be used to give an estimate of the ground borne noise level in the building, if the velocity of the incident wave field is known. The frequency domain functions show a constant trend above 50 Hz. This implies that the dominant frequency range of re-radiated sound does not differ from the

Table 6.1: Mode numbers and frequencies of the first acoustic modes of room 1.

(a)

f [Hz]	n_x	n_y	n_z
28.58	0	1	0
34.30	1	0	0
44.64	1	1	0
57.16	0	2	0
61.25	0	0	1
66.66	1	2	0
67.59	0	1	1
68.60	2	0	0
70.20	1	0	1

(b)

f [Hz]	n_x	n_y	n_z
34.30	1	0	0
42.87	0	1	0
54.90	1	1	0
61.25	0	0	1
68.60	2	0	0
70.20	1	0	1
74.76	0	1	1
80.90	2	1	0
82.25	1	1	1

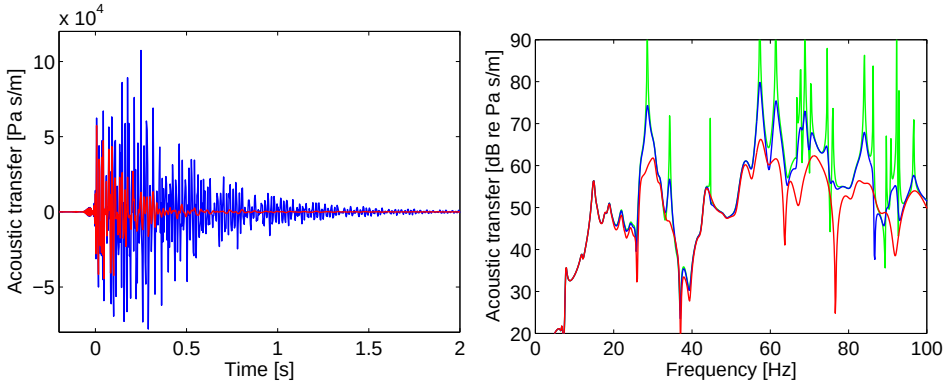

Figure 6.9: Transfer function between the vertical velocity of the rigid foundation and the sound pressure in room 1 for $\alpha = 0.00$ (green), $\alpha = 0.03$ (blue) and $\alpha = 0.15$ (red).

frequency range of the incident velocity. The first sharp peak in the frequency content appears around 30 Hz. At this frequency, the first bending modes of the room's walls excite the first horizontal acoustic modes of the room. The maximum level of the frequency content is at the first vertical acoustic resonance. Above this frequency, a lot of very sharp peaks are found corresponding to lower absorption. For the case of $\alpha = 0.15$, these peaks are damped by approximately 10 dB. Time histories of the transfer function are obtained by applying an inverse FFT and reveal good correspondence with the reverberation times predicted by Sabine's formula.

6.4.4 Acoustic response to high-speed train excitation

Figure 6.10 displays the time history and the one-third octave band spectra of the sound pressure in room 1, induced by the passage of the high-speed train. The figure shows the response for the lower absorption coefficients $\alpha = 0.03$, and for all the three modeling cases. For the case of the rigid foundation without dynamic soil-structure interaction, only the first horizontal acoustic modes are excited, resulting in a sound pressure level of 70 dB in the 25 Hz and 31 Hz bands. For the case of the flexible foundation, the dominant one-third octave bands are those containing the room's resonance frequencies at 28.6 Hz (mode (1,0,0)),

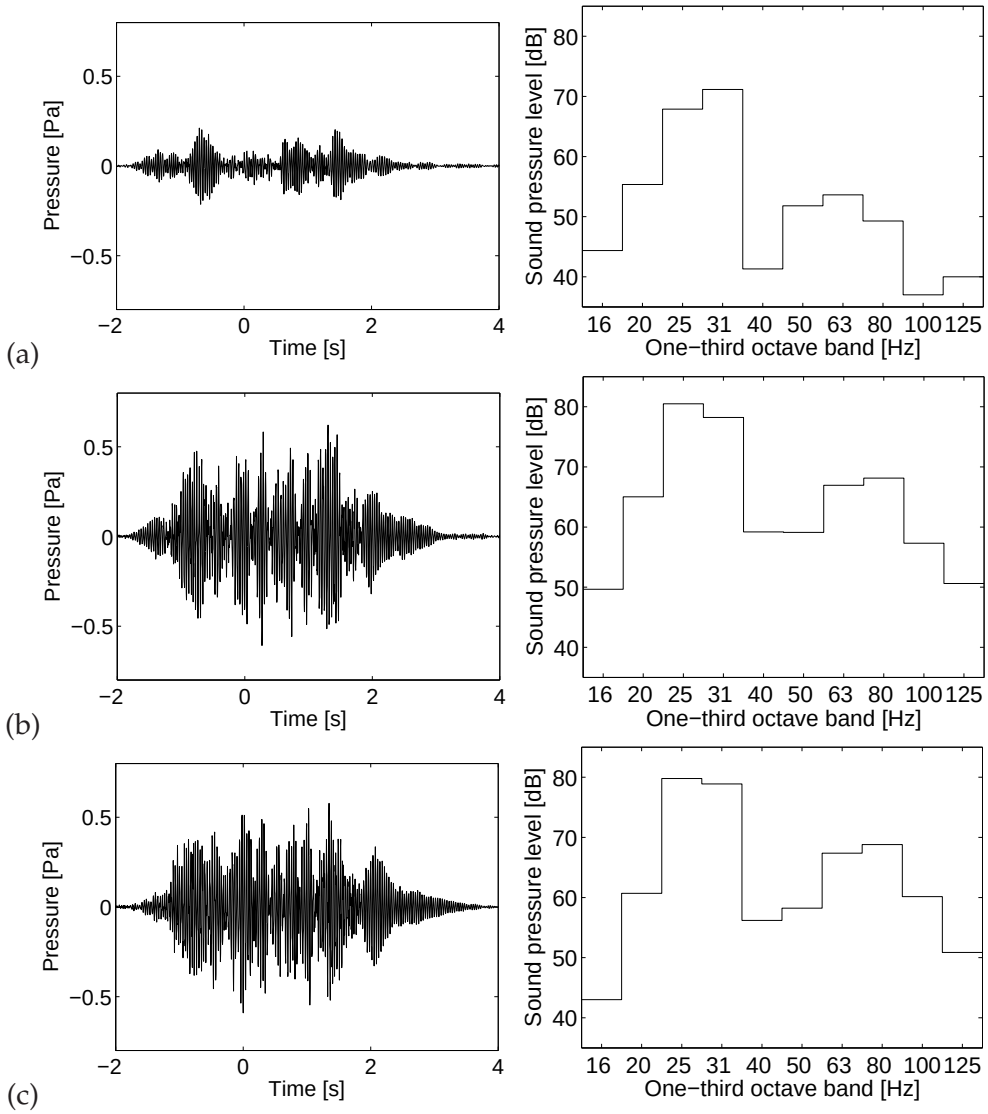

Figure 6.10: Time history and one-third octave band levels of the sound pressure in room 1 during the passage of a HST for the case of $\alpha = 0.03$ and for (a) a rigid foundation without dynamic SSI, (b) a flexible foundation without dynamic SSI and (c) a flexible foundation with dynamic SSI.

34.3 Hz (mode (0,1,0)), 57.2 Hz (mode (2,0,0)), 61.25 Hz (mode (0,0,1)) and 68.6 Hz (mode (0,2,0)). The maximum level is found in the 25 Hz band. Due to the frequency dependent sensitivity of the human ear, the observed noise is determined by the 63 Hz and 80 Hz band peaks. Comparing figures 6.10b and 6.10c, it can be found that dynamic soil-structure interaction has a negligible effect on the re-radiated noise.

Figure 6.11 shows the sound pressure in room 1 to the passage of the high-speed train for the two absorption coefficients. The one-third octave band spectra show a difference of 5 dB between the two wall absorptions above the first acoustic resonance of the room. In the time histories, the difference in reverberation time is clearly visible.

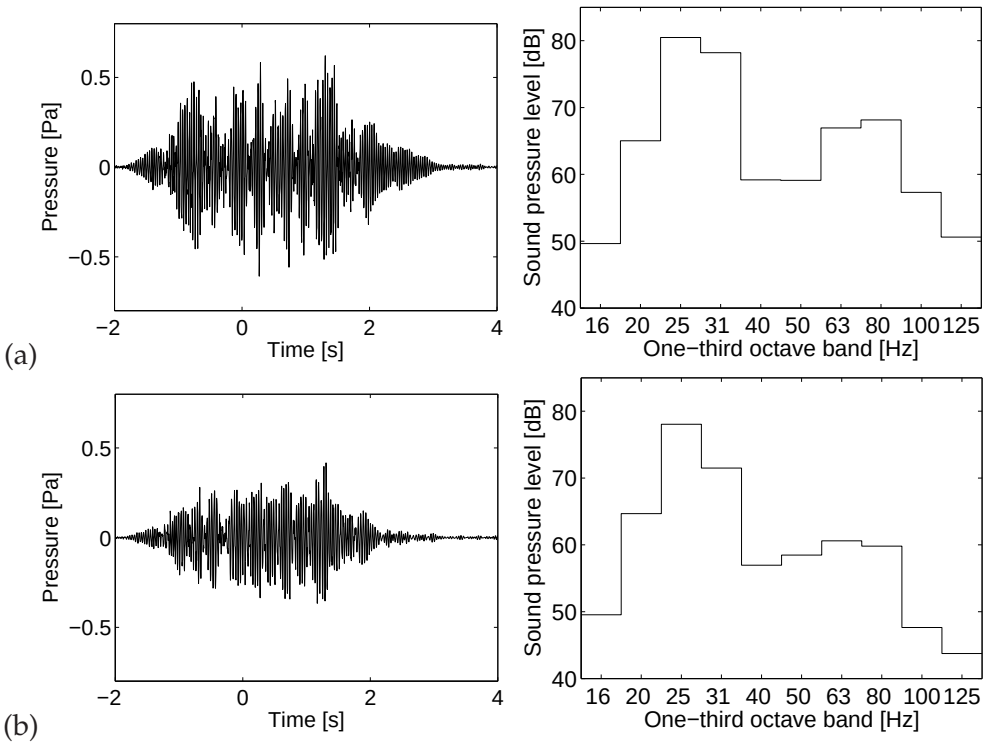

Figure 6.11: Time history and one-third octave band levels of the sound pressure in room 1 during the passage of the high-speed train for the case of a flexible foundation without dynamic SSI, with (a) $\alpha = 0.03$ and (b) $\alpha = 0.15$.

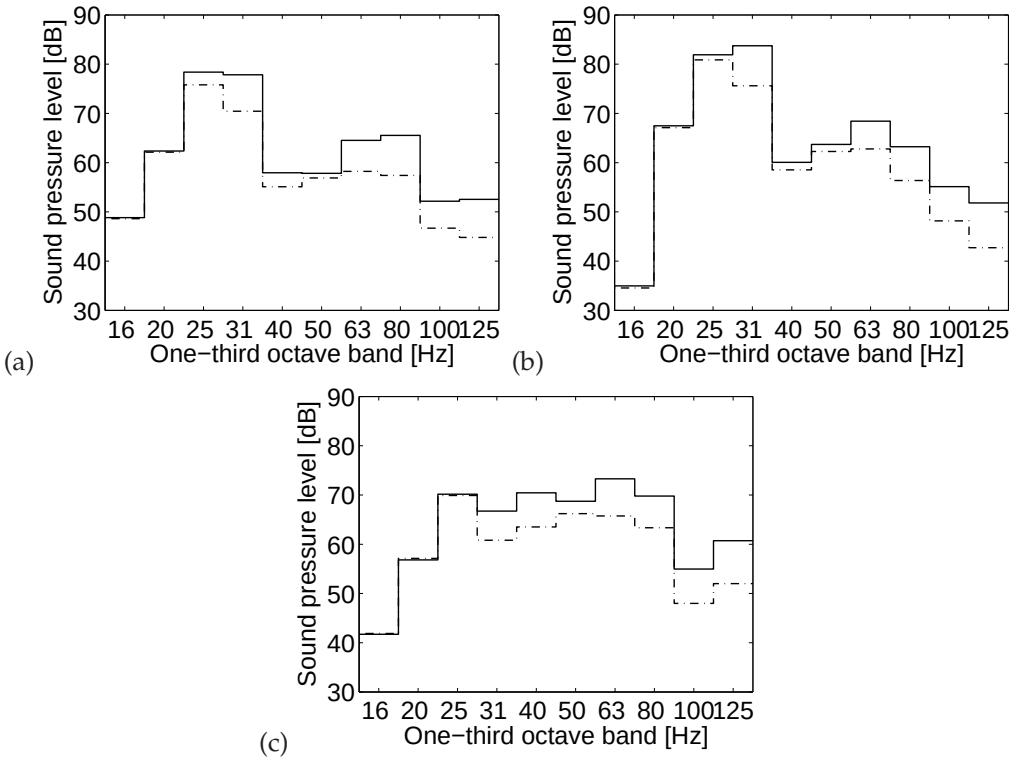

Figure 6.12: One-third octave band spectra of the sound pressure in (a) room 1, (b) room 2 and (c) room 3 to the passage of the high-speed train for the case of $\alpha = 0.03$ (solid line) and $\alpha = 0.15$ (dash-dotted line).

6.4.5 Response to high-speed train excitation in different rooms of the building

The sound pressure levels in the three rooms due to the passage of the high-speed train are compared in figure 6.12 for the case where dynamic soil-structure interaction is not accounted for and the foundation is assumed to be flexible. Comparing the pressure levels in rooms 1 and 2 that are of the same dimensions but at different levels of the building, a slight amplification at the first two horizontal modes can be observed. Figure 6.12c corresponds to room 3 that is on the first story but has different dimensions than room 1. As the first eigenfrequencies of this room (at 34.3 Hz, 42.85 Hz and 61.3 Hz) are distributed uniformly in the frequency scale, the one-third octave band spectra are balanced between 25 Hz and 80 Hz.

6.5 Vibration and noise isolation

The described methodology has been used to investigate the effectiveness of vibration and noise isolation methods. The first method is the insertion of a floating floor in the room (figure 6.13a) in order to isolate the vibrations of the floor slab from the room's interior floor. The second method, widely used in acoustic laboratories for both vibration and noise reduction purposes, is a box-within-box arrangement, where the whole interior boundary is isolated from the vibrations of the building's walls and slabs. (figure 6.13b). The third,

most practical application is the base isolation of the building, where the superstructure is isolated from the foundation by springs placed under the columns and the core walls on the basement level.

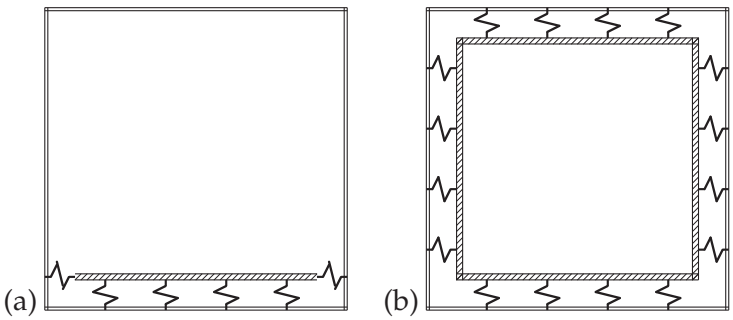

Figure 6.13: Vibration and noise isolation of the room's interior by means of (a) a floating floor and (b) a box-within-box arrangement.

For the case of the floating floor, a concrete floor supported by discrete springs and isolated from the walls by resilient material has been investigated. The 10 cm wide concrete slab is modeled by 4-node shell elements. The springs are placed at a distance of 1 m from each other. Their stiffness has been determined so that the total stiffness of the support and the mass of the concrete slab result in a vertical resonance frequency of 10 Hz. The elastic material that horizontally isolates the floating floor from the walls has been modeled by springs chosen to give a horizontal resonance frequency of 8 Hz.

For the case of the box-within-box arrangement, the internal box consists of a 10 cm wide concrete floor slab and 6 cm wide concrete walls isolated by a resilient material. For the sake of simplicity, this material is modeled by a continuous spring-damper system, where the springs are connected to each node of the shell elements representing the floor and the walls. Similarly, the ceiling is modeled as a 6 cm thick wooden slab and a resilient material. Just as for the floating floor, the vertical and horizontal resonance frequencies have been chosen to 10 Hz and 8 Hz, respectively.

For the case of the base-isolated building, 9 springs of equal stiffness k_z have been inserted below the structure's columns which are separated from the central core, and a distributed spring of total stiffness $3k_z$ has been inserted under the core. The stiffness k_z has been determined so that the vertical resonance frequency of the building on the springs is equal to 5 Hz.

As the office superstructure is modified, the superstructure modes and the quasi-static transmission of the foundation modes have been recomputed. Figure 6.14 shows some modes of the base-isolated structure. Figure 6.14a shows the quasi-static transmission of the foundation modes, resulting in smaller modal displacements of the superstructure, due to the base isolation. Figure 6.14b shows some low frequency modes of the base-isolated superstructure on a clamped foundation. These modes show rigid body motions of the original superstructure on the springs. Although the vertical resonance of the structure has been planned to 5 Hz, the actual resonance frequency of 4.60 Hz is somewhat lower. This difference can be explained with the unbalanced support of the isolated structure. In the model, the supporting stiffness is distributed uniformly under the superstructure, while the mass of the superstructure is not uniformly distributed.

For the case of the floating floor and the box-within-box arrangement, where the internal

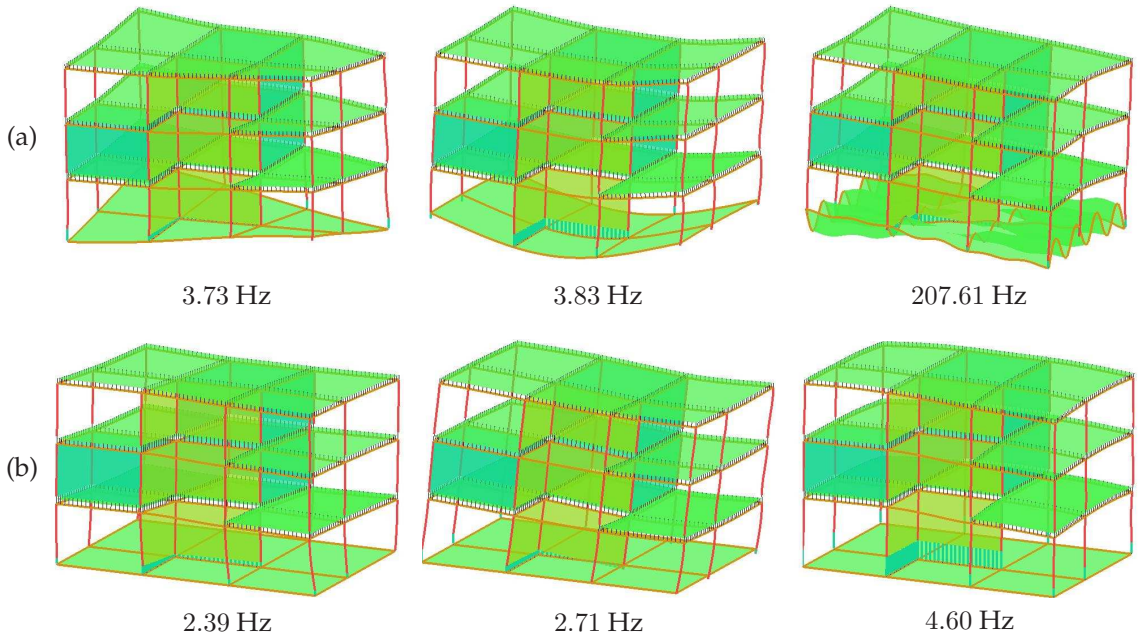

Figure 6.14: (a) Quasi-static transmission of flexible foundation modes on the base-isolated superstructure and (b) flexible modes of the base-isolated superstructure with clamped foundation.

volume of the acoustic space is modified, the acoustic computations have to be performed with the new modal base. However, as the Craig-Bampton method is used, the expensive computation of the soil's stiffness and the forces does not need to be repeated.

Figure 6.15 shows the effect of the vibration isolation methods on the sound pressure in room 1, for the case of the wall absorption $\alpha = 0.03$. The floating slab, where only reduces the noise radiation by the room's floor, does not result in significant noise reduction. The box-within-box arrangement is very effective, as it results in an average noise reduction of 10 dB for the total frequency range. The most effective solution is the base isolation of the superstructure, where the noise reduction is about 20 dB in the higher frequency range.

6.6 Conclusions

A numerical model has been presented that is capable to predict surface traffic induced vibrations and re-radiated sound in buildings, accounting for a moving vibration source, vibration propagation in a layered ground, dynamic soil-structure interaction and sound radiation into acoustic enclosures.

A numerical example has been used to demonstrate the use of the methods. The structural and acoustic response of a three-story portal frame office building has been calculated up to the frequency limit of 150 Hz.

It has been shown that, for the case of a relative stiff soil with a shear wave velocity of $c_S = 250$ m/s, the disregarding of dynamic soil-structure interaction effect and a direct excitation of the flexible foundation gives a good approximation of both the structural vibrations levels and the re-radiated sound with reasonable computational effort. The dominant fre-

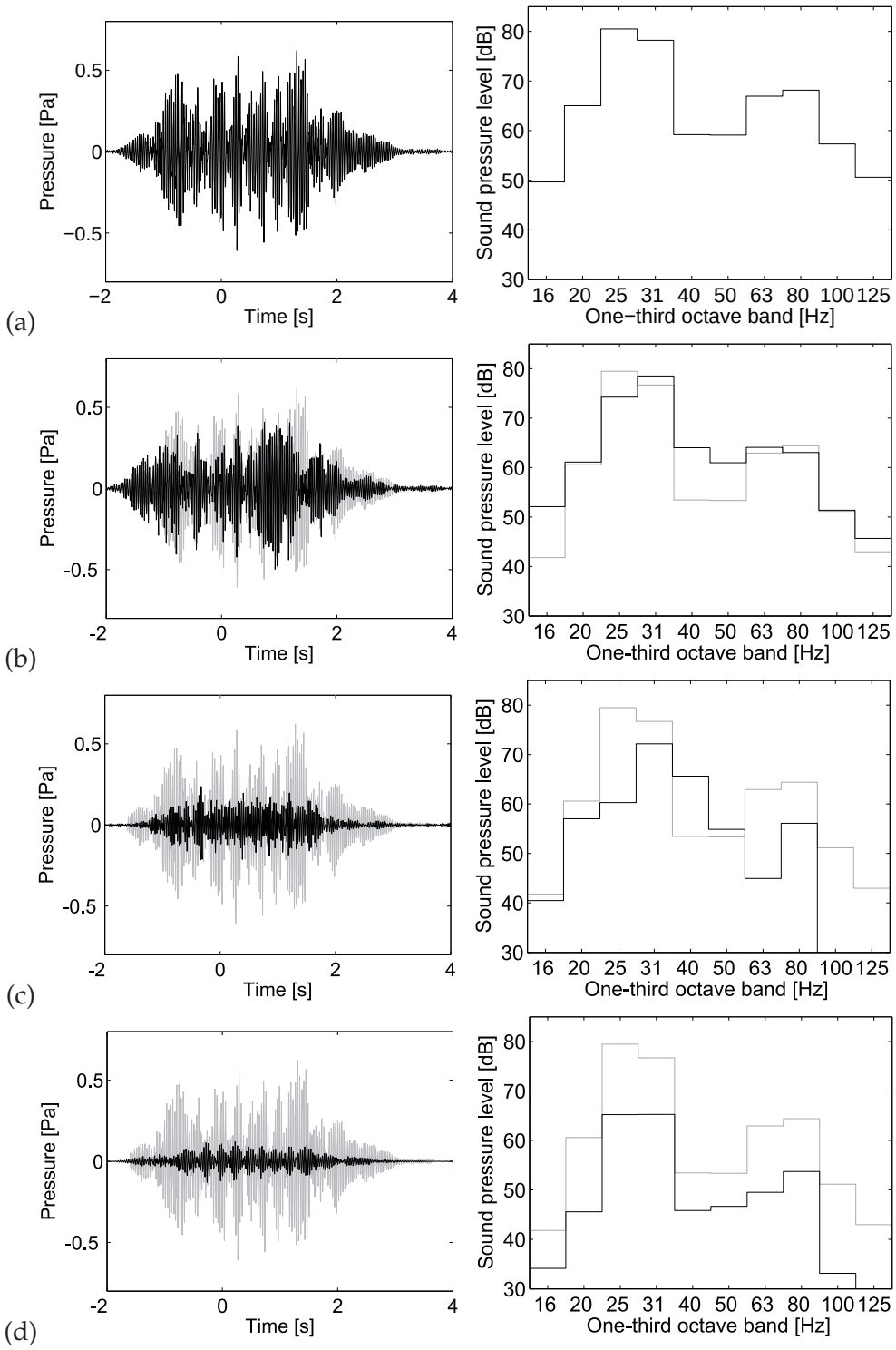

Figure 6.15: Time history and one-third octave band spectra of the sound pressure in room 1 during the passage of a HST for the case of $\alpha = 0.03$ and (a) no vibration isolation, (b) a floating floor, (c) a box-within-box arrangement and (d) base isolation. The unisolated case is displayed with grey line.

quencies of the traffic induced acoustic response are basically determined by the first acoustic resonances of the room. The effect of wall absorption on the sound pressure has been investigated, and above the first acoustic resonance, a difference of 5 dB has been found between typical wall absorptions for concrete and carpeted walls. The room dimensions are found to importantly effect the sound pressure level.

The use of the developed methodology has been demonstrated by modeling different noise-isolation methods. The base isolation of the building has been found as the most effective solution for noise isolation.

Chapter 7

Practical application

7.1 Introduction

As a practical application, the described methodology has been used to determine the vibration specifications of the new Budapest underground line m4.

The construction works of the new line m4 have started in the end of 2006. At the moment when the present thesis is submitted, the tunnel of the new line is being drilled and simultaneously, the concrete tunnel wall is being constructed. In the following months, the structural planning of the railway track system will be finalized.

The tunnel of the line m4 is a deep-bored tunnel. Its length is 7300 m, and the total line contains 10 surface-cut stations. The tunnel depth varies between $30\ \mathrm{m}$ and $5\ \mathrm{m}$, the deepest parts run under the Danube. Due to small depth of the tunnel, significant ground-borne noise and vibration is expected in existing nearby buildings. Therefore, the planning of the vibration isolation system is carried out with special attention to the noise and vibration problem.

The Laboratory of Acoustics at the Department of Telecommunications of the Budapest University of Technology and Economics took part in the design of the vibration isolation system, and the methodology described in the present thesis has been applied in the planning. The task of the Laboratory was to define the vibration specifications at the railway tunnel. This specification means that the maximal allowed tunnel vibration velocity has been determined in such a way that the ground-borne vibration and noise in nearby buildings do not exceed the limits given by the Hungarian standards.

The definition of the tunnel vibration specification has been carried out in the following steps:

- First, a measurement campaign has been organised. The aim of the measurements was threefold.

    1. The material and geometrical properties of the soil has been measured in three locations in Budapest by means of a Spectral Analysis of Surface Waves method. These parameters are essential input of the numerical model.
    2. Transfer functions have been measured between the tunnel of the existing underground lines m2 and m3 and nearby buildings. These measurements have been used for validation purposes.

3. The typical vibration velocity of the tunnel's wall has been recorded in the tunnel of the lines m2 and m3 during the passage of metro trains.

- In a second step, the coupled numerical model has been validated, using the transfer functions measured at the lines m2 and m3. During the validation, the coupled numerical model has been used to compute the vibration transfer between the tunnel's wall and the surrounding buildings, and these results have been compared to the measured transfer functions.

- In a last step, the validated numerical model has been used to compute the transfer between the tunnel of the line m4 and nearby buildings. These transfer functions were used to maximize the vibration velocity of the tunnel wall.

7.2 Determination of dynamic soil properties

The determination of the dynamic soil properties have been carried out in three locations in Budapest. The first location is in Buda, at the Kelenföld City Center, the second location is in Buda, at the Hamzsabégi street, and the third location is in Pest, in the garden of the Hungarian National Museum. In the following, the measurements at the first location are described in details.

7.2.1 The concept of the measurement

The measurements have been carried out by means of the SASW (Spectral Analysis of Surface Waves) method that is based on the disperse behavior of the surface waves in a layered half space. Using the method, the soil profile of a layered half space is determined by measuring the frequency dependent propagation velocity of the surface wave, and searching for a soil profile that yields a similar disperse behavior.

7.2.2 The measurement setup

The measurement scheme is displayed in figure 7.1. The surface waves are excited by a vertical impulsive load $F(t)$ acting on the surface of the layered half space. The acceleration time histories $a^{(i)}(t)$ are measured in several locations at the surface. The frequency dependent propagation velocity of the surface wave is determined by spectrally analyzing the acceleration signals of the adjacent sensor pairs.

Figure C.1 displays the location of the measurements carried out in the Kelenföld City Center at 1. November 2006. The measurement setup is displayed in figure C.2. The vertical impulse was excited by a $80\ \mathrm{kg}$ heavy bag filled with lead shot, falling down to a rubber mat from a height of $1.5\ \mathrm{m}$. The acceleration of the ground surface was measured with acceleration sensors mounted on steel pikes. The location and sensitivity of the acceleration sensors are given in table C.1.

The measured time histories are displayed in figure 7.2.2. Figure 7.2.2a shows the signal measured at a distance of 1 m from the source. Here, a sharp impulse appears at $t = 0\ \mathrm{s}$. The width of the impulse is approximately 0.03 s. The amplitude of the peak attenuates rapidly, as the distance from the source increases. This is a joint effect of the geometrical and material damping. The width of the impulse increases with distance. This is due to the

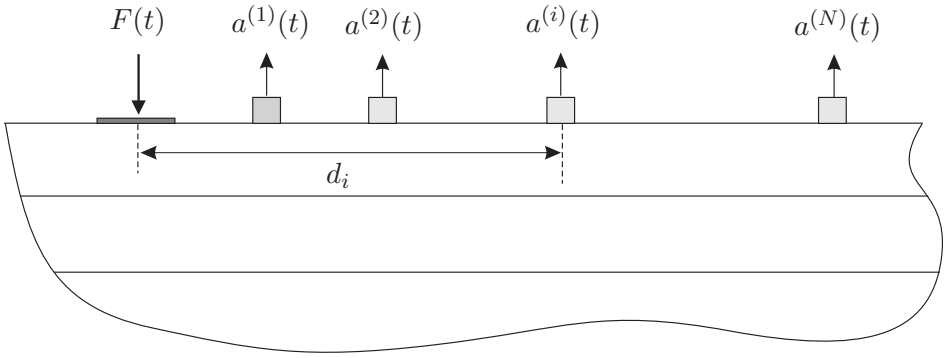

Figure 7.1: The scheme of the SASW measurement

disperse behavior of the surface wave: The small frequency components propagate faster than the high frequency components.

7.2.3 Spectral analysis

During the spectral analysis, the frequency content $\hat{a}^{(i)}(\omega)$ of the acceleration signals is computed by means of an FFT, and these frequency content functions are used to calculate the averaged cross power spectra $G_{ij}(\omega)$ of the adjacent sensor pairs:

$$G_{ij}(\omega) = \frac{1}{N_{ij}} \sum_{n=1}^{N_{ij}} \hat{a}_n^{(i)}(\omega)\ \hat{a}_n^{(j)\,*}(\omega) \tag{7.1}$$

Here, a star denotes the complex conjugate, and N_{ij} denotes the number of measurements where the i-th and j-th sensors were active.

The computed cross power spectra are displayed in figure 7.3, for the sake of clarity, only for the first three sensor pairs. According to the magnitude graphs, the falling weight excites vibrations above 10 Hz. The dominant frequency band is between 20 Hz and 180 Hz. The plot 7.3b shows the phase of the cross spectra, that is the phase difference between the adjacent sensors as a function of frequency. These curves start from zero and increase with frequency. In the case of non disperse propagation, these curves would increase linearly with frequency. The disperse behavior is expressed by the deviation from the linear curve.

The frequency dependent propagation velocity $v_{ij}(\omega)$ of the surface wave between the adjacent sensors is computed using the phase of the cross power spectrum $\arg(G(\omega))$ as

$$v_{ij}(\omega) = \frac{\omega(d_j - d_i)}{\arg(G_{ij}(\omega))} \tag{7.2}$$

The $v(\omega)$ total experimental dispersion curve of the layered half space was assembled from the $v_{ij}(\omega)$ dispersion curves, taking the following considerations: The velocity value at a frequency ω can be obtained from the signal of such a sensor pair

1. the receiver-to-receiver distance of which is small enough not to violate the spatial Nyquist criterion:

$$d_j - d_i < \frac{\pi v_{ij}(\omega)}{\omega}, \tag{7.3}$$

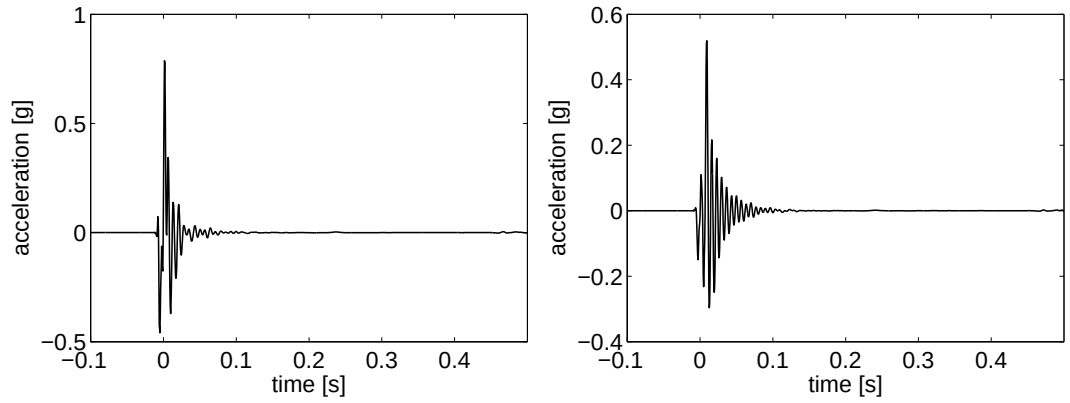

(a) $d = 1\,\mathrm{m}$

(b) $d = 2\,\mathrm{m}$

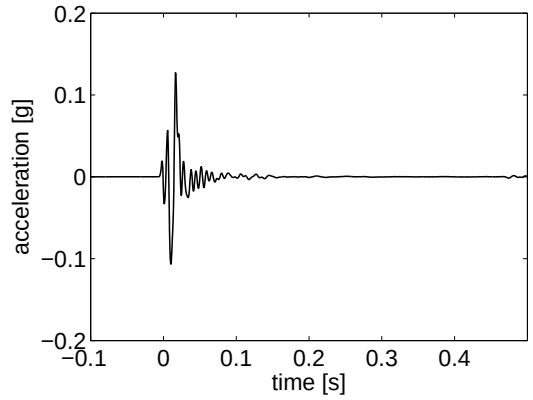

(c) $d = 4\,\mathrm{m}$

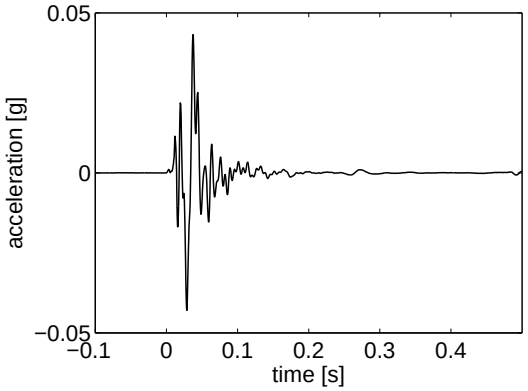

(d) $d = 8\,\mathrm{m}$

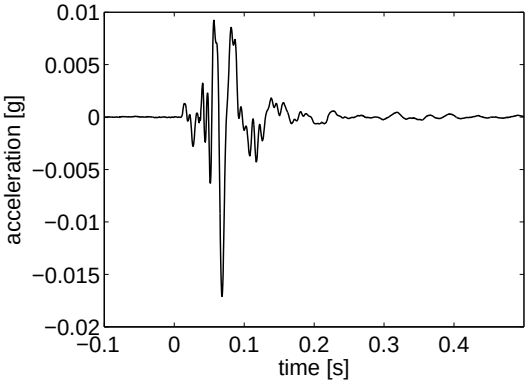

(e) $d = 16\,\mathrm{m}$

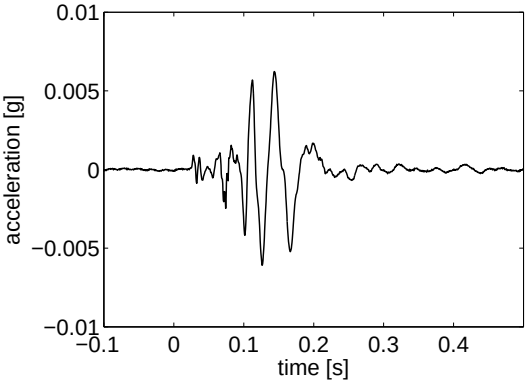

(f) $d = 25\,\mathrm{m}$

Figure 7.2: Acceleration time histories measured with the first six sensors

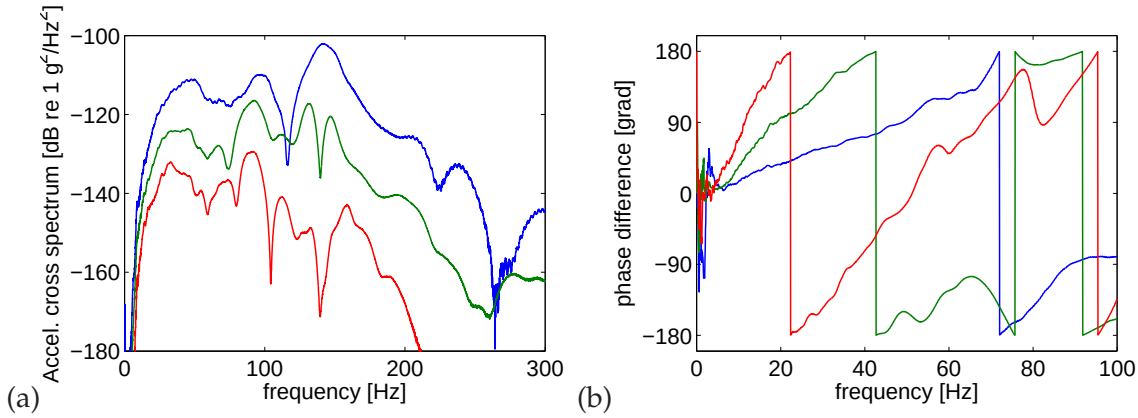

Figure 7.3: Magnitude (a) and phase (b) of the acceleration cross power spectra of adjacent sensors. (1 m-2 m – blue, 2 m-4 m – green, 4 m-8 m – red)

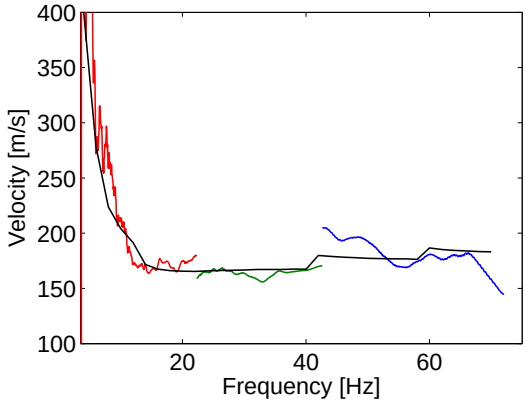

Figure 7.4: Measured dispersion curves in the Kelenföld City Center (1 m-2 m – blue, 2 m-4 m – green, 4 m-8 m – red), and the assembled experimental dispersion curve (black).

2. that are far enough from the source, so the Rayleigh surface waves dominate the response.

Not violating the Nyquist criterion practically means that the phase spectra in 7.3b are used below the first discontinuity (-2π jump). In order to hold the second criterion, the signal of a sensor pair is used only at those frequencies, where all of the other pairs with larger receiver-to-receiver distance violate the spatial Nyquist criterion.

As the cross spectra do not contain valuable components below 10 Hz, the phase curves are very noisy in this frequency range, and do not form a good base for velocity calculations. Hence, the dispersion curves have been determined over the frequency range $[10\text{ Hz}; 75\text{ Hz}]$.

The assembled experimental dispersion curve is plotted in figure 7.4. The curve starts at a phase velocity of 400 m/s at low frequencies, and this velocity decreases to 170 m/s at 15 Hz. This indicates that the stiffness of the ground increases with depth. The small frequency vibrations that reach the lower soil layers, propagate faster in the stiffer medium, while the high frequency vibrations propagate slower in the softer layers closer to the surface.

Table 7.1: Soil profile fitted in the Kelenföld City Center

	h [m]	c_S [m/s]	G [N/m^2]	ρ [kg/m^3]	β [$-$]	ν [$-$]
1. layer	2	200	$7.20 \cdot 10^7$	1800	0.025	1/3
2. layer	6	160	$5.37 \cdot 10^7$	2100	0.025	1/3
half space	∞	470	$5.08 \cdot 10^8$	2300	0.025	1/3

7.2.4 The inversion

During the inversion, a horizontally layered half space model is searched for in such a way that its theoretical dispersion curve is similar to the experimental dispersion curve in figure 7.4. As the Poisson's ratio and the material damping hardly affects the dispersion curve, their values have been set to $\nu = 1/3$ and $\beta = 0.025$, constant over the layers. Further, it has been assumed that the soil consists of two homogeneous layers lying on a homogeneous half space.

The inversion has been carried out using a multi-dimensional genetic optimizing algorithm. The variables of the optimization were the shear moduli and mass densities of the layers and the half space (2×3 variables), and the width of the two layers (2 variables). The theoretical dispersion curves have been computed by means of the Dynamic Stiffness Matrix method, described in chapter 2, and the mean square difference of the experimental and theoretical dispersion curves has been minimized. The resulting material properties are displayed in table 7.1.

7.3 Validation of the numerical model

The model validation has been performed by parallel measurements and computations along the existing underground lines m2 and m3. Three locations were chosen for validation purposes. Location 1 is near the station Kálvin square of the line m3, location 2 is near the station Blaha Lujza square of the line m2, and finally, location 3 is near the station Kossuth square of line m2. In the following, the validation at location 1 is discussed in details.

7.3.1 Site description

The site at the Kálvin square is shown in figure 7.5. The metro tunnel of line m3 runs in the direction SW-NE at a depth of 30 m below the surface, as shown in figure 7.5b. The metro station Kálvin tér is under the crossing of the Múzeum boulevard, the Vámház boulevard, the Múzeum street, the Baross street, the Üllői street and the Kecskeméti street.

The building of the Kálvin Center is at the crossing of the Múzeum street and the Baross street, as can be seen in figure 7.5b. This is is a 8-story concrete portal frame office building. The building has an embedded concrete box foundation with two basement levels. The photo of the building can be seen in figure C.3.

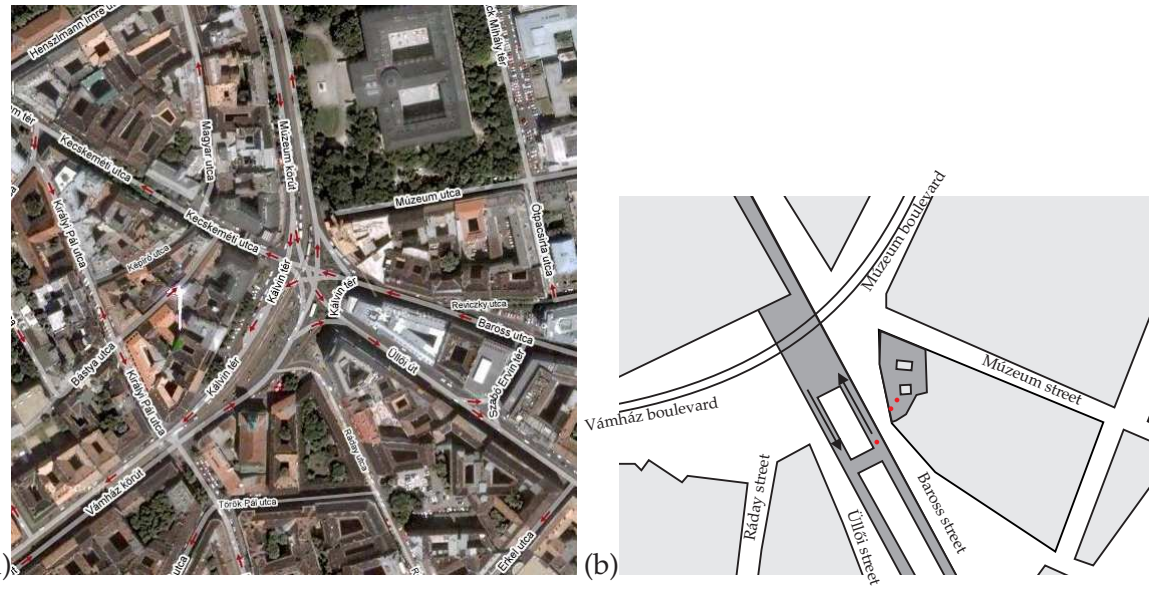

Figure 7.5: (a) The site at the Kálvin tér (b) The location of the metro tunnel m3 and the Kálvin Center

7.3.2 Measurements in the tunnel of line m3 and in the Kálvin Center

The measurements have been performed in the right track of the tunnel and in the basement of the Kálvin Center. The measurement locations are marked with red points in the figure C.3b. The vibration of the tunnel wall was measured using three acceleration sensors. One sensor measured the vertical vibration of the base plate of the tunnel, and two sensors measured the radial and tangential vibration of the tunnel's side wall, as shown in figure C.4.

Three accelerometers were placed in the building of the Kálvin Center. The sensors were located in the basement of the building. One accelerometer measured the vertical vibration of the base plate, while two accelerometers measured the horizontal and vertical vibrations of the side wall of the basement, as shown in figure C.4.

For the falling weight measurements, the falling weight introduced in section 7.2 was used. Figure 7.6 shows the frequency content of the acceleration measured in the tunnel and the building's basement. The curves describing the acceleration in the tunnel and in the building can be easily distinguished. The vibrations attenuate by 40-50 dB as they propagate from the tunnel to the building's basement. The simple and similar shape of the curves corresponding to the tunnel's vibration implies that only the first few modes of the tunnel's cross section are excited.

7.3.3 The numerical model

The numerical source model consists of a coupled longitudinally invariant finite element-boundary element model, where the finite element method is used to model the tunnel and the boundary element method is used to model the soil. The receiver model is a three-dimensional finite element model of the building.

The inner radius of the tunnel is 2.6 m, the outer radius is 3.1 m. The tunnel center

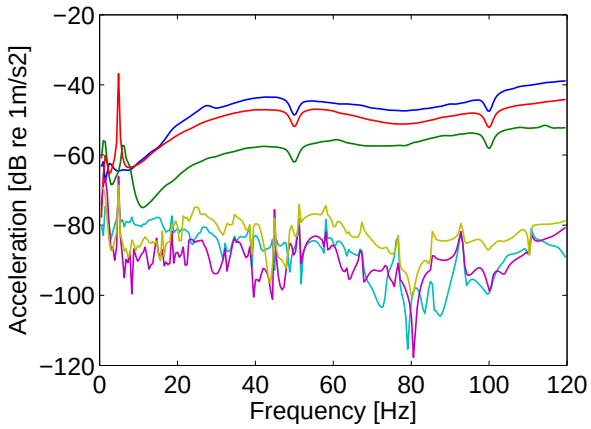

Figure 7.6: Frequency content of the measured acceleration of the tunnel and the building due to the falling weight excitation. Blue–tunnel base plate vertical, green–tunnel side wall radial, red–tunnel side wall tangential, yellow–building base mat vertical, cyan–building wall horizontal, magenta–building wall vertical.

Table 7.2: Soil properties measured in the garden of the Hungarian National Museum

	h [m]	c_S [m/s]	G [N/m^2]	ρ [kg/m^3]	β [−]	ν [−]
1. layer	2	200	$7.20 \cdot 10^7$	1800	0.025	1/3
2. layer	6	160	$5.37 \cdot 10^7$	2100	0.025	1/3
half space	∞	470	$5.08 \cdot 10^8$	2300	0.025	1/3

is located at a depth of 28.2 m. The tunnel's material is described by a mass density $\rho = 2300$ kg/m^3, a Young's modulus of $E = 2$ i10^{10} N/m^2, a Poisson's ratio $\nu = 0.16$ and a material damping ratio $\eta = 0.02$.

The soil is characterized by the material parameters determined during the SASW measurements in the garden of the Hungarian National Museum. This building is located between the Múzeum boulevard and the Múzeum street, as can be seen in figure 7.5. The soil parameters are given in Table 7.2.

The finite element mesh of the Kálvin Center is displayed in figure 7.7. The model contains the main structural elements of the building. These are the box foundation, the columns and beams of the portal frame structure, the slabs of the floors, the central cores that surround the elevators and the staircases and finally the concrete wall of a neighboring building. All these structural elements are made of reinforced concrete, their dimensions are displayed in table C.2.

The numerical model was used to compute the transfer function between the displacements of the tunnel's wall and the displacements in the building when an impulsive load is acting on the tunnel's base plate. During the computations, it has been assumed that only three low frequency modes of the tunnel's cross section are excited. These are (1) the rigid body vertical displacement of the tunnel, the (1) first vertical compressional mode of the tunnel and (3) the first horizontal compressional mode of the cross section. These modes are displayed in figure 7.8.

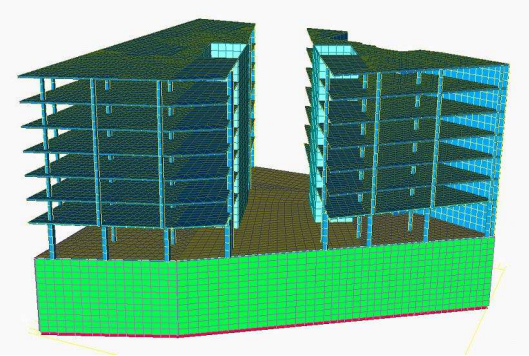

Figure 7.7: The finite element model of the Kálvin Center

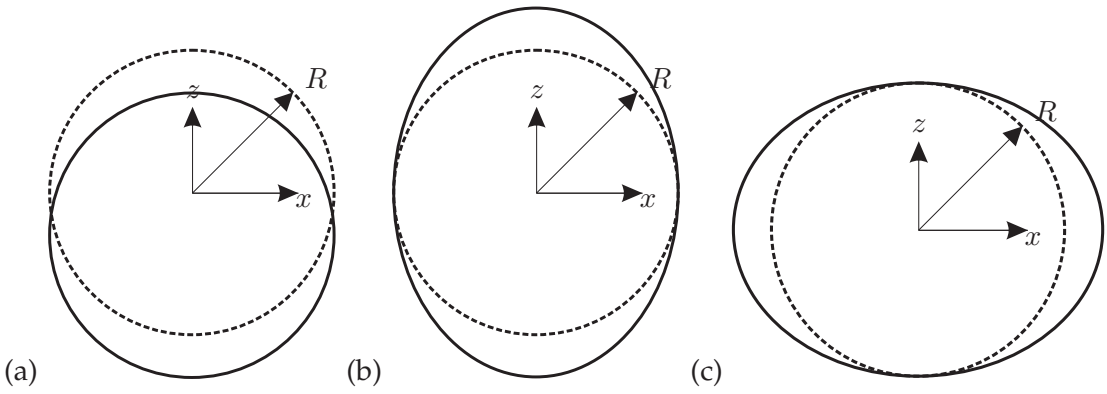

Figure 7.8: The three modes of the tunnel's cross section. (a) Vertical rigid body mode ($u_x = 0$, $u_z = 1$), (b) first vertical compressional mode ($u_x = 0$, $u_z = z$), (c) first horizontal compressional mode ($u_x = x$, $u_y = 0$).

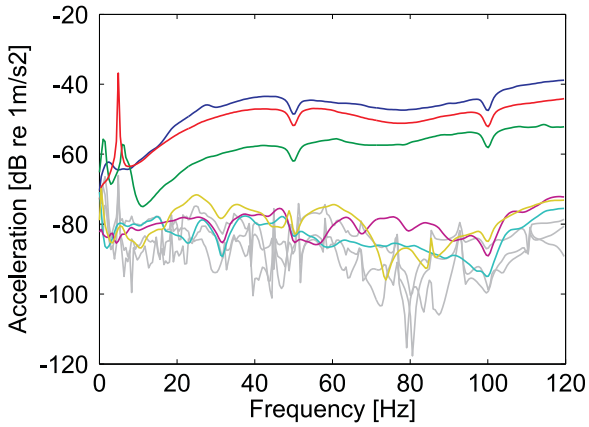

Figure 7.9: Frequency content of the computed acceleration of the tunnel and the building due to the falling weight excitation. Blue–tunnel base plate vertical, green–tunnel side wall radial, red–tunnel side wall tangential, yellow–building base mat vertical, cyan–building wall horizontal, magenta–building wall vertical.

As the impact force of the falling weight was not measured during the falling weight measurements and only the three displacement components were known from the testing, the frequency content of the loading force in the numerical model has been defined so that the computed tunnel accelerations do not differ from the measured tunnel response. In this phase, the frequency content of the x and z components of the loading force were considered as unknown parameters, and the difference between the measured and computed tunnel wall accelerations were minimized with a least mean squares algorithm.

Figure 7.9 shows the frequency content of the resulting accelerations in the tunnel and in the building's basement. It can be seen that the least means squares algorithm resulted in an almost perfect match between the measured and computed tunnel accelerations. The computed structural accelerations in the two points of the basement are also displayed in the figure. Comparing these values with the structural displacements in figure 7.6, it can be seen that the model computes the structural vibrations with a reasonable accuracy. The difference between the computed and measured results is about 5 dB.

7.4 Parametric study

After the model has been validated, a parametric study has been carried out in order to determine the vibration specifications for the new line m4. In the parametric study, a typical portal frame office building located above the metro tunnel has been modeled, and the re-radiated noise level in the rooms of the building due to the passage of a metro train has been computed. These computations have been carried out with different soil properties, different tunnel geometries and different tunnel-building distances. These parametric studies resulted in transfer functions between the vibration on the tunnel's base plate and the re-radiated noise in the building. With these transfer functions, the maximum allowable tunnel vibration levels could be determined so that the specified maximal sound pressure in the building's rooms is not exceeded.

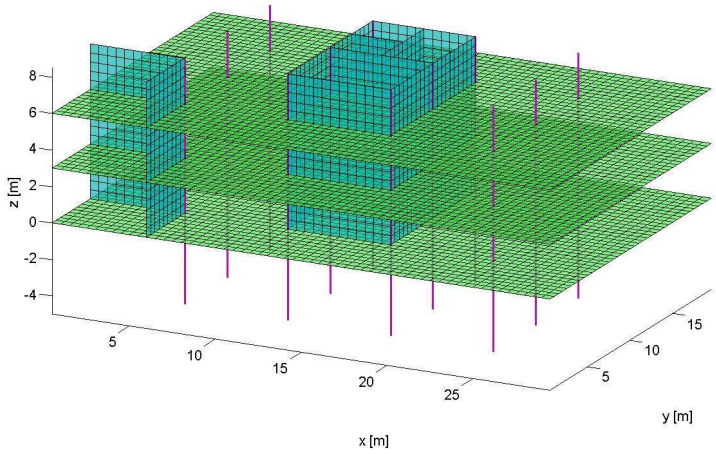

Figure 7.10: Finite element mesh of the portal frame office building. The external walls and the box foundation is not displayed in the figure.

7.4.1 The office building

The office building model used in the parametric study is displayed in figure 7.10. The dimensions of the building are 30 m $\times$ 20 m $\times$ 13.5 m. The structure is embedded in the soil to a depth of 4.5 m, and rests on a box foundation (not displayed in the figure). The box foundation is built of reinforced concrete of width 0.5 m. The building's floors are resting on columns with square cross section and width of 0.3 m. The reinforced concrete floors are modeled with 0.3 m wide plate elements. The in-fill walls of 15 rooms are taken into account in the model. The masonry in-fill walls of the rooms are modeled with 0.1 m wide plate elements. In each floor, there are two rooms of dimensions 5 m $\times$ 4 m $\times$ 3 m, one smaller room of dimensions 2.5 m $\times$ 4 m $\times$ 3 m and two very small rooms of dimensions 2.5 m $\times$ 2 m $\times$ 3 m.

7.4.2 Parameters

In the parametric study, two different soil types have been considered. Both soil types are modeled as a homogeneous half space. The first, stiff soil is characterized by the parameters: shear wave velocity $c_{\mathrm{S}} = 250$ m/s, compressional wave velocity $c_{\mathrm{P}} = 500$ m/s, mass density $\rho = 2300$ kg/m^3, material damping ratio $\beta = 0.025$. The second, soft soil is characterized by $c_{\mathrm{S}} = 250$ m/s, $c_{\mathrm{P}} = 500$ m/s, $\rho = 2300$ kg/m^3, $\beta = 0.025$.

The distance of the building and the tunnel is given by the two distances D and L, D being the distance of the building's base plate and the tunnel's horizontal central line, and L being the distance of the building's box foundation and the tunnel's vertical central line, as shown in figure 7.11. During the parametric study, the parameter D has been changed between 9 m and 25 m, and the parameter L has been varied between 4 m and 6 m.

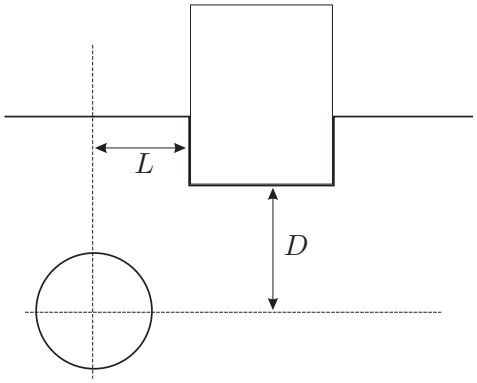

Figure 7.11: variable distances between the tunnel and the office building

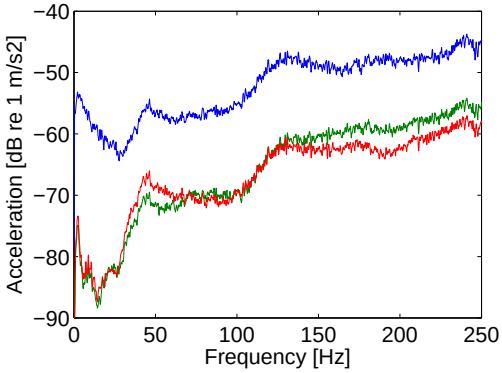

Figure 7.12: Frequency content of the acceleration of the tunnel wall near the station Kálvin square due to the passage of the metro train. Blue–base plate, red–tunnel wall radial, green–tunnel wall horizontal.

7.4.3 The excitation

As in the parameteric study the transfer functions needed to be computed for several soil types and geometries, it has been assumed that the metro excitation is two-dimensional. This assumption resulted in significant simplifications of the model. Further, it has been assumed that the displacements of the tunnel of the new line will be similar to the displacements on the tunnel wall of the line m3 at the station Kálvin tér.

The tunnel displacements due to the pasasge of the metro train in the tunnel of the line m3 were measured during the measurment campaign. The frequency content of the wall accelerations is plotted in figure 7.12. The tunnel's wall vibrates in the horizontal and vertical direction with approximately the same magnitude. The vertical vibration of the base plate is 10 dB larger than the vibration of the tunel's side wall.

Due to the assumption of the two-dimentional excitation, the modal coordinates of the three modes displayed in figure 7.8 could be directly computed from the three measured tunnel accelerations. In a following step, the structural and acoustic response of the office building could be computed.

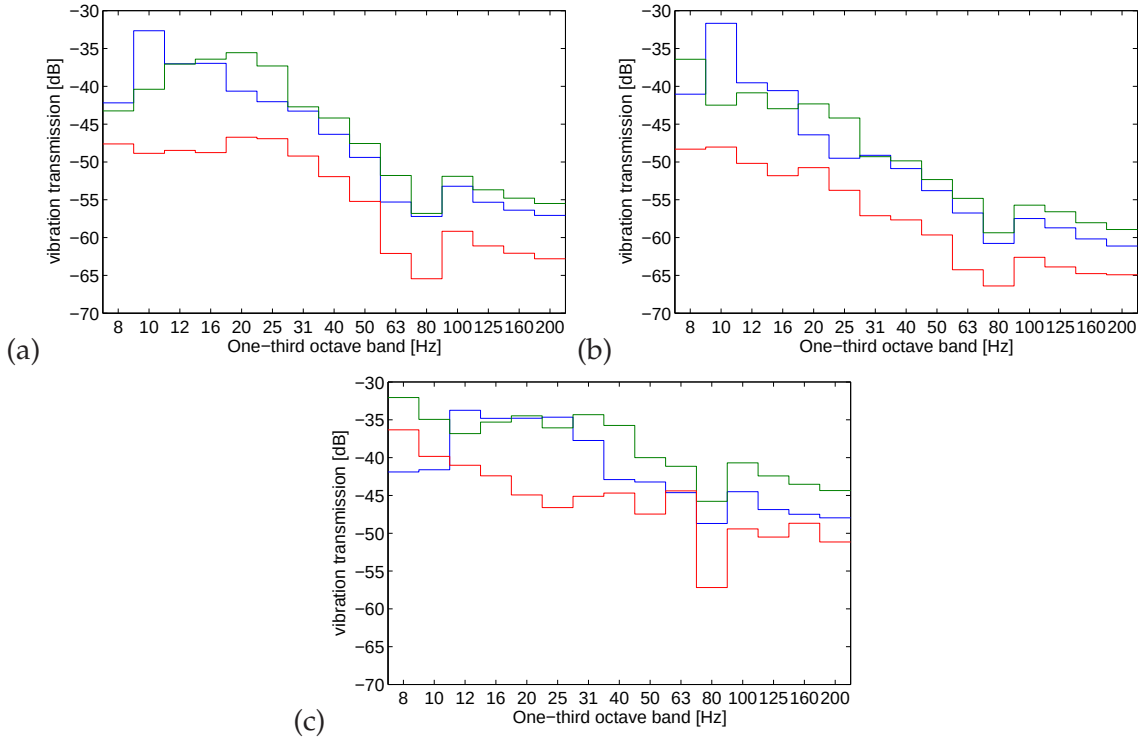

Figure 7.13: Vibration amplification between the tunnel and the building's foundation for (a) $D = 15$ m and $c_S = 150$ m/s, (b) $D = 25$ m and $c_S = 150$ m/s, (c) $D = 25$ m and $c_S = 250$ m/s. The blue curve corresponds to the vertical rigid body mode, the red to the horizontal compressional mode and the green to the vertical compressional mode.

7.4.4 Transfer functions

Figure 7.13 shows the vibration attenuation between the metro tunnel and the building's foundation. The vibration attenuation was determined by computing the displacement in the center of the building's foundation due to a modal excitation with unit amplitude. In the figure, the attenuation is given for all the three tunnel mode shapes, for different depth values D and for both soil types.

The curves show a descending slope, especially for the flexible soil characterised by $c_S = 150$ m/s. This is due to the geometrical and material damping of the soil. For the case of low frequency vibrations, the tunnel at a depth of 15 m behaves similarly to the tunnel at a depth of 25 m. The difference in depth is more pronounced in the higher frequency range, where the deeper tunnel induces 5 dB smaller vibrations in the buildings foundation. Comparing figures 7.13a and 7.13c that correspond to the same depth $D = 15$ m but different soil properties, it can be stated that the attenuation is less for the case of the stiffer soil. The large difference in the higher frqeuency range implies that the role of the material damping in the total attenuation is greater than the role of the geometrical damping.

Figure 7.14 shows the transfer functions relating the modal displacement of the tunnel and the acoustic response of one room of the portal frame building building. The chosen room is in the fisrt floor of the building. Its dimensions are 2.5 m $\times$ 4 m $\times$ 3 m. The absorption coefficient of the walls' material is considered to be $\alpha = 0.1$. The transfer functions

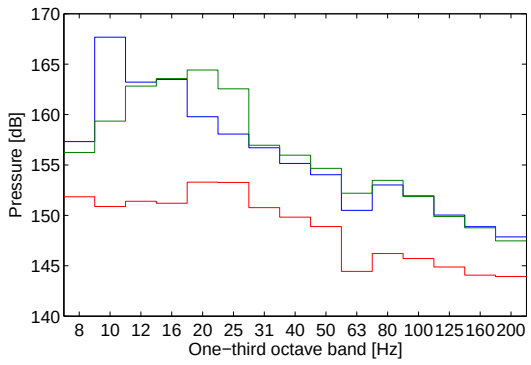

(a)

Figure 7.14: One-third octave band sound pressure levels in one room of the office building due to unit modal displacement of the tunnel. The blue curve corresponds to the vertical rigid body mode, the red to the horizontal compressional mode and the green to the vertical compressional mode.

correspond to a tunnel depth $D = 15$m and the soft soil.

7.5 The requirement curves

The transfer functions have been used to determine the maximal allowed vibration velocity of the tunnel wall as follows:

- Considering the tunnel depth and the soil type, four cases have been taken into account. Case A1 stands for a deep tunnel in soft soil, case A2 stands for a deep tunnel in stiff soil. Case B1 correspondes to the shallow tunnel in soft soil and case B2 stands for a shallow tunnel in stiff soil.
- For each case, the computed transfer functions have been used to determine the sound pressure in all the 15 rooms of the building due to the passage of a metro train described by the tunnel wall vibrations given in figure 7.12. This sound pressure response have been computed as the average from 20 randomly chosen points in each room.
- For each one-third octave band, the maximal sound pressure in the building have been computed from the 15 room responses. This resulted in a worst case value over the building for each one-third octave band.
- The excitation spectra in figure 7.12 have been weighted by a frequency-independent scalar so that the resulting sound pressure level in the building is equal to the limit defined by the Hungarian standard [Kör02].

The Hungarian standard defines the maximal indoor noise level due to traffic excitation at a sound pressure level of 30 dBA. This sound pressure level is computed by averaging the sound energy over 8 hours in the daytime. As the passage of the metro train takes approximately 10 seconds and the average daytime frequency of the metro passages will be one passage per 3-4 minutes, the standard is fulfilled if the sound pressure level of one passage does not exceed 42 dBA. This sound pressure value was used as the limit that defined the weighting factor of the excitation velocity on the tunnel.

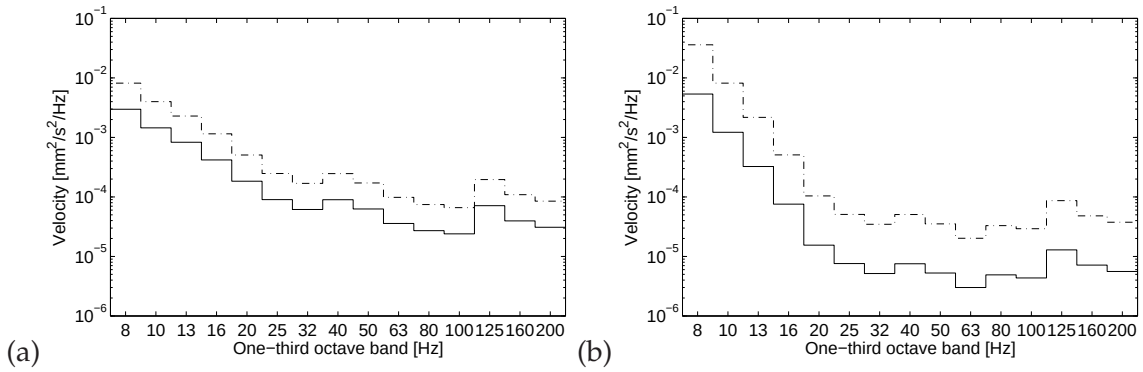

Figure 7.15: The tunnel vibration requirement curves for the case of the (a) deep and the (b) shallow tunnel parts. The solid curve stands for the case of the stiff soil and the dashed-dotted curve stands for the case of the soft soil.

The resulting excitation velocity at the tunnel's base plate is considered as the tunnel's vibration requirement. The vibration requirement curves for the four cases A1, A2, B1 and B2 are given in figure 7.15. Case A has been computed from the transfer functions corresponding to a depth $D = 20$ m, while case B was computed using the depth $D = 4$ m.

Chapter 8

Conclusions

This thesis presented a coupled deterministic numerical model for the modeling of ground-borne noise and vibration due to traffic excitation. It has been shown that the source model of Lombaert, the dynamic soil-structure interaction model of Clouteau and Aubry and a spectral finite element method used for the sound radiation problem can be coupled into a complex numerical model. The model describes the total vibration path and accounts for vibration generation by a moving vehicle, vibration propagation in layered soil, dynamic soil-structure interaction and sound radiation into closed acoustic spaces. New elements in the coupled model are the spectral finite element model for the acoustic radiation problem and the application of the Combined Helmholtz Integral Equation Formalism for the computation of the soil's dynamic stiffness.

The acoustic model was derived in Chapter 5. It has been found that the original form of the spectral finite element method can be significantly simplified if the acoustic impedance of the walls is distributed uniformly over the walls or the walls have a small absorption coefficient. The effect of wall openings on the re-radiated noise has been investigated.

The application of the Combined Helmholtz Integral Equation Formalism for the mitigation of fictitious eigenfrequencies in elastodynamics has been tackled in Chapter 4. It has been shown that the material damping of the ground affects the error due to the fictitious eigenfrequencies, and this error can be avoided by the application of the CHIEF method.

The coupled model has been used in a complex numerical example to compute the ground-borne noise and vibration from high-speed surface trains in a portal frame office building. The effect of dynamic soil-structure interaction on the re-radiated noise has been investigated, and it has been found that for the case of large difference between the stiffness of the soil and the structure's foundation, simplified models can describe the vibration transmission between the soil and the structure without loss of accuracy in the in-door noise. It has been demonstrated how the coupled method can be used to predict the effectiveness of different vibration isolation methods.

Finally, a practical application of the coupled model has been demonstrated.

8.1 Recommendation for further work

A great advantage of the presented integrated model is its complexity. The model can account for several different mechanisms in the vibration chain, and it is able to investigate the effect of parameter changes in the soil, in the structural components or in the acoustic

properties.

This complexity is also a significant disadvantage of the method, because lots of the needed input parameters are unknown in most of the practical cases. The soil layering and material properties of the layers, the dynamic properties of structural components, the properties of structural joints, the complex wall impedance values or the frequency dependence of the wall absorption are all parameters of the model that can not be known exactly before a structure is constructed, or can not be measured exactly for the case of an existing building. Therefore, stochastic modeling of vibration propagation is the most important issue in the recommended future work. There is a large need for complex coupled stochastic numerical models that can take the known variability or uncertainty of the input parameters into account, and give the desired outputs in the form of probability density functions or fuzzy numbers. These methods can help us in distinguishing between parameters having different influence on the outputs.

The capabilities of the presented coupled numerical model are recommended to exploit with several parametric studies regarding vibration isolation of structures. The optimal design of base isolation is still an open question. Is base isolation more efficient if the foundation is isolated from the structure or is it better if the isolation is applied between the basement level and the superstructure? What is the effect of simultaneous isolation at different levels of the structure? What is the optimal distribution of the resilient material under a floating floor? These questions are to be answered by means of parametric studies.

Regarding the acoustic radiation problem, a possible way of future research can be the modeling of more complex room geometries with the spectral finite element method. This topic involves the computation of dynamic modes of coupled acoustic spaces. An other important research field is the proper modeling of wall openings by applying perfectly matched layers (PML) on the opening surfaces instead of modeling with absorbing boundary conditions.

International journal papers

IJ1 A.B. Nagy, **P. Fiala**, F. Márki, F. Augusztinovicz, G. Degrande, S. Jacobs, and D. Brassenx. Prediction of interior noise in buildings, generated by underground rail traffic. *Journal of Sound and Vibration*, 293(3-5):680–690, 2006. Proceedings of the 8th International Workshop on Railway Noise, Buxton, U.K., 8-11 September 2004.

IJ2 **P. Fiala**, G. Degrande, and F. Augusztinovicz. Numerical modelling of ground-borne noise and vibration in buildings due to surface rail traffic. *Journal of Sound and Vibration*, 301:718–738, 2007.

IJ3 **P. Fiala**, S. Gupta, G. Degrande, and F. Augusztinovicz. A comparative study of different measures to mitigate ground borne noise and vibration from underground trains. *Journal of Sound and Vibration*. Submitted for publication

National journal papers

NJ1 **P. Fiala**. Talajrezgések numerikus modellezése peremelem módszerrel. *Akusztikai Szemle*, 5(2–3):9–14, 2003.

NJ2 T. Mozsolics and **P. Fiala**. Mozgó hangsugárzók hangterének számítása. *Akusztikai Szemle*, 6(1):13–18, 2005.

International conference papers

IC1 **P. Fiala**, J. Granát, and F. Augusztinovicz. Analysis of soil vibration by means of the boundary element method. In *Proceedings of the 27th International Seminar on Modal Analysis*, Leuven, Belgium, September 2002.

IC2 F. Augusztinovicz A. Kotschy A. B. Nagy, **P. Fiala**. Prediction of radiated noise in enclosures using a rayleigh integral based technique. In *CD Proc. InterNoise 2004*, Prague, 2004.

IC3 A.B.Nagy, **P. Fiala**, F.Márki, F. Augusztinovicz, G. Degrande, and S. Jacobs. Calculation of re-radiated noise in buildings, generated by underground rail traffic. In *CD Proc. 29th ISMA Conference*, Leuven, Belgium, 2004.

IC4 A.B. Nagy, **P. Fiala**, F. Márki, F. Augusztinovicz, G. Degrande, S. Jacobs, and D. Brassenx. Prediction of interior noise in buildings, generated by underground rail traffic. In D. Thompson and Ch. Jones, editors, *8th International Workshop on Railway Noise*, volume 2, pages 613–620, Buxton, U.K., September 2004.

IC5 **P. Fiala**, J. Granát, and F. Augusztinovicz. Modelling of ground vibrations in the vicinity of a tangent railway track. In *CD Proc. of Forum Acusticum 2005*, Budapest, Hungary, August 2005.

IC6 **P. Fiala**, G. Degrande, G. Granát, and F. Augusztinovicz. Structural and acoustic response of buildings in the higher frequency range due to surface rail traffic. In *ICSV13 13th International Congress on Sound and Vibration*, Vienna, Austria, July 2006.

IC7 **P. Fiala** and G. Degrande. Vibrations and re-radiated noise in buildings generated by surface high-speed train traffic. In *Proceedings of the 7th National Congress on Theoretical and Applied Mechanics*, Mons, Belgium, May 2006. National Committee for Theoretical and Applied Mechanics.

IC8 S. Gupta, **P. Fiala**, M.F.M Hussein, H. Chebli, G. Degrande, F. Augusztinovicz, H.E.M. Hunt, and D. Clouteau. A numerical model for ground-borne vibrations and re-radiated noise in buildings from underground railways. In *Proceedings of the 29th International Conference on Noise and Vibration Engineering*, Leuven, Belgium, September 2006.

IC9 **P. Fiala**, S. Gupta, G. Degrande, and F. Augusztinovicz. A numerical model for re-radiated noise in buildings from underground railways. In *Proceedings of the 9th International Workshop on Railway Noise*, Munich, Germany, September 2007.

IC10 G. Degrande, S. Gupta, **P. Fiala**, and F. Augusztinovicz. A numerical model for ground-borne vibrations and re-radiated noise in buildings from underground railways. In *Proceedings of the 3rd International Symposium on Environmental Vibrations: Prediction, Monitoring, Mitigation and Evaluation*, Beijing, September 2007.

Bibliography

[AB94] N. Atalla and R.J. Bernhard. Review of numerical solutions for low-frequency structural-acoustics problems. *Applied Acoustics*, 43:271–294, 1994.

[AC92] D. Aubry and D. Clouteau. A subdomain approach to dynamic soil-structure interaction. In V. Davidovici and R.W. Clough, editors, *Recent advances in Earthquake Engineering and Structural Dynamics*, pages 251–272. Ouest Editions/AFPS, Nantes, 1992.

[AL83] R.J. Apsel and J.E. Luco. On the Green's functions for a layered half-space. Part II. *Bulletin of the Seismological Society of America*, 73:931–951, 1983.

[Ami90] S. Amini. On the choice of the coupling parameter in boundary integral formulations of the exterior acoustic problem. *Applicable Analysis*, 35:75–92, 1990.

[Aue94] L. Auersch. Wave propagation in layered soils: theoretical solution in wavenumber domain and experimental at results of hammer and railway traffic excitation. *Journal of Sound and Vibration*, 173(2):233–264, 1994.

[Aue05] L. Auersch. The excitation of ground vibration by rail traffic: theory of vehicle-track-soil interaction and measurements on high-speed lines. *Journal of Sound and Vibration*, 284(1-2):103–132, 2005. Accepted for publication. In press.

[Bal96] E. Balmes. Optimal ritz-vectors for component mode synthesis using the singular value decomposition. *AIAA Journal*, 34:1256–1260, 1996.

[BB81] P.K. Banerjee and R. Butterfield. *Boundary element methods in engineering science*. McGrawn-Hill Book Company, UK, 1981.

[BM71] A.J. Burton and G.F. Miller. The application of integral equation methods to the numerical solution of some exterior boundary-value problems. In *Proceedings of the Royal Society of London*, volume 323, pages 201–210, 1971.

[Bru65] G.B. Brundrit. A solution to the problem of scalar scattering from a smooth bounded obstacle using integral equations. *Quarterly Journal of Mechanics and Applied Mathematics*, 18(4):473–489, 1965.

[CB68] R.J. Craig and M. Bampton. Coupling of substructures for dynamic analyses. *AIAA Journal*, 6(7):1313–1319, 1968.

[Clo90] D. Clouteau. *Propagation d'ondes dans des milieux hétérogènes. Application à la tenue des ouvrages sous séismes*. PhD thesis, Laboratoire de Mécanique des Sols, Structures et Matériaux, Ecole Centrale de Paris, 1990.

[Clo99a] D. Clouteau. *MISS Revision 6.2, Manuel Scientifique*. Laboratoire de Mécanique des Sols, Structures et Matériaux, Ecole Centrale de Paris, 1999.

[Clo99b] D. Clouteau. *MISS Revision 6.2, Manuel Utilisateur*. Laboratoire de Mécanique des Sols, Structures et Matériaux, Ecole Centrale de Paris, 1999.

[CLS90] N. Chouw, R. Le, and G. Schmid. Ausbreitung von Erschutterungen in homogenem Boden. Numerische Untersuchungen mit der Randelementmethode im Frequenzbereich. *Bauingenieur*, 65:399–406, 1990.

[Cop67] L.G. Copley. Integral equation method for radiation from vibrating bodies. *Journal of the Acoustical Society of America*, 41:807–816, 1967.

[Cro65] J.H.A. Crocket. Some practical aspects of vibration in civil engineering. In *Proceedings of the symposium on vibration in civil engineering*, pages 253–271, 1965.

[CW90] H. Cramer and W. Wunderlich. Multiphase models on soil dynamics. In *Structural Dynamics*, pages 165–172, Balkema, Rotterdam, 1990.

[DBB99] A. Deraemaeker, I. Babuska, and Ph. Bouillard. Dispersion and pollution of the fem solution for the helmholtz equation in one, two and three dimensions. *International Journal for Numerical Methods in Engineering*, 46:471–499, 1999.

[DDRVdBS98] G. Degrande, G. De Roeck, P. Van den Broeck, and D. Smeulders. Wave propagation in layered dry, saturated and unsaturated poroelastic media. *International Journal of Solids and Structures*, 35(34-35):4753–4778, 1998. Poroelasticity Maurice A. Biot memorial issue.

[Deg02] G. Degrande. Wave propagation in the soil: theoretical background and application to traffic induced vibrations. In H. Grundmann, editor, *Proceedings of the 5th European Conference on Structural Dynamics: Eurodyn 2002*, pages 27–40, Munich, Germany, September 2-5 2002. Semi-plenary keynote lecture.

[dLBFM$^+$98] A. de La Bourdonnaye, C. Farhat, A. Macedo, F. Magoules, and F. Roux. A non-overlapping domain decomposition method for the exterior helmholtz problem. *Contemporary Mathematics*, 218:42–66, 1998.

[Doy97] J.F. Doyle. *Wave propagation in structures: spectral analysis using discrete Fourier transforms*. Springer-Verlag, 1997.

[DS01] G. Degrande and L. Schillemans. Free field vibrations during the passage of a Thalys HST at variable speed. *Journal of Sound and Vibration*, 247(1):131–144, 2001.

[FDGA06] P. Fiala, G. Degrande, G. Granát, and F. Augusztinovicz. Structural and acoustic response of buildings in the higher frequency range due to surface rail traffic. In *ICSV13 13th International Congress on Sound and Vibration*, Vienna, Austria, July 2006.

[FR91] C. Farhat and F. Roux. A method for finite element tearing and interconnecting and its parallel solution algorithm. *International Journal for Numerical Methods in Engineering*, 32:1205–1227, 1991.

[GPVR00] T. Gustafsson, H.R. Pota, J. Vance, and B.D. Rao. Estimation of acoustical room transfer functions. In *Proceedings of the 39th IEEE Conference on Decision and Control*, Sydney, Australia, December 2000.

[Har91] C.M. Harris. *Handbook of Acoustical Measurements and Noise Control*. McGraw-Hill, 1991.

[Has53] N.A. Haskell. The dispersion of surface waves on multilayered media. *Bulletin of the Seismological Society of America*, 73:17–43, 1953.

[HM90] D.Le Houdéec and S. Malek. Effectiveness of trenches or screens for scattering surface waves. In *Structural Dynamics*, pages 709–715, Balkema, Rotterdam, 1990.

[Hun07] H.E.M. Hunt. Types of rail roughness and the selection of vibration isolation measures. In *Proceedings of the 9-th International Workshop on Railway Noise*, Munich, Germany, September 2007.

[JLHPP98] D. V. Jones, D. Le Houedec, A. T. Peplow, and M. Petyt. Ground vibration in the vicinity of a moving harmonic rectangular load on a half-space. *European Journal of Mechanics, A/Solids*, 17(1):153–166, 1998.

[JP91] D.V. Jones and M. Petyt. Ground vibration in the vicinity of a strip load: a two-dimensional half-space model. *Journal of Sound and Vibration*, 147(1):155–166, 1991.

[JP92] D.V. Jones and M. Petyt. Ground vibration in the vicinity of a strip load: an elastic layer on a rigid foundation. *Journal of Sound and Vibration*, 152(3):501–515, 1992.

[JP93] D.V. Jones and M. Petyt. Ground vibration in the vicinity of a rectangular load on a half-space. *Journal of Sound and Vibration*, 166(1):141–159, 1993.

[JP97] D.V. Jones and M. Petyt. Ground vibration in the vicinity of a rectangular load acting on a viscoelastic layer over a rigid foundation. *Journal of Sound and Vibration*, 203(2):307–319, 1997.

[Kau86] E. Kausel. Wave propagation in anisotropic layered media. *International Journal for Numerical Methods in Engineering*, 23:1567–1578, 1986.

[Kau94] E. Kausel. Thin-layer method: Formulation in the time domain. *International Journal for Numerical Methods in Engineering*, 37:927–941, 1994.

[KP82] E. Kausel and R. Peek. Dynamic loads in the interior of a layered stratum: an explicit solution. *Bulletin of the Seismological Society of America*, 72(5):1459–1481, 1982.

[KR81] E. Kausel and J.M. Roësset. Stiffness matrices for layered soils. *Bulletin of the Seismological Society of America*, 71(6):1743–1761, 1981.

[Kör02] Környezetvédelmi és Egészségügyi Minisztérium. *8/2002. (III.22) KöM-EüM együttes rendelet a zaj-és rezgésterhelési határértékek megállapításáról*, 2002.

[Kup65] V.D. Kupradze. *Potential Methods in the Theory of Elasticity*. Israel Program of Scientific Translation, Jerusalem, 1965.

[Kus69] R. Kussmaul. Ein numerisches vervahren zur lösung der neumannschen aussenraumproblem für die helmholtzsche schwingungsgleichung. *Computing*, 4:246–273, 1969.

[LA83] J.E. Luco and R.J. Apsel. On the Green's functions for a layered half-space. Part I. *Bulletin of the Seismological Society of America*, 4:909–929, 1983.

[Lam04] H. Lamb. On the propagation of tremors over the surface of an elastic solid. *Philosophical Transactions of the Royal Society*, A203:1–42, 1904.

[LD01] G. Lombaert and G. Degrande. Experimental validation of a numerical prediction model for free field traffic induced vibrations by in situ experiments. *Soil Dynamics and Earthquake Engineering*, 21(6):485–497, 2001.

[LD03] G. Lombaert and G. Degrande. The experimental validation of a numerical model for the prediction of the vibrations in the free field produced by road traffic. *Journal of Sound and Vibration*, 262:309–331, 2003.

[LDC00] G. Lombaert, G. Degrande, and D. Clouteau. Numerical modelling of free field traffic induced vibrations. *Soil Dynamics and Earthquake Engineering*, 19(7):473–488, 2000.

[LDKF06] G. Lombaert, G. Degrande, J. Kogut, and S. François. The experimental validation of a numerical model for the prediction of railway induced vibrations. *Journal of Sound and Vibration*, 2006. Accepted for publication.

[LKL99] U. Lee, J. Kim, and A.Y.T. Leung. The spectral element method in structural dynamics. *The Shock and Vibration Digest*, 32(6):451–465, 1999.

[LMPLH02] G. Lefeuve-Mesgouez, A.T. Peplow, and D. Le Houédec. Surface vibration due to a sequence of high speed moving harmonic rectangular loads. *Soil Dynamics and Earthquake Engineering*, 22:459–473, 2002.

[Lom01] G. Lombaert. *Development and experimental validation of a numerical model for the free field vibrations induced by road traffic*. PhD thesis, Department of Civil Engineering, K.U.Leuven, 2001.

[Lov44] A.E.H. Love. *The mathemaical theory of elasticity*. Dover publications, New York, 1944.

[LW72] J. Lysmer and G. Waas. Shear waves in plane infinite structures. *Journal of the Engineering Mechanics Division, Proceedings of the ASCE*, 98(EM1):85–105, 1972.

[Lys70] J. Lysmer. Lumped mass method for Rayleigh waves. *Bulletin of the Seismological Society of America*, 60(1):89–104, 1970.

[McN71] R. McNeil. A hybrid method of component mode synthesis. *Computers and Structures*, 1(4):581–601, 1971.

[MH94] H.A. Müller M. Heckl. *Taschenbuch der Technischen Akustik*. Springer Verlag, Berlin, 1994.

[MK83] J. Melke and S. Kraemer. Diagnostic methods in the control of railway noise and vibration. *Journal of Sound and Vibration*, 87(2):377–386, 1983.

[MK00] C. Madshus and A.M. Kaynia. High-speed railway lines on soft ground: dynamic behaviour at critical train speed. *Journal of Sound and Vibration*, 231(3):689–701, 2000.

[Mül90] G.H. Müller. Soil-vibration and radiatin of energy under a harmonic load on the soil-surface. In *Structural Dynamics*, pages 723–729, Balkema, Rotterdam, 1990.

[MV05] David Moens and Dirk Vandepitte. A survey of non-probabilistic uncertainty treatment in finite element analysis. *Computer Methods in Applied Mechanics and Engineering*, 194(12–16):1527–1555, 8 April 2005.

[MVB05] A.V. Metrikine, S.N. Verichev, and J. Blauwendraad. Stability of a two-mass oscillator moving on a beam supported by a visco-elastic half-space. *International Journal of Solids and Structures*, 42:1187–1207, 2005.

[NFM+06] A.B. Nagy, P. Fiala, F. Márki, F. Augusztinovicz, G. Degrande, S. Jacobs, and D. Brassenx. Prediction of interior noise in buildings, generated by underground rail traffic. *Journal of Sound and Vibration*, 293(3-5):680–690, 2006. Proceedings of the 8th International Workshop on Railway Noise, Buxton, U.K., 8-11 September 2004.

[Pan65] I.O. Panich. On the question of solvability of the external boundary value problem for the wave equation and maxwell's equation. *Uspeki Mat. Nauk. (Russian Math. Survey)*, 20(1):221–226, 1965.

[PCD04] L. Pyl, D. Clouteau, and G. Degrande. A weakly singular boundary integral equation in elastodynamics for heterogeneous domains mitigating fictitious eigenfrequencies. *Engineering Analysis with Boundary Elements*, 28(12):1493–1513, 2004.

[Pet98] M. Petyt. *Introduction to finite element vibration analysis*. Cambridge University Press, Cambridge, 1998.

[Pie91] A.D. Pierce. *Acoustics. An introduction to ints physical principles and applications*. The Acoustical Society of America, New York, 1991.

[Pyl04] L. Pyl. *Development and experimental validation of a numerical model for traffic induced vibrations in buildings*. PhD thesis, Department of Civil Engineering, K.U.Leuven, 2004.

[Ray87] J.W.S. Rayleigh. On waves propagated along the plane surface of an elastic solid. *Proceedings of the London Mathematical Society*, 17:4–11, 1887.

[RFBA04] S.Á. Rubio, J. Francisco, J.J. Benito, and E. Alarcón. The direct boundary element method: 2d site effects assessment on laterally varying layered media (methodology). *Soil Dynamics and Earthquake Engineering*, 24:167–180, 2004.

[Rub75] S. Rubin. Improved component-mode representation for structural dynamic analysis. *AIAA Journal*, 13(8):995–1006, August 1975.

[Sab93] T.C. Sabine. *Collected papers on acoustics*. Peninsula Publishing, Los Altos, 1993.

[Sch68] H.A. Schenck. Improved integral formulation for acoustic radiation problems. *Journal of the Acoustical Society of America*, 44:45–58, 1968.

[Sch07] M. Schevenels. *The impact of uncertain dynamic soil characteristics on the prediction of ground vibrations*. PhD thesis, Department of Civil Engineering, K.U.Leuven, 2007.

[SF62] R.P. Shaw and M.B. Friedman. Diffraction of a plane schock wave by a free cylindrical obstacle at a free surface. pages 371–379, 1962.

[SJP99a] X. Sheng, C.J.C. Jones, and M. Petyt. Ground vibration generated by a harmonic load acting on a railway track. *Journal of Sound and Vibration*, 225(1):3–28, 1999.

[SJP99b] X. Sheng, C.J.C. Jones, and M. Petyt. Ground vibration generated by a load moving along a railway track. *Journal of Sound and Vibration*, 228(1):129–156, 1999.

[Tal94] P.L. Tallec. *Domain decomposition methods in computational mechanics*. Compuattional Mechanics Advances. North-Holland, 1994.

[Tho50] W.T. Thomson. Transmission of elastic waves through a stratified solid medium. *Journal of Applied Physcis*, 21:89–93, 1950.

[Urs73] F. Ursell. On the exterior problems of acoustics. *Proceedings of the Cambridge Philosophical Society*, 74:117–125, 1973.

[Urs78] F. Ursell. On the exterior problems of acoustics ii. *Proceedings of the Cambridge Philosophical Society*, 84:545–548, 1978.

[vhG01] Raymond van het Groenewoud. Zo zot van haar. *Een jongen uit Schaarbeek*, 2001.

[WC96] J.P. Wolf and C.Song. *Finite-element modelling of unbounded media*. John Wiley and Sons, 1996.

[Wol85] J.P. Wolf. *Dynamic soil-structure interaction*. Prentice-Hall, Englewood Cliffs, New Jersey, 1985.

[WP90] J.P. Wolf and A. Paronesso. One-dimensional modeling of the non-linear far field in soil-structure interaction analysis. In *Proceedings of the 4th US National Conference on Earthquake Engineering*, Palm Springs, California, 1990. Earthquake Engineering Research Center.

[www03] http://www.convurt.com, 2003.

[Zam94] S.I. Zaman. *Integral equation formulations of exterior acoustic scattering problems*. PhD thesis, City University, London, UK, 1994.

[Zie86] O.C. Zienkiewicz. *The finite element method*. McGraw-Hill, third edition, 1986.

[ZT88] O.C. Zienkiewicz and R.L. Taylor. *The finite element method, Volume 1: basic formulation and linear problems*. McGraw-Hill, fourth edition, 1988.

Appendix A

Integral transforms

Fourier transformation from the time domain to the frequency domain is defined by:

$$\hat{u}(\omega) = \int_{-\infty}^{+\infty} u(t) \mathrm{e}^{-\mathrm{i}\omega t} \mathrm{d}t \tag{A.1}$$

The inverse Fourier-transform is defined as:

$$u(t) = \frac{1}{2\pi} \int_{-\infty}^{+\infty} \hat{u}(\omega) \mathrm{e}^{\mathrm{i}\omega t} \mathrm{d}\omega \tag{A.2}$$

The Fourier-transform from the spatial domain to the wavenumber domain is defined as:

$$\tilde{u}(k_x) = \int_{-\infty}^{+\infty} \hat{u}(x) \mathrm{e}^{\mathrm{i}k_x x} \mathrm{d}x \tag{A.3}$$

and the corresponding inverse Fourier-transform is defined by:

$$\hat{u}(x) = \frac{1}{2\pi} \int_{-\infty}^{+\infty} \tilde{u}(k_x) \mathrm{e}^{-\mathrm{i}k_x x} \mathrm{d}k_x \tag{A.4}$$

Appendix B

The dynamic stiffness matrices for the in-plane wave propagation

B.1 The dynamic stiffness matrix of a soil layer element for P-SV waves

The ij-th element of the symmetrical in-plane dynamic stiffness matrix $\tilde{\mathbf{S}}^{\mathrm{L}}_{\mathrm{P-SV}}$ is given in the form $\tilde{S}^{\mathrm{L}}_{ij} = A\tilde{Q}^{\mathrm{L}}_{ij}$, where

$$\tilde{Q}^{\mathrm{L}}_{11} = \frac{1}{t}\cos k_{\mathrm{P}z}d\sin k_{\mathrm{S}z}d - s\sin k_{\mathrm{P}z}d\cos k_{\mathrm{S}z}d \tag{B.1a}$$

$$\tilde{Q}^{\mathrm{L}}_{12} = \frac{3-t^2}{1+t^2}(1-\cos k_{\mathrm{P}z}d\cos k_{\mathrm{S}z}d) + \frac{1+2s^2t^2-t^2}{st(1+t^2)}(\sin k_{\mathrm{P}z}d\sin k_{\mathrm{S}z}d) \tag{B.1b}$$

$$\tilde{Q}^{\mathrm{L}}_{13} = -s\sin k_{\mathrm{P}z}d - \frac{1}{t}\sin k_{\mathrm{S}z}d \tag{B.1c}$$

$$\tilde{Q}^{\mathrm{L}}_{14} = \cos k_{\mathrm{P}z}d - \cos k_{\mathrm{S}z}d \tag{B.1d}$$

$$\tilde{Q}^{\mathrm{L}}_{22} = \frac{1}{s}\sin k_{\mathrm{P}z}d\cos k_{\mathrm{S}z}d + t\cos k_{\mathrm{P}z}d\sin k_{\mathrm{S}z}d \tag{B.1e}$$

$$\tilde{Q}^{\mathrm{L}}_{23} = -\cos k_{\mathrm{P}z}d + \cos k_{\mathrm{S}z}d \tag{B.1f}$$

$$\tilde{Q}^{\mathrm{L}}_{24} = -\frac{1}{s}\sin k_{\mathrm{P}z}d - t\sin k_{\mathrm{S}z}d \tag{B.1g}$$

$$\tilde{Q}^{\mathrm{L}}_{33} = \frac{1}{t}\cos k_{\mathrm{P}z}d\sin k_{\mathrm{S}z}d + s\sin k_{\mathrm{P}z}d\cos k_{\mathrm{S}z}d \tag{B.1h}$$

$$\tilde{Q}^{\mathrm{L}}_{34} = \frac{t^2-3}{1+t^2}(1-\cos k_{\mathrm{P}z}d\cos k_{\mathrm{S}z}d) + \frac{t^2-2s^2t^2-1}{st(1+t^2)}(\sin k_{\mathrm{P}z}d\sin k_{\mathrm{S}z}d) \tag{B.1i}$$

$$\tilde{Q}^{\mathrm{L}}_{44} = \frac{1}{s}\sin k_{\mathrm{P}z}d\cos k_{\mathrm{S}z}d + t\cos k_{\mathrm{P}z}d\sin k_{\mathrm{S}z}d \tag{B.1j}$$

$$A = \frac{(1+t^2)k_x\mu}{2(1-\cos k_{\mathrm{S}z}d\cos k_{\mathrm{P}z}d) + (st+\frac{1}{st})(\sin k_{\mathrm{S}z}d\sin k_{\mathrm{P}z}d)} \tag{B.2}$$

and

$$t = \frac{k_{\mathrm{S}z}}{k_x} \tag{B.3a}$$

$$s = \frac{k_{\mathrm{P}z}}{k_x} \tag{B.3b}$$

B.2 The dynamic stiffness matrix of a half space element for P-SV waves

The symmetrical in-plane dynamic stiffness matrix $\tilde{\mathbf{S}}^{\mathrm{R}}_{\mathrm{P-SV}}$ of a half space is given as:

$$\tilde{\mathbf{S}}^{\mathrm{R}}_{\mathrm{P-SV}} = k_x \mu \begin{bmatrix} \frac{\mathrm{i}s(1+t^2)}{1+st} & 2-\frac{(1+t^2)}{1+st} \\ 2-\frac{(1+t^2)}{1+st} & \frac{\mathrm{i}t(1+t^2)}{1+st} \end{bmatrix} \tag{B.4}$$

Appendix C

Measurement fotos and data

Table C.1: Location and sensitivity of the acceleration sensors used at the SASW measurements in the Kelenföld City Center

#	d [m]	type	serial	sensitivity [mV/g]
1	1	B&K 4381	1161005	100
2	2	PCB 393A03	9650	1000
3	4	PCB 393A03	9651	1000
4	8	PCB 393A03	8410	1000
5	16	PCB 393A03	16594	1000
6	25	PCB 393A03	9650	1000
7	50	PCB 393A03	9651	1000

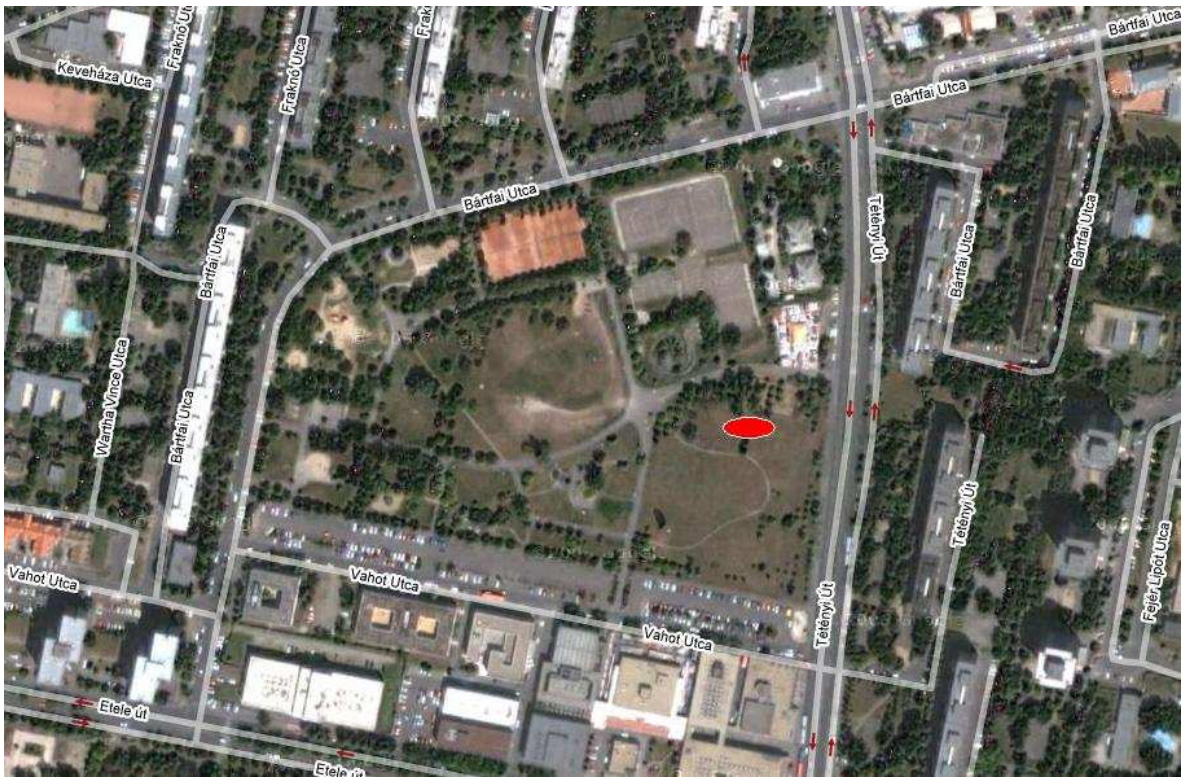

Figure C.1: Measurement location in Kelenföld City Center

Figure C.2: The measurement setup: (a) 80 kg heavy bang filled with lead shot, (b) PCB 393A03 acceleration sensor mounted on a steel pike.

Figure C.3: The building of the Kálvin Center

Figure C.4: Acceleration sensors (a) at the side wall of the tunnel, (b) at the base plate of the tunnel and (c) on the floor and the wall of the basement of the Kálvin Center

Table C.2: Dimensions of the structural elements in the Kálvin Center

Element	dimension [m]
Base plate thickness	1.0
Basement wall thickness	0.5
Diameter of columns in the basement	0.8
Diameter of columns in the floors	0.6
Central core wall thickness	0.2
Floor slab thickness	0.2
Wall thickness of neighboring building	0.2